Computational and Experimental Development of Novel Combustion Strategies for Advanced Internal Combustion Engines
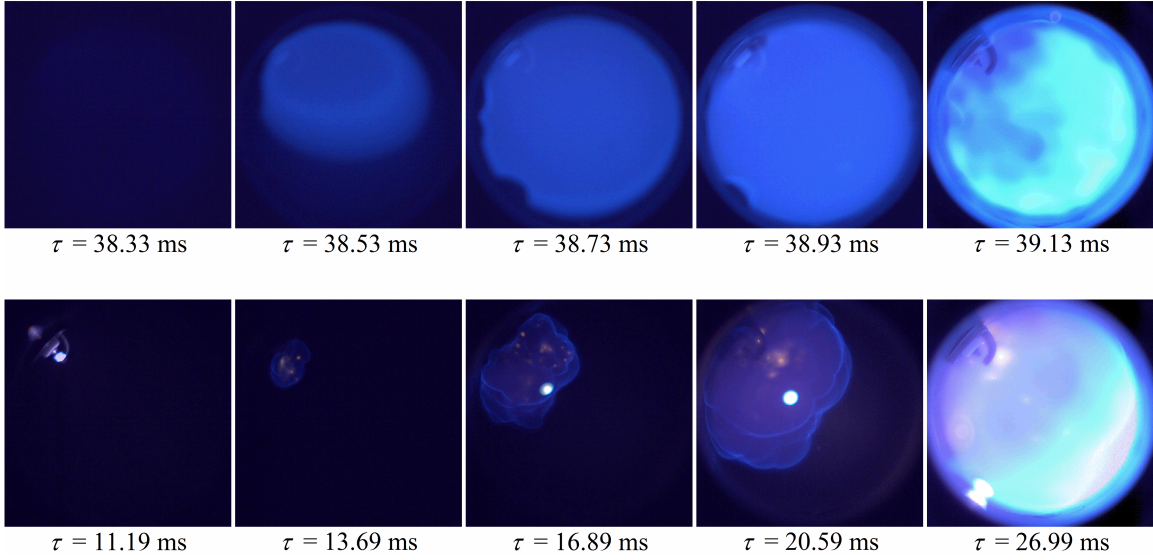
by

Dimitris Assanis

A dissertation submitted in partial fulfillment
of the requirements for the degree of
Doctor of Philosophy
(Mechanical Engineering)
in The University of Michigan
2016

Doctoral Committee:

Professor Margaret S. Wooldridge, Chair
Professor Peter Adriaens
Professor André L. Boehman
Professor Panos Y. Papalambros

$\tau = 38.33$ ms $\tau = 38.53$ ms $\tau = 38.73$ ms $\tau = 38.93$ ms $\tau = 39.13$ ms

$\tau = 11.19$ ms $\tau = 13.69$ ms $\tau = 16.89$ ms $\tau = 20.59$ ms $\tau = 26.99$ ms

High-speed imaging of combustion. [1]

To my family,
nothing is ever achieved in a vacuum.

ACKNOWLEDGEMENTS

tails. There is a reason they say a dog is a man's best friend. My brother, Nicholas, who has challenged me to think outside the box with a business mindset and for never stopping to encourage me to keep improving upon myself. And to my parents, Helen and Dennis, who have shown me the truest of unconditional love. My mother has supported me and emboldened me through every venture I have tackled in life. And to my father, for being my greatest role model any son could ever ask for because of the values and integrity that you lead your personal life with and the accomplishments you have achieved in your professional life. Thank you!

TABLE OF CONTENTS

LIST OF FIGURES

Figure

LIST OF TABLES

LIST OF APPENDICES

Appendix

ABSTRACT

Computational and Experimental Development of Novel Combustion Strategies for
Advanced Internal Combustion Engines

by

Dimitris Assanis

Chair: Margaret S. Wooldridge

Fuel lean combustion strategies are attractive methods to increase the thermal efficiency of gasoline, spark ignition, internal combustion engines, but engine design remains challenging due to the lean flammability limits of the fuel/air mixture. Turbulent jet ignition originating from a pre-chamber can help address mixture flammability limits by ejecting high enthalpy and highly reactive jets into the main combustion chamber, enabling overall lean combustion. However, appropriate mixture conditions must be achieved in the main combustion chamber as well as in the pre-chamber for this strategy to be successful.

This dissertation study considered a series of experimental and computational efforts to support the development of lean burn reciprocating engines. First, fundamental combustion experiments to quantify flame speeds, flammability limits, and the interaction between flames and auto-ignition events of lean fuel/air mixtures were performed. The approach used a rapid compression facility to study iso-octane and air mixtures at a range of equivalence ratios and dilution levels. High speed cinematography and pressure time histories were used to measure the fundamental combustion properties of the mixtures at fixed state conditions. The experiments were performed at premixed, moderate temperature (925 – 1000 K) and pressure (> 7.5 atm) conditions. The results provided the first measurements of lean flammability limits at conditions relevant to spark ignition engines.

The next phase of the research used computational fluid dynamics (CFD) of an actual prototype spark ignition engine to evaluate different methods to create ignitable mixtures in a pre-chamber while simultaneously creating fuel lean charges in the

main combustion chamber. The concept of an indirectly fueled dual pre-chamber engine was created and evaluated using the three-dimensional CFD simulations. Flow metrics were defined to evaluate the quality of the engine configurations. Six design iterations were evaluated with the goal of achieving near stoichiometric fuel-to-air equivalence ratios ($\phi = 1.0$) in two pre-chambers, while simultaneously achieving fuel lean equivalence ratios ($\phi < 1.0$) in the main combustion chamber. The simulation results showed the final iteration achieved the design goals with good flexibility in the fuel injection strategies (e.g. injection timing and fuel mass). The results also demonstrated the utility of the flow-alignment and chamber filling criteria to select nozzle design for pre-chambers.

In the next stage of the project, engine hardware was produced based on the CFD results. The prototype engine was designed and built with optical accessibility to allow evaluation of the fuel and air flow motion. High speed cinematography and pressure diagnostics were used with a fully-transparent cylinder liner to illuminate and image the fuel spray and air charge motion using Mie scattering. Fuel penetration distance, injection speed, plume cone angle, and plume to plume spray angle were measured as a function of different operating conditions. Air charge motion was qualitatively characterized. The fuel flow motion was in agreement with CFD predictions and the air charge imaging confirmed vortices were developed near the surface of the piston. The features of the fuel and air flow were considered vital based on the CFD results to passively fuel the pre-chambers. The fuel spray data are the first in situ measurements of the unique fueling strategy and unique hardware.

The combination of fundamental experiments, computational studies and applied experimental validations have demonstrated a new process and new outcomes for combustion science and technology that can operate significantly more fuel lean than traditional spark ignition engines.

CHAPTER I

Introduction

1.1 Background

The earth's atmosphere is a magical phenomenon that acts as a thermally-insulating blanket, absorbing and retaining solar radiation, in order to create an average surface temperature of around 15° C, thus capable of supporting life as we know it today. Water vapor is the most abundant greenhouse gas that helps the earth's atmosphere create this thermally-insulating blanker effect. In a nutshell, as the earth's surface temperature increases, air and trapped water vapor rises to higher and colder altitudes, causing the water vapor to condense and form clouds. When a certain air mass becomes oversaturated with water, the water vapor precipitates out of the sky in the form of rain, dropping the water vapor to a lower altitude. This self-regulating feedback mechanism creates an important transport mechanism for heat and energy to be exchanged between the earth's surface and the atmosphere.

Carbon dioxide is the second most abundant greenhouse gas species in the earth's atmosphere and a certain amount of it in our atmosphere is absolutely necessary for the existence of human beings. Plants rely on photosynthesis to convert carbon dioxide and water vapor into glucose and subsequently release oxygen, required for human life, back into the atmosphere. Unlike water-vapor, carbon dioxide does not have a self-regulating feedback mechanism to disperse heat and energy between atmosphere and the earths surface. Carbon dioxide sits in the atmosphere, until photosynthesized, and absorbs energy in its molecular bonds very efficiently. This absorbed energy would normally have been reflected back out to outer space from the earth's surface, but instead becomes trapped in the atmosphere, like sunlight in a greenhouse, and warms the atmosphere and correspondingly the earth's surface temperature.
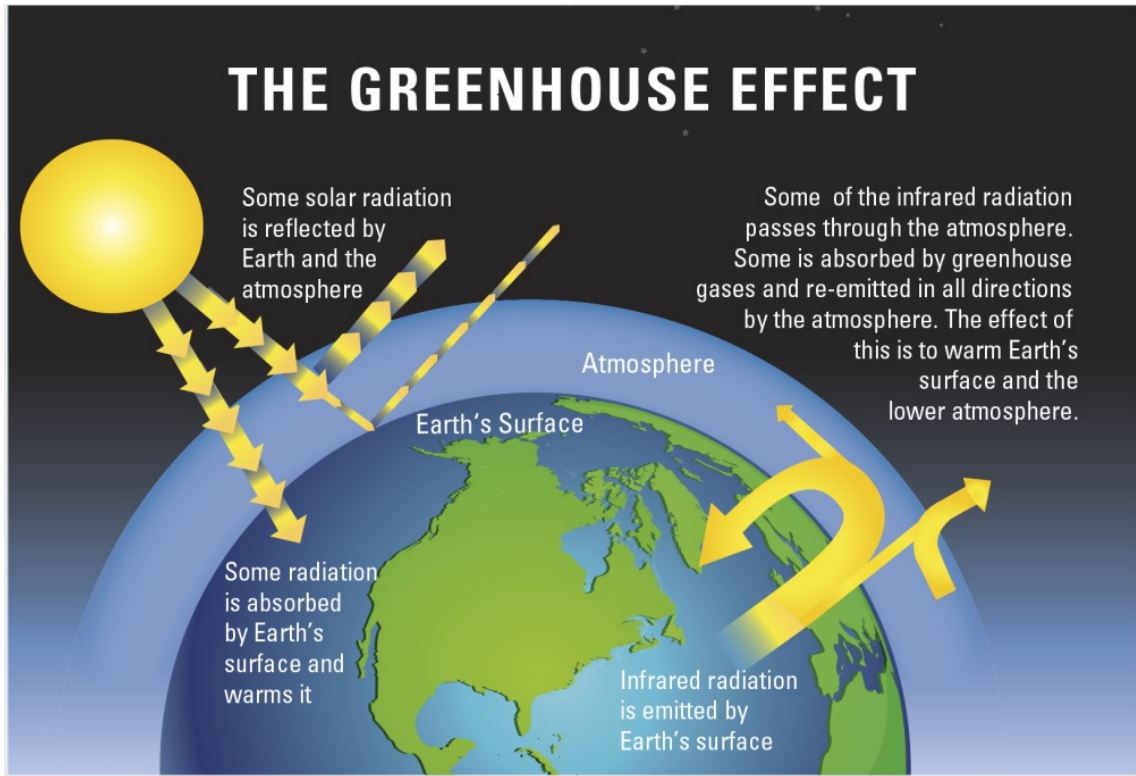
Figure 1.1: Greenhouse gasses that are responsible for creating the required livable surface temperatures on the earth can cause global warming if found in overabundance. [2].

Carbon dioxide is naturally emitted by the earth and its inhabitant, such as in the form of volcanic eruptions or from humans and other animals through our respiration, a process that combines oxygen and water to form glucose and releases carbon dioxide back into the atmosphere. For billions of years, the amount of production of naturally-occurring carbon dioxide was in balance with the naturally occurring sequestration processes of our planet. Since the industrial revolution, the amount of carbon dioxide has increased by a third, primarily through the burning of fossil fuels, thus upsetting the balance found in the earth's atmosphere. Coincidentally, the earth's surface temperature has been experiencing an unprecedented level of global warming during the same time period. It is widely undisputed today that the excess, human-produced, carbon dioxide is the leading cause of global warming due to the greenhouse effect described earlier.

Due to the significant role carbon dioxide plays as a greenhouse gas in global warming, the United States Energy Information Administration tracks and projects the carbon dioxide emissions by industry sector, see Figure 1.2, to better understand where human-produced carbon dioxide is generated. It is without a doubt that the

transportation sector has been and will continue to be the largest producer of human-produced carbon dioxide, beating out the residential, commercial, and industrial sectors. Carbon dioxide is generated when an engine in a vehicle burns carbon-based fuels, such as gasoline or diesel, in the presence of oxygen, found in air, to generate propulsion power. Given a fixed set of monetary, temporal, and human capital resources, in can be inferred the largest reduction in human-produced carbon dioxide can be achieved in the highest production sector: transportation.
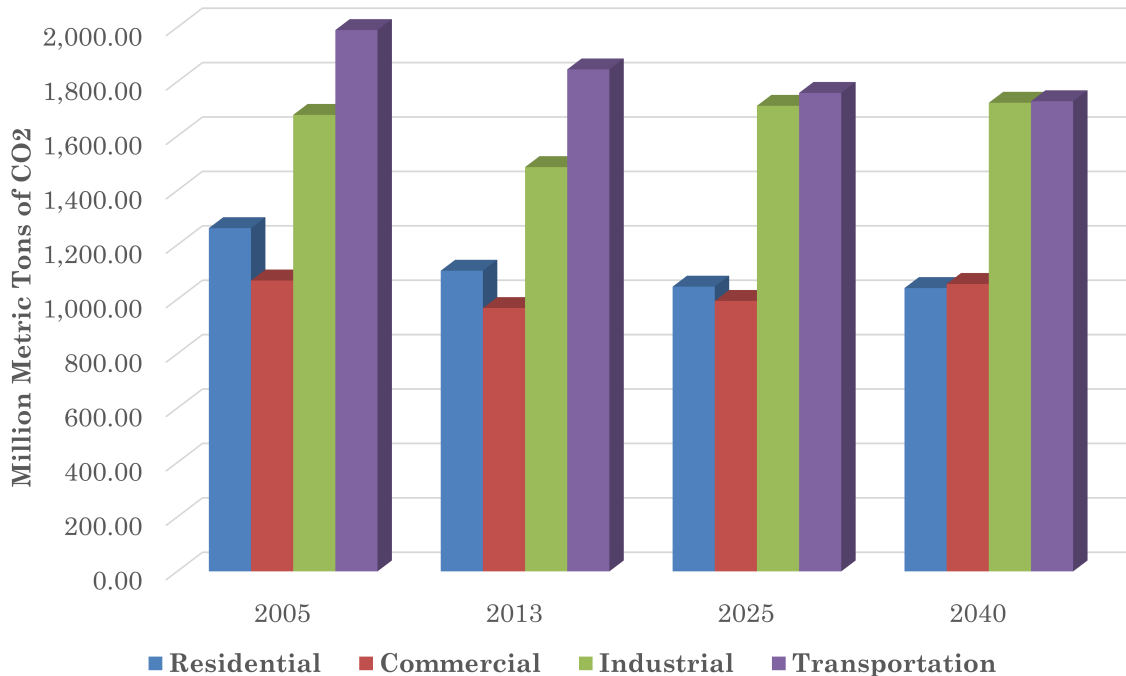
Figure 1.2: Carbon dioxide product by industry section in the United States. Data is sourced from the U.S. Energy Information Administration [3].

The United States of America's governmental agencies have decided to tackle vehicle transportation carbon dioxide production by setting a corporate average fuel economy (CAFE) target, thus ensuring that new vehicles are more fuel efficient, thus burning less fuel, and in turn emitting less carbon dioxide into the atmosphere. The 2025 CAFE mandate states that the fuel economy of a light duty passenger vehicle should be 54.5 miles per gallon (mpg) by year 2025. The average new light-duty passenger-vehicle fuel economy was 36 mpg in 2014. Thus, the government is asking for light-duty passenger vehicle manufacturers to improve the vehicle fuel economy by more than 50% by the year 2025. At the current rate of iterative fuel economy improvement, which has seen an impressive uptick historically speaking, vehicle manufacturers are projected to miss the mandate by about 10 years using traditional evolutionary vehicle technology. Thus, it is abundantly clear that revolutionary vehicle

technologies need to identified and implemented to meet the 2025 CAFE mandate of 54.5 mpg for new light-duty passenger vehicles. The work presented in this document will focus on identifying revolutionary propulsion technologies, in the form of novel combustion strategies, that can be implemented in an advanced internal combustion engine necessary to meet the 2025 CAFE mandate.
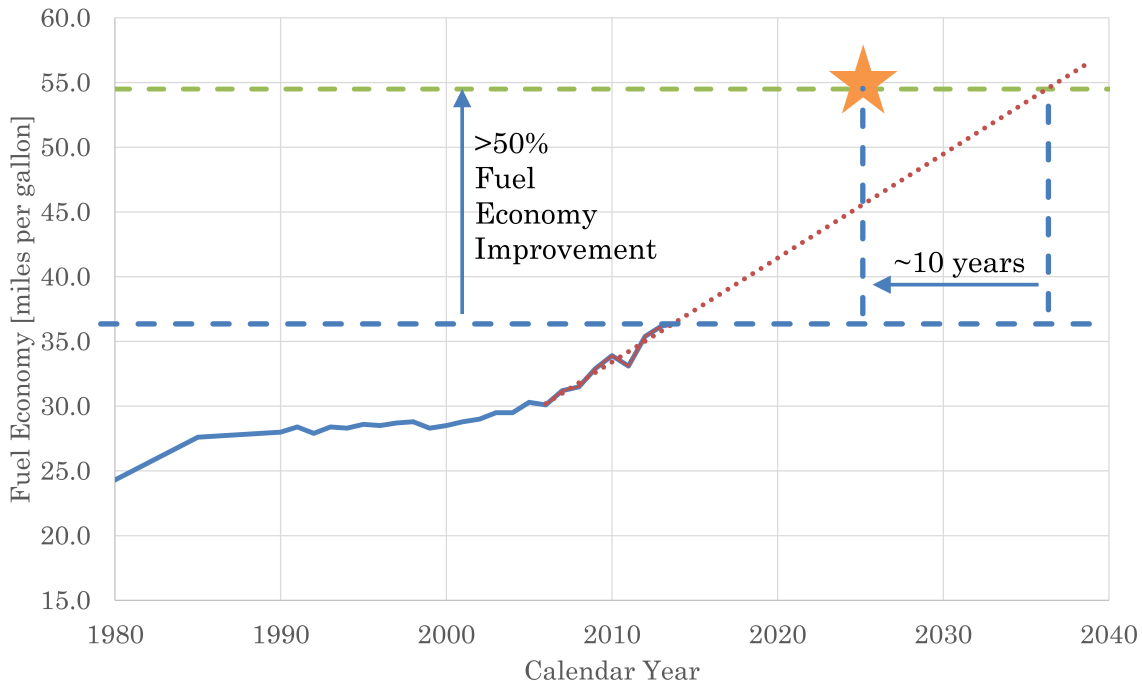
Figure 1.3: New light duty passenger vehicle fuel economy compared to fleet average with 2025 CAFE mandate highlighted. Data is sourced from the United States Department of Transportation [4].

French Neo-Platonist philosopher Bernard of Chartres's 12th century metaphorical concept of dwarfs standing on the shoulders of giants (nanos gigantum humeris insidentes) is best expressed in English by Sir Isaac Newton, "If I have seen further, it is by standing on the shoulders of Giants". In the truest of fashion, the insights and teaching provided by the experts of the combustion field have the paved the way to provide context for my work. The computational study of Lavoie et al. in 2012 [5] examined a series of six combustion modes and their effect on vehicle fuel economy gain. The outcomes of this study are of extreme importance here as they are the first of their kind to lay out the vehicle fuel efficiency benefit, from a thermodynamic perspective, of different combustion modes, as seen in Figure 1.4. The six combustion modes can be sub-divided into two categories, mode one and two encompass a naturally aspirated air charge induction system, and modes three through six encompass a forced induction air charge induction system coupled with downsized engine

displacement. Decreasing the engine displacement and boosting allows an engine to operate with fewer thermodynamic losses and closer to its optimum brake specific fuel consumption point for a larger portion of the simulated drive cycle. Most gasoline vehicles operating on the road today are running stoichiometric spark ignition combustion mode due to exhaust after treatment requirements of the three-way catalyst. Advanced combustion modes, operating in equivalence ratio space of $0.2 \leq \phi \leq 1.0$, could include combustion modes such as gasoline compression ignition or reactivity controlled compression ignition (RCCI). Homogeneous charge compression ignition (HCCI) is another combustion mode that could offer attractive vehicle fuel economy improvements, but has demonstrated significant control challenges in the past due to the chemical reactivity of the charge mixture [7,8]. The same chemical kinetics that enable the HCCI combustion mode are also sensitive to temperature stratification, thus yielding the combustion control difficulties previously mentioned. Ultimately, achieving a greater than 50% fuel economy improvement will require at least a lean spark ignition or advanced combustion mode to run lean and dilute, coupled with downsizing of engine displacement and forced induction. In summary the teachings of Lavoie et al. shed insights, from a thermodynamic perspective, on what type of combustion is necessary to achieve the required 50% vehicle fuel economy improvement, but leave the door wide open in terms determining a combustion strategy that will be controllable and operate in the proposed equivalence ratio space.

Advanced modes of internal combustion (IC) engine operation have potential to dramatically improve IC engine efficiencies while simultaneously lowering engine emissions [5, 9–12]. Advanced engine operating strategies include low temperature and fuel lean conditions, which enable higher compression ratios and may reduce the need for exhaust gas after-treatment [9–12]. Specifically, fuel lean combustion strategies are attractive methods to increase the thermal efficiency of gasoline, spark ignition, internal combustion engines, but engine design remains challenging because of the charge mixture lean flammability limits associated with traditional spark ignition systems. Turbulent jet ignition originating from a pre-chamber can help address mixture flammability limits by ejecting high enthalpy and highly reactive jets into the main combustion chamber, enabling overall lean combustion. Pre-chamber engine concepts are not a new technology to the automotive industry. H.R. Ricardo's internal combustion engine, documented in 1918, is the earliest pre-chamber concept found in the literature [13]. The pollution regulations of the 1970's brought renewed focus on the pre-chamber engine concept from research institutions and industry [14–22]. Most of the pre-chamber engine concepts suffered from atypical induction designs

that required complicated valvetrain arrangements [16]; however, recent advances in numerical simulations and computational resources allowed gasoline pre-chamber engine concepts to be systematically considered in new configurations. Naturally, one is led to ask can advanced pre-chamber engine concepts enable lean burn combustion with superior controllability than previous generations? In search of a response, a new engine concept is proposed in which the pre-chambers are indirectly fueled to improve pre-chamber mixture quality, thus eliminating wall wetting associated with previous designs and in turn improving tailpipe emissions by reducing particulate matter and unburned hydrocarbons. However, appropriate mixture conditions must be achieved in the pre-chamber and main chamber for this strategy to be successful.

CASE	Combustion Mode	Air Handling	Size	City/Hwy (mpg)	FE GAIN
1	Stoich-SI $(\Phi = 1.0)$	NA	3.3 L	25.4	BASE
2	Advanced $(0.2 \le \Phi \le 1.0)$	NA	3.3 L	31.3	23%
3	HCCI $(0.2 \le \Phi \le 0.45)$	TC	3.3 L	31.2	23%
4	Stoich-SI $(\Phi = 1.0)$	TC	1.4 L	34.5	36%
5	Lean-SI $(\Phi = 0.75)$	TC	1.4 L	36.7	44%
6	Advanced $(0.2 \le \Phi \le 1.0)$	TC	1.4 L	40.3	58%
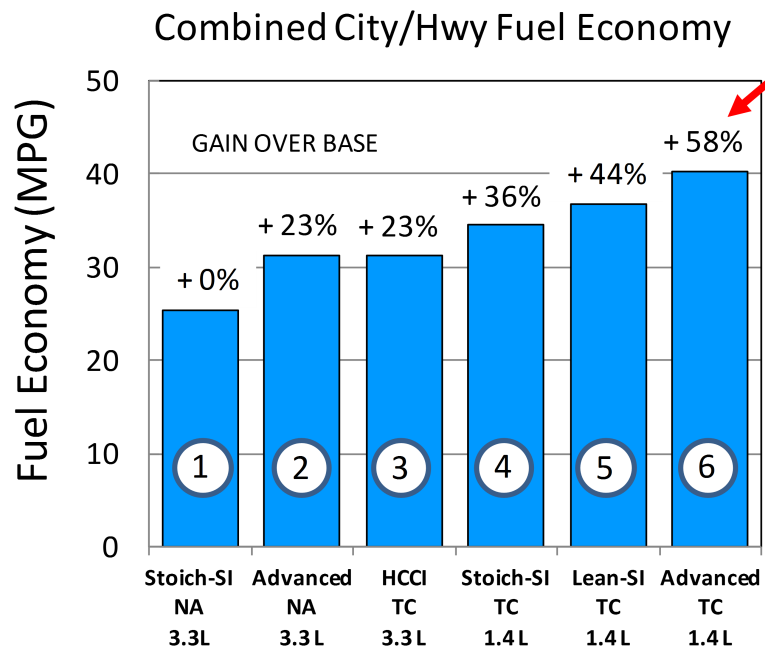
Figure 1.4: Results from the Lavoie et al. [5] computational study compare the effects of different combustion modes on vehicle fuel efficiency improvement. Figure adapted from Lavoie et al. [5].

1.2 Research Methodology

The objective of this thesis is to demonstrate the feasibility and flammability limits of dilute lean burn combustion and to harvest this knowledge to design a pre-chamber engine with potential to significantly improve thermal efficiencies of spark-ignited engines. This will be achieved by performing experimental and computational studies of dilute lean burn combustion and fuel / air preparation strategies in fundamental devices and practical engine implementations.
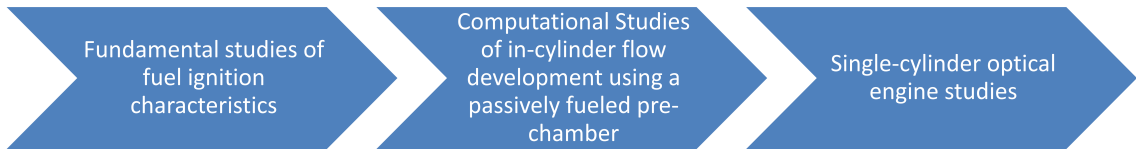
Figure 1.5: Overview flow schematic of the research studies performed in this document.

This thesis work starts with fundamental experimental studies of fuel ignition characteristic in a rapid compression facility (RCF). The question being answered here is what are the flammability limits of dilute, lean combustion of iso-octane (gasoline) /air mixtures. These fundamental experiments are necessary to be performed in an RCF as there is a need to isolate specific chemical mechanisms of ignition with simplified fluid mechanics, thus removing fuel mixing and turbulence effects commonly convoluted in engine experiments, at state and mixture compositions relevant to piston engine conditions. The goals of theses fundamental experiments are to demonstrate a flame can be initiated and propagated at fuel lean and dilution conditions and to quantify sensitivity of lean limits to state and composition conditions.

Next, computational studies of in-cylinder flow development using a passively fueled pre-chamber are performed using three-dimensional computational fluid dynamics (CFD) software. This portion of the work is trying to understand if there is a feasible range of lean mixture conditions that can be achieved using practical engine hardware and what range of mixture and stratification control can be anticipated. In this phase, there is a need to identify key design aspects to create dilute lean burn combustion in a piston spark ignition engine. The objectives of the computational studies are to demonstrate the superposition of fuel/air equivalent ratio can be achieved in the pre-chambers using a dual injection strategy and to quantify the sensitivity to breathing and fueling strategies.

Finally, the single cylinder optical studies are performed to determine if the CFD predicted fuel spray and flow-field are achievable and if indeed they can yield the

targeted mixture preparation in a real engine with a passively fueled pre-chamber. There is a key need to identify fuel/air mixture preparation robustness to determine a feasible engine operating envelope. To achieve this, the physical preparation of fuel/air mixtures needs to be demonstrated, as well as an appropriate mechanism to control the fuel/air mixture preparation must be demonstrated.

1.3   Executive Summary

Advanced modes of internal combustion (IC) engine operation have potential to dramatically improve IC engine efficiencies while simultaneously lowering engine emissions [5,9–12]. Advanced engine operating strategies include low temperature and fuel lean conditions, which enable higher compression ratios and may reduce the need for exhaust gas after-treatment [9–12]. Specifically, fuel lean combustion strategies are attractive methods to increase the thermal efficiency of gasoline, spark ignition, internal combustion engines, but engine design remains challenging due to two major factors associated with the lean flammability limits of the fuel/air mixture. There is a significant lack of fundamental combustion data, such as flame speeds and flammability limits at the state and reactant mixture conditions important to advanced combustion in IC engines. Consequently, the objective of this thesis starts by experimentally characterizing flame speeds, flammability limits, and the interaction between flames and autoignition events of lean iso-octane (an important gasoline reference fuel) and air mixtures at premixed, moderate temperature (925 – 1000 K) and pressure (> 7.5 atm) conditions relevant to advanced engine combustion strategies. Chapter 2 describes the results of this experimental study of lean flammability limits. Chapters 3 – 6 describes the results of the application of the fundamental understanding of lean combustion to modern engine design. Specifically, in recent years, pre-chambers have been shown to enable advanced combustion modes in reciprocating engines. As part of this dissertation, a dual pre-chamber (DPC) engine was designed and built which leveraged our understanding of extending lean combustion limits. The project was a collaboration between the University of Michigan (UM) and Hyundai-Kia America Technical Center, Inc (HATCI). After a thorough review of the literature to assess the potential of pre-chamber systems, the first phase of the project used computational fluid dynamics (CFD) simulations to develop a new engine design (described in Chapter 3). The goal of the simulations was to demonstrate a novel concept of passive fueling of the pre-chambers while simultaneously fueling the main combustion chamber. The outcomes of the simulation research included recommendations

for the dimensional geometry of a prototype DPC engine and fuel injection strategies to achieve the fueling goals. The next phase of the project is described in Chapters 4 and 5 and presents the results of building and evaluating a physical prototype of the DPC engine. The objective of the engine build was to demonstrate the flow dynamics predicted by the CFD model. The prototype single-cylinder DPC engine was built and installed at the UM. In addition to the engine head, piston, fuel injector, and other hardware required, a metal cylinder liner was machined and used to statically and dynamically test the engine. Details on the engine hardware and testing are found in Chapters 4 and 5. A fully transparent fused silica cylinder liner was also fabricated for imaging studies of the fuel and air flow. High-speed imaging captured fuel injection events at different injection timings and the air charge motion (via water vapor condensation). Results of the imaging study are presented in Chapter 5. The features of the fuel and air flow were considered vital based on the CFD results to passively fuel the pre-chambers. The fuel spray data are the first *in situ* measurements of the unique fueling strategy and unique hardware. Conclusions of the dissertation and recommendation for future work are presented in Chapter 6.

CHAPTER II

Experimental Investigation of Flame Autoignition Interactions

2.1 Abstract

Recent modifications to the University of Michigan rapid compression facility (UM RCF) were made to allow direct imaging of flame/autoignition interactions using compression to initiate autoignition chemistry and a spark plug to initiate simultaneous flame development. The experimental data in this study quantify the effects of spark-initiated flame propagation on autoignition of iso-octane / O_2 / inert gas mixtures at well-defined initial conditions. The work leveraged the controlled environment of the UM RCF, in which temperature, pressure, and composition are nominally uniform and well-known at the end of compression. Flame initiation by the spark plasma, flame propagation, and autoignition were monitored using high-speed optical imaging of chemiluminescence and in situ pressure time histories. End-of-compression temperatures from T_{EOC} = 942 - 1018 K were considered, while the end-of-compression pressures were nominally constant within the range of P_{EOC} = 7.8 – 9.5 atm. The fuel-to-O_2 molar equivalence ratio was varied from ϕ = 0.20 - 0.99 and dilution, defined as the molar ratio of inert gases to O_2 in the reactant mixture, was varied from inert:O_2 = 3.76 - 7.47 to determine the effects on flame/autoignition interactions as well as to identify the lean flammability limit of the mixtures as a function of dilution. Flame propagation is generally expected to decrease autoignition delay times

by compression heating the unburned portion of the mixture. The effect of flame propagation was maximized in these experiments by igniting the mixtures early during the autoignition process. Later spark timings had small to negligible effect on the autoignition delay time. Dilution had significant effect on the lean flammability limits, increasing from a lean limit of $\phi = 0.35$ at air levels of dilution to $\phi = 0.65$ at inert:O_2 dilution of 7.5. The flammability limit was well correlated with the theoretical adiabatic flame temperature of each experiment. The propagation rates of flames successfully initiated by the spark plasma were determined from the imaging data and were $\sim 1 - 12$ m/s. The magnitude of the propagation rates and the effect on the time integrated temperature scaled with the energy content of the mixtures as indicated by the theoretical adiabatic flame temperature.

2.2   Introduction

Advanced modes of internal combustion (IC) engine operation have potential to dramatically improve IC engine efficiencies while simultaneously lowering engine emissions [5, 9–12]. Advanced engine operating strategies include low temperature and fuel lean conditions, which enable higher compression ratios and may reduce the need for exhaust gas after-treatment [9–12]. Homogeneous charge compression ignition (HCCI) is a low temperature combustion strategy that has been the focus of numerous experimental and computational studies in the past decade. Several excellent articles review research progress on HCCI and other advanced engine strategies including discussions of important limitations of current scientific understanding [9,12], demonstration of operating modes [9,11,12], and advances (existing and required) in related engine technology [9,11,12].

Methods of advanced combustion in IC engines often encompass mixed modes of combustion, in which flames and autoignition processes are simultaneously contributing to combustion and heat release rates. For example, during spark-assisted compression ignition (SACI), a spark plug is used to initiate a flame into the nominally homogeneous or partially stratified fuel/air charge in an internal combustion engine. SACI has been demonstrated to expand high and low load operation beyond HCCI boundaries [23–25]. However, methods to optimize SACI and other mixed modes of combustion are limited by the lack of fundamental understanding of flame propagation and autoignition interactions at conditions relevant to advanced engine strategies. Moreover, advanced combustion strategies like HCCI, SACI and gasoline direct injection (GDI) often consider highly dilute operation as a means to

achieve high efficiency goals and meet emerging and more strict emissions require-
ments. These strategies typically target either (globally) fuel lean or stoichiometric
conditions. The combination of high levels of dilution and fuel lean reactant mix-
tures is particularly challenging, as flame propagation and heat release rates decrease
dramatically compared to undiluted stoichiometric conditions.

There is also a significant lack of fundamental combustion data, such as flame
speeds and flammability limits at the state and reactant mixture conditions impor-
tant to advanced combustion in IC engines. This gap complicates optimizing engine
operation, especially the development and validation of theory and models which ac-
curately describe mixed modes of combustion like SACI. Consequently, the objective
of the current study is to experimentally characterize flame and autoignition inter-
actions of iso-octane (an important reference fuel) and air mixtures at premixed,
moderate temperature (925 – 1000 K) and pressure (>7.5 atm) conditions relevant to
advanced engine strategies. The technical approach of this study leverages the well-
defined mixture and state conditions that can be created using a rapid compression
facility (RCF). Previous studies have demonstrated the value of RCFs as experimen-
tal platforms for providing important insights into the effects of mixture stratification
on spark ignited flames during direct injection of the fuel [26–30]. Much has been
learned from these previous RCF studies, including the effects of spark and fuel tim-
ing on mixture stratification and the resulting flame propagation [26–30]. The focus
in the current work differs fundamentally from these previous studies as the focus is
on flame/autoignition interactions at conditions with nominally homogeneous initial
conditions, where thermal and mixture stratification have been minimized prior to
spark igniting the mixture. Specifically, the effects of flame propagation on the au-
toignition delay time are determined in this study and the flammability limit for lean,
dilute, premixed iso-octane air mixtures is determined. Measurements of flame prop-
agation rates were also made for mixtures in which flames were successfully initiated
and sustained in the test gas mixture.

2.3   Experimental Approach

All experiments were conducted using the University of Michigan rapid compres-
sion facility (UM RCF) which has been used for numerous autoignition studies, in-
cluding extensive characterization of iso-octane autoignition [6, 31–33]. The UM RCF
is essentially a chemical reactor that creates nominally uniform temperature and pres-
sure conditions using a free piston to compress a test gas mixture. The test section of

the UM RCF provides excellent optical and physical access to interrogate the gases during autoignition. The technical approach used in this study compared autoignition data with and without using a spark plug to initiate flames during the ignition delay time. The autoignition characteristics of the mixtures were determined using the pressure time history, and the characteristics of flame propagation were determined using high-speed imaging. The spark/autoignition experiments were also used to identify flammability limits as a function of dilution for fuel lean iso-octane air mixtures.

2.3.1 Rapid Compression Facility Details

Details of the dimensions, operating procedure, and results of RCF characterization studies have been described previously and can be found in Donovan et al. [34] and He et al. [31]. The key features are highlighted here: The UM RCF consists of a driver section, driven section, test section, a sabot or free piston, a globe valve, and a mixing manifold. The driver section is separated from the driven section by a fast acting hydraulic globe valve assembly. Due to the high pressure differential across the globe valve assembly, a thin (0.05 mm thick) and scored plastic (Mylar) sheet is placed between the vacuum side of the valve assembly and the driven section to prevent air leaking into the evacuated driven section. The RCF achieves desired thermodynamic conditions through compression heating of the test-gas mixture by the sabot. The sabot consists of a solid plastic (Delrin) body with a brass counterweight located in the posterior and a detachable disposable nosecone made of deformable ultra-high molecular weight polyethylene. The sabot design includes two u-ring seals to minimize blow-by of the driver gases into the driven section during compression of the test-gas mixture.

As shown in Figure 2.1, downstream of the driven section is the test manifold, which consists of the converging, extension, and test sections. The converging section traps the cold boundary layer gases outside the test section to maximize test times at high temperatures and pressures, by minimizing fluid mixing and heat losses. The critical dimensions of the extension section are the internal diameter of 5.08 cm and the axial length of 8.05 cm.

A new test section was fabricated from 316L stainless steel for this study to allow a spark plug to be mounted in the test section. The critical dimensions of the test section are the internal diameter of 5.08 cm and the axial length of 5.88 cm. For each experiment, the sealed test volume consists of the test section volume and part of the extension section volume. The nosecone seals the test section by an annular

interference fit in the extension section, resulting in a nominal test volume of 186.1 cm^3. The test section is sealed using a polycarbonate endwall, 12.7 mm thick, and a load distribution plate that allows optical access for end-view imaging. Polycarbonate is more durable than quartz and polycarbonate provides comparable transmission efficiency to quartz in the visible spectrum, where the transmission efficiency of quartz is $\sim 90\%$ and of polycarbonate is $85 - 90\%$ in the wavelength range 390 - 700 nm.
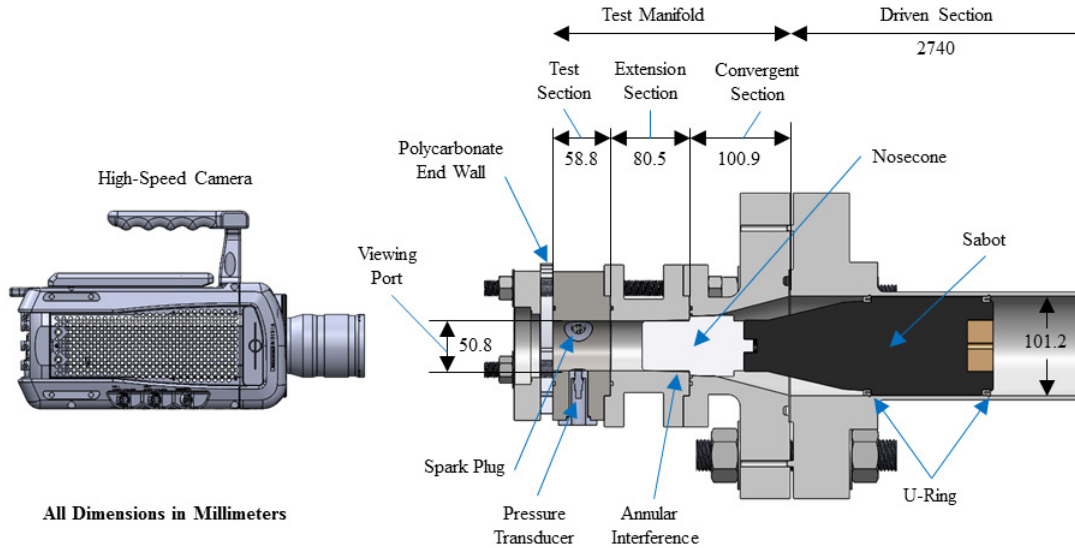
Figure 2.1: Side-view cross-section schematic of the UM RCF showing the driven section, the test manifold, and the high-speed camera. The sabot location corresponds to the end of compression in the test section.

The pressure time histories for each experiment were measured using an amplified high-speed transient piezoelectric pressure transducer (Kistler 6045A transducer and Kistler 5010B charge amplifier). As shown in Figure 2.1 and Figure 2.2, the pressure transducer was mounted on the bottom of the test section (i.e. at the piston or end view 6 o'clock position), and the spark plug was mounted at the 11 o'clock position. The orientation of the transducer and spark plug are not expected to effect the results of this study. The information is provided to orient the imaging data. All data except the camera imaging results were recorded using a 32 bit data acquisition system (National Instruments cDAQ-9172) operating at 100 kHz and collected using a custom data acquisition program (LabView, 2011).

2.3.2 Spark Ignition System Details

The spark ignition system used in this study is similar to traditional electronic ignition systems used in automotive applications. The spark plug is a production
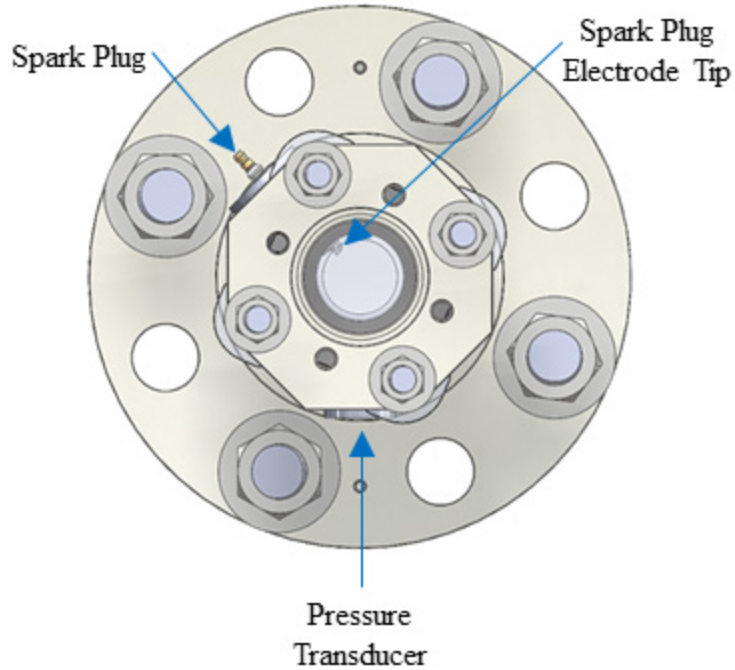
Figure 2.2: End-view schematic of the UM RCF showing the driven section and the test manifold. The sabot location corresponds to the end of compression in the test section.

flat seat iridium tip model (NGK IX BKR6EIX-11) set with a 1.1 mm gap between the central and ground electrodes. The central electrode sits 5 mm proud relative to the wall of the test section. An ignition module (Wells DR178) was used to signal an ignition coil (Accel 140024) with a maximum discharge voltage of 48,000 V. The ignition coil was powered by a regulated power supply capable of 12 A output (Pyramid PS-14KX 13.8 V) and connected to the spark plug using a spiral wound, silicone-sleeved, low resistance conducting spark plug wire. The amount of spark discharge energy was not changed throughout the experimental study. Thus, within the tolerance expected for a typical production automotive ignition system, the spark discharge energy remained constant for every experiment. The minimum ignition energy for each mixture composition will vary to some degree. The results may therefore be sensitive, to some extent, to the amount of ignition energy introduced to the test-chamber.

The ignition module was triggered by the falling edge of a 2.5 V, 2 ms square wave produced by a digital delay/pulse generator (Stanford Research, Inc. DG535). The combined resistance of the secondary coil, insulated connecting wire, and the spark plug was measured to be 14.25 kΩ. The timing of the spark discharge was targeted to

occur at the end of the first quartile of the predicted ignition delay time as determined by evaluating the Walton et al. [6] iso-octane correlation at the targeted experimental conditions. This methodology ensured the spark discharge occurred after the end of compression by the sabot and early during the autoignition delay time, to allow the maximum time for a potential flame to propagate.

2.3.3 High-Speed Imaging System Details

A high-speed color digital video camera (Vision Research Phantom v711) was located downstream of the transparent end wall along the axis of the test section to record end-view imaging during the experiments. The high-speed camera featured a 1280 x 800 pixel CMOS sensor (Vision Research) with a 7 gigapixel/second throughput capable of recording from 7,530 frames per second (fps) at a maximum resolution of 1280 x 800 pixels to 680,000 fps at a maximum resolution of 128 x 8 pixels. The CMOS sensor used a combination of four filters to achieve particular spectral response resulting in red, green, and blue output signals. The blue signal was acquired using a bandpass filter with peak transmittance at 455 nm and half-power transmittance at wavelengths of 406 nm and 508 nm. The green signal was acquired using a bandpass filter with a peak transmittance at 540 nm and half-power transmittance at wavelengths of 478 nm and 596 nm. The red signal was acquired using a bandpass filter with peak transmittance at 636 nm and half-power transmittance at wavelengths of 579 nm and 660 nm. A low-pass filter with a cutoff frequency of approximately 715 nm was used to attenuate infrared emission. The camera lens assembly included a 50 mm high-speed lens (Navitar DO-5095 f/0.95), a 62 mm magnification lens (Hoya +4) to decrease the depth of field, and a 62 mm lens (Hoya Pro1 Digital Filter) to reduce internal light scattering and reflections in the lens assembly. The front lens element (Navitar DO5095) is made of single anti-reflective coating glass that can reflect up to $4 - 5\%$ of incoming light. The digital filter (Hoya Pro1) is a multi-coated filter that features three layers of anti-reflective coating, thus reducing the reflected light to just $1 - 2\%$ of incoming light. Internal light scatter, caused by stray reflected light, should be reduced because stray light can hit the CMOS sensor and create non-physical effects such as flares or ghosting. The camera was triggered using a digital delay/pulse generator (Stanford Research, Inc. DG535). The recording time was centered on the end of compression (i.e. the nosecone seating event) by applying a delay of 6.5 ms from when the digital delay/pulse generator was initially triggered by the sabot.

Camera software (Vision Research Phantom Software PCC 2.0.717.0) was used to set-up, calibrate, and capture all relevant videos. The camera was focused on the

plane of the spark plug electrode prior to every experiment using a high exposure setting and corresponding low frame rate setting. A digital white-balance was performed as necessary using a white calibrating sheet of paper to ensure the red, green, and blue signals were balanced in magnitude. The exposure was decreased until the sensor did not detect any pixel saturation; at this point, the digital white balance was performed through the software. The camera settings were then adjusted to the appropriate resolution (512 x 512 pixels), frame rate (10,000 fps), and exposure (99.64 μs) settings for the experiments. For the settings applied in this study, one pixel is equal to approximately 0.1 x 0.1 mm. The zero signal level for the CMOS array was calibrated with the lens cap on the camera using the current session reference function of the camera control software.

The high-speed videos were analyzed frame-by-frame using a combination of the camera specific software (Phantom SDK 12.0.705.0) and algorithms developed for this work and implemented in Matlab (R2012a). The image analysis was used to determine the location of the flame front in each image, for experiments where a flame was successfully initiated. For each experiment, a threshold was applied to convert the color images to binary scale, and an origin was defined as the centroid of the spark discharge. Vectors originating from the centroid were used to determine the location of the flame front in each frame. As will be shown later, the flames were often irregular in shape, and apparent flame propagation rates were determined along the measurement vectors from the time histories of the flame front location

2.3.4 Experimental Procedure

The test gas mixtures were made in a stirred mixing tank external to the RCF. A manifold was used to prepare the test gas mixtures using ultra high-purity components. The purity and source of the reactants are provided in Appendix A. The partial pressures of the gases (0 – 100 torr and 0 – 1000 torr) were measured using two capacitance diaphragm pressure gauges, respectively (Varian CeramiCel VCMT12TFA and VCMT13TFA). The partial pressures were varied in different mixtures to achieve the targeted fuel-oxygen equivalence molar ratio, ϕ, and inert gas to oxygen, $I : O_2$, molar ratio. Each test gas mixture was stirred at 500 revolutions per minute (rpm) for a minimum of 20 minutes to ensure mixture homogeneity.

After the test gas mixture was prepared, each ignition experiment used the following process. The sabot was placed at the upstream end of the driven section. The driven section was evacuated and then filled with the test gas mixture to an initial pressure of $P_0 = 63.6 – 67.3 \pm 0.3$ torr. The hydraulic globe valve was actu-

ated, launching the sabot down the length of the driven section until the nosecone of the sabot seated via an interference fit in the extension section. The RCF was disassembled, cleaned, and re-assembled between each experiment.

A laser diode (50 mW, 532 nm) paired with a photodetector (Hamamatsu S1787-12) were located slightly upstream of the test section (aligned orthogonal to the axis of the RCF) and used to determine the time the sabot passed the laser diode/photodetector location. When the sabot passed the measurement port (and blocked the laser beam), a signal was sent from the photodetector to trigger two digital delay/pulse generators (Stanford Research, Inc. DG535) that in turn triggered the spark and data acquisition systems. The effect of changing the spark timing on the lean flammability was investigated for some experiments. The time of the spark discharge was varied from the end of the first, second, and third quartiles of the predicted autoignition delay time. No effect of spark timing was observed on the lean flammability limit. For the majority of the experiments, the spark timing was set for the end of the first quartile of the predicted ignition delay time, in order to maximize the time for flame propagation and therefore maximize the effects of flame propagation on autoignition.

2.4 Results

2.4.1 Flame Effects on Test Gas Conditions

Experiments were conducted over a range of mixture compositions, targeted temperatures and pressures, and with and without the use of the spark plug to initiate flames. Figure 2.3, on the next page, shows typical pressure time history and imaging results for an experiment in which the spark system was applied. The results are for a mixture with an inert gas to oxygen ratio of $I : O_2 = 4.99$ (mole basis) and a fuel to oxygen equivalence ratio of $\phi = 0.99$ (mole basis). The pressure and pressure derivative time histories are shown in the upper panel. Select frames from the imaging sequence are shown in the lower panel. The images in the figure are color enhanced for clarity, and not all frames in the video file are presented. The end of compression (EOC) pressure for the experiment is $P_{EOC} = 8.4$ atm and the EOC temperature is $T_{EOC} = 976$ K, as determined by numerical integration of the isentropic compression relation Eqn. 2.1

$$\int\limits_{T_0}^{T_{EOC}} \frac{\gamma}{\gamma - 1} \, d\ln(T) = \ln(\frac{P_{EOC}}{P_0}) \tag{2.1}$$

where P_0 is the initial charge pressure, T_0 is the initial charge temperature (typically 298 K), and γ is the temperature dependent ratio of the specific heats of the unreacted mixture, which is determined using the NASA Thermodynamic Data Base [35].
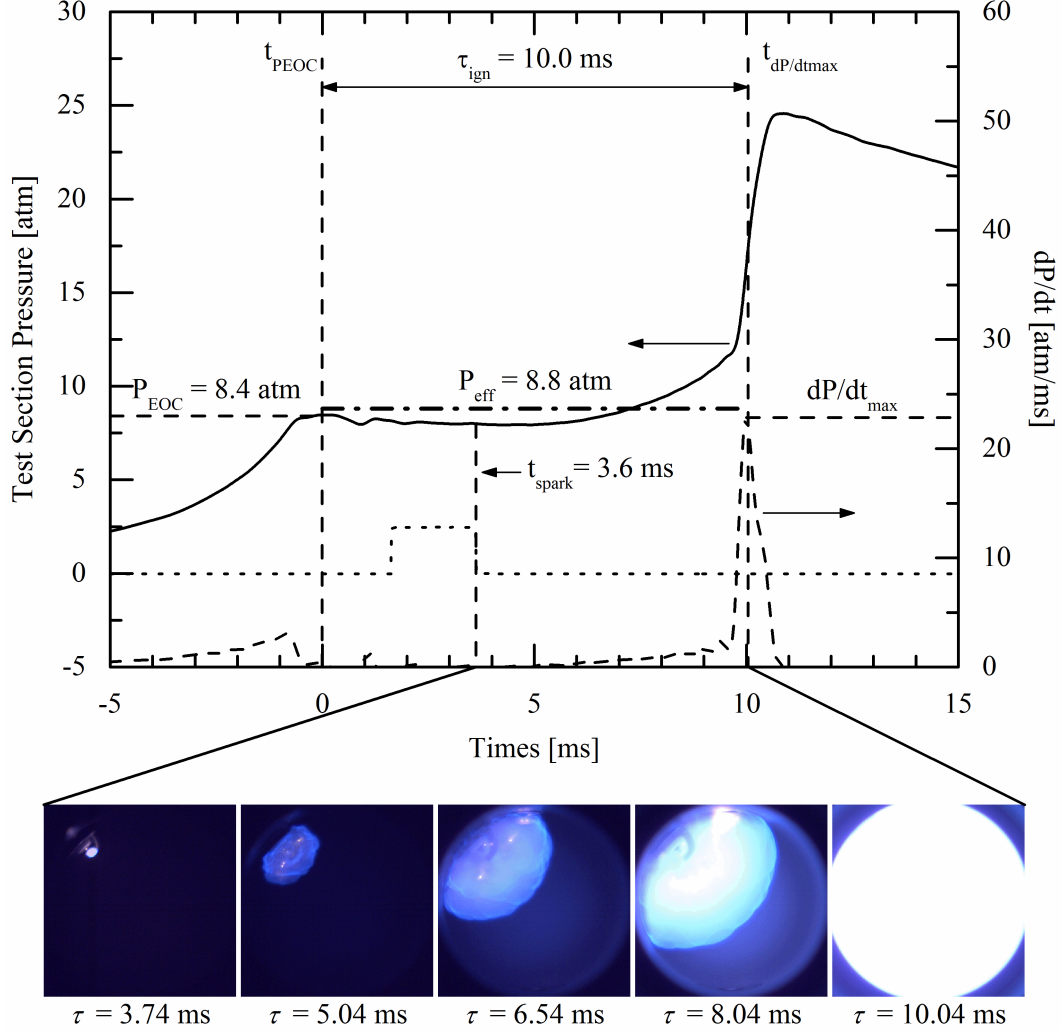
Figure 2.3: The top panel presents the pressure and pressure derivative time histories for a typical iso-octane autoignition/flame interaction experiment ($I : O_2 = 4.99$, $\phi = 0.99$, $T_{EOC} = 976$ K, and $P_{EOC} = 8.4$ atm). The lower panel presents selected frames from the video sequence. The spark triggering signal (arbitrary units) is included for reference as the dotted line.

In Figure 2.3, EOC is set as time t = 0, and volumetric autoignition of the mixture is indicated by the maximum rate of pressure rise after the EOC, $\frac{dP}{dt}max$. Volumetric autoignition also corresponds with the high intensity chemiluminescence that fills the imaging window in the last frame of the sequence presented in the lower panel of Figure 2.3. The autoignition delay time, τ_{ign}, is determined from the pressure and

pressure derivative time histories as the elapsed time between the P_{EOC} and maximum rate of pressure rise, $\frac{dP}{dt}max$, as shown in Figure 2.3.

The effects of the spark are evident in the pressure time history and the imaging sequence. The compression process prior to the EOC is smooth. Immediately following EOC, there is a slight observable decrease in the test section pressure caused by cooling of the test gases due to the colder test section walls. The decaying oscillatory behavior in the pressure signal, observed temporarily after the EOC, is an artifact of the fast Fourier transform filter used to reduce the noise recorded by the pressure transducer which originates from the impact of the nosecone seating. The spark trigger signal is included for reference in the upper panel of Figure 2.3 as the dotted line (arbitrary units). The falling edge of the spark trigger signal occurs at t = 3.63 ms, and the spark plasma appears within approximately 110 μs of the trigger signal in this experiment. A flame kernel is initiated by the spark discharge, and a flame propagates outward from the spark electrode. Within approximately 1 ms of the falling edge of the spark signal, the pressure in the test section starts to increase. The rate of pressure rise steadily increases prior to volumetric ignition, and as seen in the imaging data, the pressure rise correlates with the progress of the flame propagation through the test gas mixture. The increase in pressure prior to volumetric autoignition is primarily associated with compression heating of the remaining unburned mixture by the spark initiated flame. Pressure rise can also occur due to exothermic reactions during the autoignition delay time. As will be shown below, the chemical contribution can be small relative to the effects of compression heating; however, the relative contributions will be a function of the volume of the test section and the energy content of the mixture.

EOC conditions are appropriate initial conditions for each experiment and a summary of the EOC conditions is provided in Table 2.1. Additionally, in previous UM RCF autoignition studies [6,36], time-integrated values for pressure and temperature were found to represent the test conditions quite well, in terms of correlating τ_{ign} data with the average state conditions experienced by the unburned mixture throughout the autoignition delay time period. In this study, the time integrated conditions are outcomes of the flame and autoignition interactions for a specific set of mixture composition, spark timing, and EOC conditions. As seen in Figure 2.3, using the EOC conditions to define the state conditions of the experiment would improperly estimate the pressure (and consequently the temperature) of the gases in the test section at the time of volumetric autoignition. For these experiments, the time-integrated values capture the effects of heat losses as well as the (potentially offsetting) effects of

compression heating due to flame propagation. Thus, the effective state conditions reported in the current work are results of each flame/autoignition interaction experiment, and the effective conditions reflect the extent to which the EOC conditions have been affected by flame propagation and heat losses and flame propagation.

As in previous UM RCF studies [6,36], the effective pressure, P_{eff}, for each experiment is defined as the time-integrated average pressure from the maximum pressure due to compression (P_{EOC}) to the time of maximum rate of pressure rise, $\frac{dP}{dt}max$, or

$$P_{eff} = \frac{1}{t_{\frac{dP}{dt},max} - t_{P_{EOC}}} \int_{t_{P_{EOC}}}^{t_{\frac{dP}{dt},max}} P\, dt \qquad (2.2)$$

The corresponding effective temperature, T_{eff}, for each experiment is determined using the same form as Eqn. 2.1, in which the end of compression parameters are replaced with the effective pressure and temperature:

$$\int_{T_{eff}}^{T_0} \frac{\gamma}{\gamma - 1} d\ln(T) = \ln(\frac{P_{eff}}{P_0}) \qquad (2.3)$$

For reference, the effective conditions for the results presented in Figure 2.3 were $P_{eff} = 8.8$ atm, and $T_{eff} = 985$ K, and the EOC conditions were $P_{EOC} = 8.4$ atm, and $T_{EOC} = 976$ K.

Table 2.1: Summary of experimental conditions and results for autoignition/flame interaction experiments. The mixture composition is provided on a mole basis. The equivalence ratio is based on iso-octane to O2 molar ratios. Experiments in which flames were successfully initiated by the spark discharge include the average propagation rate of the flames, U_{avg}. Experiments in which flames are not successfully initiated by the spark are denoted as below the flammability limit, BFL. Experiments in which flames are successfully initiated but apparent flame speed measurements were not performed are denoted as above the flammability limit, AFL.

ϕ	inert $I:O_2$	$\chi_{i-C8H18}$ [%]	χ_{O2} [%]	χ_{N2} [%]	χ_{Ar} [%]	T_{EOC} [K]	P_{EOC} [atm]	T_{eff} [K]	P_{eff} [atm]	τ_{ign} [ms]	τ_{spark}[b] [ms]	U_{avg} [m/s]	T_{ad}[c] [K]	density ratio[d] $[\frac{\rho_B}{\rho_U}]$	Cv[e] $[\frac{J}{mol-K}]$
0.20	3.76	0.33	20.94	75.14	0.01	988	8.9	966	8.1	30.5	11.9	BFL	1600	0.61	26.93
0.30	4.98	0.40	16.66	80.72	2.23	998	8.3	983	7.8	23.8	7.3	BFL	1743	0.56	26.15
0.30	3.76	0.50	20.90	77.90	0.00	977	8.4	959	7.8	26.1	9.0	BFL	1879	0.51	26.95
0.30	3.76	0.50	20.90	77.90	0.01	988	8.8	968	8.1	20.9	8.8	BFL	1888	0.51	27.02
0.40	3.76	0.66	20.87	74.71	3.76	978	8.6	965	8.1	20.5	7.0	1.4	2152	0.44	27.03
0.40	4.99	0.53	16.60	82.51	0.00	985	8.7	964	8.0	26.0	9.9	BFL	1934	0.50	26.95
0.49	4.98	0.66	16.61	79.31	3.43	976	8.4	965	8.0	22.9	9.4	1.5	2144	0.44	26.97
0.49	7.46	0.47	11.77	83.88	3.88	1000	8.4	986	7.9	26.3	9.2	BFL	1870	0.53	26.15
0.50	3.76	0.83	20.84	68.83	9.51	978	8.4	980	8.5	13.8	4.9	3.1	2415	0.39	27.06
0.50	3.76	0.83	20.84	68.83	9.50	986	8.8	978	8.4	14.9	4.6	2.7	2420	0.40	27.11
0.50	4.98	0.66	16.60	79.31	3.43	976	8.5	959	7.9	27.1	10.1	0.9	2146	0.44	26.96
0.50	4.99	0.66	16.58	81.31	0.00	953	8.5	933	7.8	38.2	14.1	1.3	2098	0.44	27.51
0.50	4.99	0.66	16.58	81.31	0.01	954	8.6	936	7.9	35.7	13.6	1.5	2098	0.44	27.52
0.50	4.99	0.66	16.58	78.60	4.16	957	7.8	954	7.7	27.4	5.1	1.5	2135	0.44	26.75
0.50	4.99	0.66	16.58	72.50	10.26	996	8.2	985	7.8	18.1	6.2	2.2	2198	0.44	26.28
0.50	7.47	0.47	11.76	86.64	0.00	978	8.4	960	7.7	38.2	12.3	BFL	1828	0.53	26.72
0.59	7.47	0.56	11.74	87.22	0.01	979	8.4	956	7.7	37.2	9.9	BFL	1977	0.49	26.96

ϕ	inert $I:O_2$	$\chi_{i-C_8H_{18}}$ [%]	χ_{O_2} [%]	χ_{N_2} [%]	χ_{Ar} [%]	T_{EOC} [K]	P_{EOC} [atm]	T_{eff} [K]	P_{eff} [atm]	τ_{ign} [ms]	τ_{spark}^{b} [ms]	U_{avg} [m/s]	T_{ad}^{c} [K]	density ratio^d $[\frac{\rho_B}{\rho_U}]$	Cv^e $[\frac{J}{mol-K}]$
0.60	4.99	0.79	16.56	75.81	6.84	990	8.9	972	8.3	18.9	6.3	2.1	2360	0.41	27.19
0.69	4.99	0.92	16.54	71.14	11.40	983	8.8	979	8.6	14.6	5.0	3.1	2541	0.37	27.15
0.69	7.45	0.65	11.76	84.65	2.94	974	8.3	954	7.7	37.8	11.3	1.6	2132	0.45	26.86
0.69	7.47	0.65	11.74	85.01	0.01	950	8.5	930	7.8	52.2	14.8	0.9	2077	0.45	27.59
0.70	4.99	0.92	16.54	76.87	5.68	942	8.1	945	8.2	26.9	11.1	2.7	2480	0.37	27.53
0.73	7.41	0.69	11.80	83.12	4.38	986	9.0	974	8.6	24.3	6.4	AFL	2212	0.43	26.93
0.73	7.42	0.69	11.79	83.13	4.38	977	8.7	974	8.5	23.2	6.0	AFL	2206	0.43	26.87
0.73	7.42	0.69	11.80	78.34	9.17	1012	9.2	1005	9.0	14.7	4.1	AFL	2259	0.44	26.52
0.74	7.43	0.69	11.78	83.13	4.39	985	8.9	969	8.3	27.1	17.7	AFL	2214	0.43	26.92
0.74	7.43	0.69	11.79	83.13	4.39	998	9.5	980	8.8	22.0	6.2	AFL	2225	0.44	27.01
0.74	7.43	0.69	11.78	78.34	9.19	1012	9.2	1005	8.9	15.0	8.0	AFL	2262	0.44	26.52
0.74	7.44	0.69	11.77	83.14	4.39	984	8.9	968	8.3	29.4	12.1	AFL	2213	0.43	26.92
0.79	7.46	0.74	11.73	82.84	4.68	978	8.4	966	8.1	27.5	7.3	1.7	2280	0.42	27.05
0.99	3.76	1.64	20.66	44.18	33.52	972	8.3	1002	9.5	5.0	1.3	11.7	3119	0.28	27.56
0.99	4.99	1.31	16.47	59.11	23.11	976	8.4	985	8.8	10.0	3.6	6.1	2892	0.32	27.35
0.99	7.46	0.93	11.71	77.10	10.26	974	8.3	974	8.4	21.5	4.9	2.1	2509	0.37	27.16

^{a} Balance CO_2.

^{b} Time from the end of compression to the falling edge of the spark trigger signal. See text for details on how spark timing was selected.

^{c} Adiabatic flame temperatures were calculated assuming a constant volume using the initial reactant composition and the end of compression temperature and pressure for each experiment.

^{d} The density ratio was calculated based on the initial reactant mixture and effective conditions of the unburned gasses (ρ_U) and the theoretical mixture composition and effective conditions of the burned gases (ρ_B).

^{e} The mixture heat capacity was calculated based on the initial reactant mixture and the end of compression temperature (T_{EOC}).
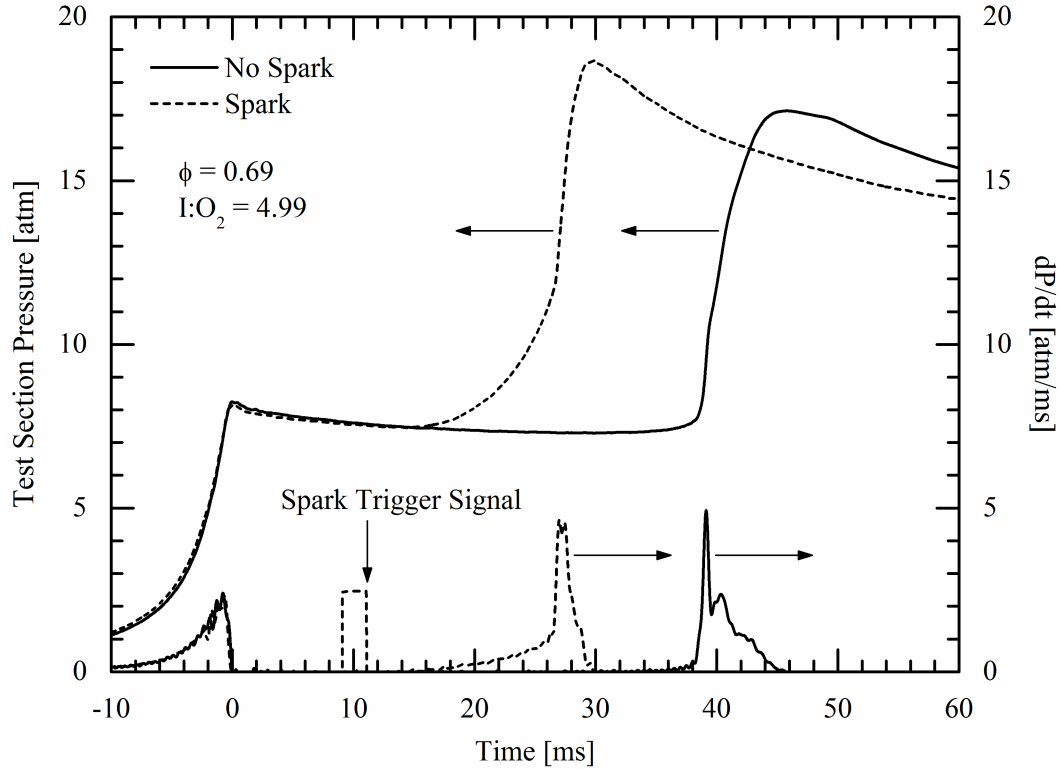
Figure 2.4: Comparison of the effects of spark ignition on the pressure and pressure derivative time histories for iso-octane/O_2 mixtures with the same mixture composition and virtually identical end of compression conditions (spark experiment: T_{EOC} = 942 K, and P_{EOC} = 8.1 atm, no-spark experiment: T_{EOC} = 945 K, P_{EOC} = 8.2 atm).

The effects of flame propagation on pressure time history and resulting autoignition delay time are directly compared in Figure 2.4 and Figure 2.5. Pressure and corresponding imaging data for a spark-initiated flame/autoignition experiment and a non-sparking autoignition experiment are presented in Figure 2.4 and Figure 2.5, respectively. The end of compression conditions for the two experiments are virtually identical (spark-initiated experiment: P_{EOC} = 8.1 atm, T_{EOC} = 942 K; autoignition experiment: P_{EOC} = 8.2 atm, T_{EOC} = 945 K). As seen in Figure 2.4, the two pressure time-histories remain within < 1.5% until approximately 5 ms after the spark has been discharged or about 16 ms after the end of compression. The effects of compression heating by flame propagation lead to higher effective conditions for the spark-initiated experiment of P_{eff} = 8.2 atm, and T_{eff} = 945 K, compared to the autoignition experiment conditions of P_{eff} = 7.5 atm, and T_{eff} = 926 K. Note that the non-sparking experiment shows effects of chemical exothermicity during the ignition delay time. However, comparison of the two pressure time histories immediately
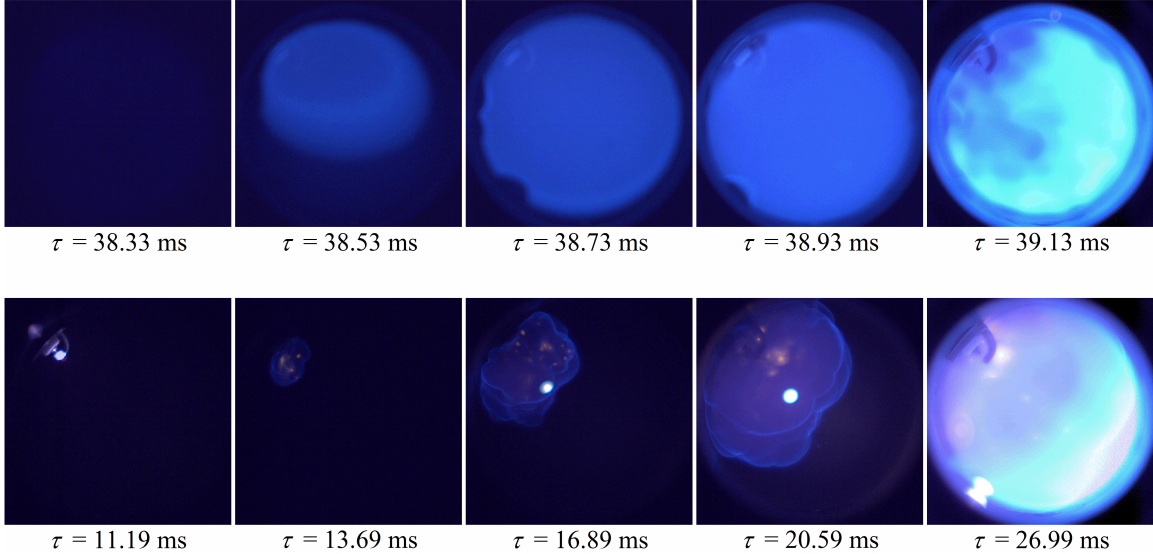
Figure 2.5: High-speed imaging data (selected frames) corresponding to the two ignition experiments presented in Figure 2.4. The upper panel presents frames from the non-sparking experiment and the lower panel presents frames from the sparking experiment. Time $\tau = 0$ corresponds to the end of compression for both image sequences.

prior to autoignition shows the contribution from compression heating to the increase in pressure is significantly higher than the contribution from chemical reaction for these particular experiments. The autoignition of the spark-initiated experiment is accelerated by 31% compared to the baseline autoignition delay time (spark-initiated experiment: $\tau_{ign} = 26.9$ ms; autoignition experiment: $\tau_{ign} = 39.0$ ms). The imaging data of Figure 2.5 show the uniform and rapid chemiluminescence associated with autoignition of the non-sparking autoignition experiments; note the compressed time scale of the images of the upper panel compared to the lower panel. For the upper panel, the peak illumination intensity corresponding to the autoignition event occurred between the fourth and fifth frames. The imaging data of the spark-initiated experiment show a complex and irregular flame surface is formed by the spark plasma, and the flame propagates outward from the spark plug electrode. Autoignition for the sparking experiments occurs in the volume of the unburned gases after the flame has propagated nearly halfway across the diameter of the test section

Non-sparking experiments were conducted to ensure the new test section reproduced previous UM RCF measurements of autoignition delay times for iso-octane. A summary of these baseline autoignition experiments is provided in the supplementary material in Table A.1 which includes the mixture composition, end of compression pressure and temperature, effective pressure and temperature, and autoignition de-

lay time data. The results of the current work for baseline autoignition delay times agree well with previous UM RCF iso-octane autoignition data from Walton et al. [6] as seen in Figure A.1 of the supplementary material. The cumulative experimental uncertainty of the autoignition delay time for the experiments in this study was ± 15%.

The experiments in this work considered a broad range of compositions with equivalence ratios of $\phi = 0.20$ to 0.99 and inert to oxygen dilution ratios of $I : O_2 = 3.76$ to 7.47 (mole basis); however, the pressures and temperatures intentionally spanned a narrow range to facilitate the determination of lean flammability limits and to minimize the effects of state conditions on flame propagation. Consequently, the end of compression pressures spanned $P_{EOC} = 8$ to 8.5 atm, and the end of compression temperatures spanned the range $T_{EOC} = 942 - 1000$ K. Table 2.1 provides a summary of the results of the experiments in which the spark discharge system was applied. The results include the mixture composition, state conditions, autoignition delay time data and information on whether a flame was successfully initiated for each experiment. The experiments in which flames were not successfully initiated are identified as below the flammability limit (BFL) in Table 2.1 and were used to identify the lean flammability limits for the mixtures.

In the current work, and with RCM studies in general, buffer gas composition was varied to control the end-of-compression temperature and pressure of the experiments. While the composition of the buffer gases can affect autoignition delay times in the negative-temperature-coefficient region via chemical interactions and through the heat capacity of the mixture [37], the chemical effects are expected to be negligible ($< 5\%$) at the conditions studied here, which are outside the NTC region. Additionally, the heat capacity of each reactant mixture was calculated using the mixture composition and the end of compression temperature. The average mixture heat capacity for all mixtures was 26.93 J/mol-K with a standard deviation of 1.37%. Consequently, thermal effects due to compression heating (and endothermic and exothermic chemical reactions) are expected to be comparable for all experiments.

For some experiments, the effects of spark timing were considered and compared with baseline experiments with identical end of compression conditions and mixture compositions, but where the spark system was not used. All these experiments were conducted at conditions above the flammability limit, and flames were successfully initiated and sustained in each of these sparking experiments. The pressure time histories for these data are provided in Figure A.2 of the supplementary material. Experiments where the spark was triggered in the second (Q2) and third (Q3) quartile

27

showed negligible impact on the autoignition delay time (within the experimental uncertainty). Significant effect on the autoignition delay time was only observed when the flame was initiated early (during the first quartile), e.g. the results presented in Figure 2.4; however, not all Q1 sparking experiments affected the autoignition delay time. Figure 2.6 presents the change in the measured autoignition delay time relative to each corresponding baseline non-sparking measurement for the four end-of-compression temperatures considered in these experiments. When a decrease in autoignition delay time was observed, the pressure time history also showed a pressure rise above the baseline prior to the rapid pressure rise of autoignition, as seen in Figure 2.4. As discussed earlier, this pressure rise is attributed to compression heating of the unburned mixture by the flame, and results in an increase in the effective or time-averaged temperature of the experiment. Therefore the change in T_{eff} relative to the baseline non-sparking experiment is also a metric of the impact of flame propagation on autoignition and is provided in Figure 2.6. The data show $\sim 2 - 31\%$ decrease in the ignition delay time due to flame propagation with corresponding changes in average temperatures of $\sim 1 - 19$ K. The magnitude of compression heating is a function of the test gas mixture composition, spark timing, state conditions, and volume of the test chamber. While the data in Figure 2.6 are presented as a function of T_{EOC}, the energy content of the mixture may be a more appropriate parameter, as is discussed further below.

2.4.2 Lean Flammability Limits

The lean flammability limits defined by the fuel-to-oxygen equivalence ratio were determined at three levels of dilution for nominal end of compression conditions of $P_{EOC} = 8.6 \pm 0.9$ atm and $T_{EOC} = 977 \pm 35$ K. For each dilution level, spark initiated experiments were conducted over a range of equivalence ratios from $phi = 0.20 - 0.99$. For each experiment, the spark was triggered and the imaging data were used to determine if a flame was successfully initiated and sustained. The effects of flame propagation were also observable in the pressure time history as a pressure rise prior to autoignition, as seen in Figure 2.3 and Figure 2.4. For experiments in which flames were not successfully initiated by the spark discharge, no additional pressure rise was observed in the pressure time histories prior to autoignition.

The results of the flammability limit study are presented in Figure 2.7 as a function of mixture dilution. Conditions in which flames were successfully initiated and sustained in the chamber are presented as circles, while conditions in which a flame was not successfully initiated or the flame quenched before autoignition are presented
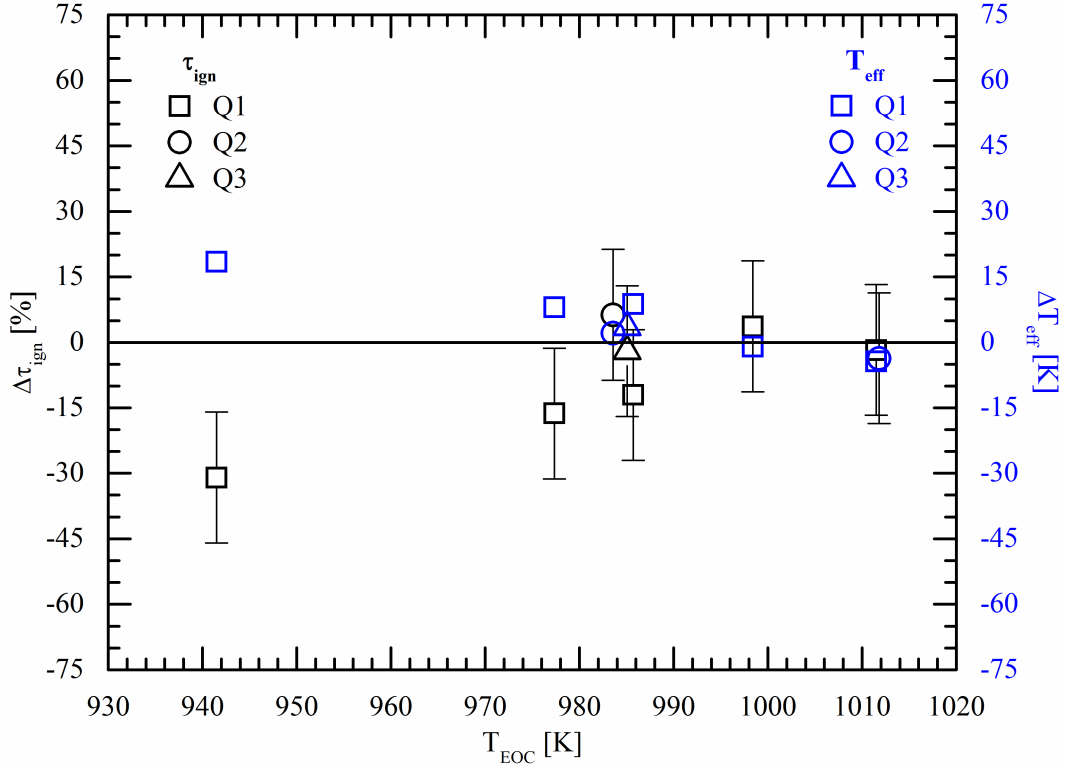
Figure 2.6: The effects of flame propagation on the measured ignition delay time and effective temperature relative to identical baseline autoignition experiments. The error bars represent the uncertainty in measurements of τ_{ign}.

as squares. The flammability limit is defined as the midpoint between the conditions in which flames were observed and conditions in which they were not. Multiple experiments were performed near the lean limit to ensure repeatability and using higher exposure settings of the camera, to maximize detection of the chemiluminescence from the flames. Furthermore, the image analysis code was applied to verify the classification of the experiments performed near the flammability limit, as the chemiluminescence could be relatively weak at those conditions. The results show the lean flammability limit for ϕ increased significantly, by 86%, from air levels of dilution ($I : O_2 = 3.76$) to the most dilute condition of $I : O_2 = 7.47$.

2.4.3 Imaging Results of Flame Propagation Rates

For experiments in which flames were successfully initiated by spark discharge and sustained, the imaging data were used to determine the propagation rate of the flames. Not all the imaging data could be analyzed to determine propagation rates, as some images had high uncertainty in the flame position due to overlapping flame fronts or
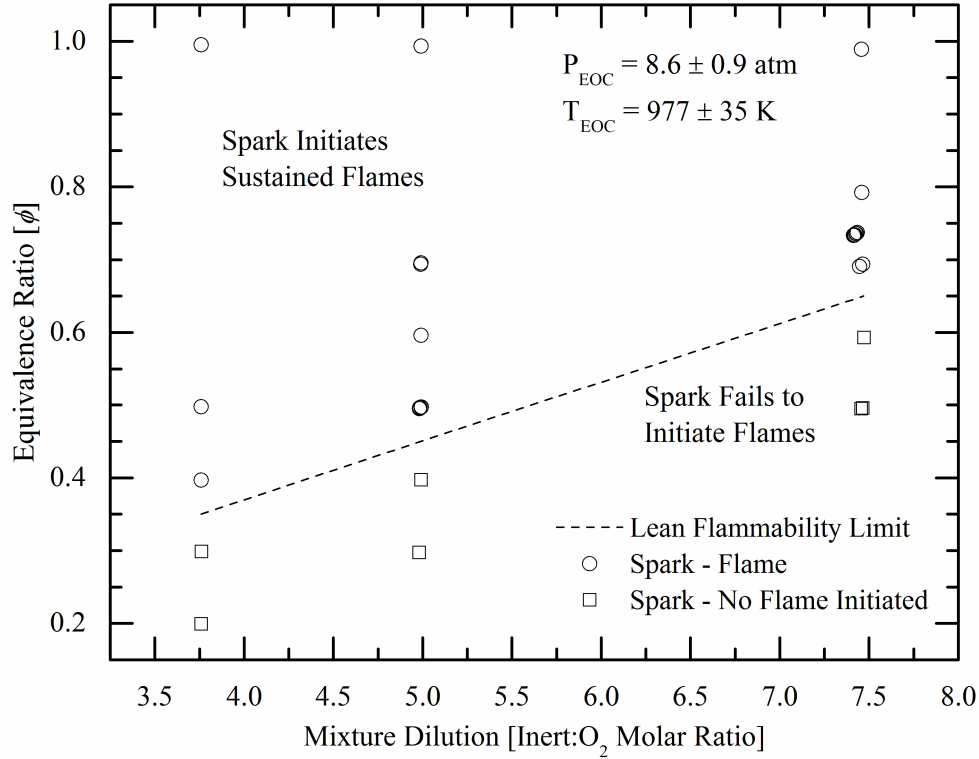
Figure 2.7: Summary of the experimental results for lean flammability limits as a function of dilution.

weak chemiluminescence. However, for imaging data where the flame front was well defined, the location of the flame front along selected trajectories was determined as a function of time relative to an origin that was set as the centroid of the spark discharge. The position of the flame front was determined along trajectories at 0.0° (horizontal), 26.6°, 45.0° (diagonal), 63.4°, and 90.0° (vertical) orientations as shown in the inset in Figure 2.8. For reference, the experimental results presented in Figure 2.8 are from the experimental results presented in Figure 2.3 ($\phi = 0.99$, inert to O_2 ratio = 4.99, $P_{EOC} = 8.4$ atm, $P_{eff} = 8.8$ atm, $T_{EOC} = 976$ K, and $T_{eff} = 985$ K). Results for the position of the flame along the measurement trajectories are presented in Figure 2.8, where time t = 0 is now defined as the first time the spark plasma was observed. The time histories of the flame positions were smoothed using a two-point moving average filter. At early times, the position of the flame front was convolved with the spark plasma. After the flame was successfully initiated, the position data show the flame grew at similar rates of expansion along the different measurement trajectories for these experimental conditions, i.e. the flame development was generally uniform. The rapid increase in the position of the reaction front at t ≈ 5.5 ms was the result

30

of volumetric autoignition.
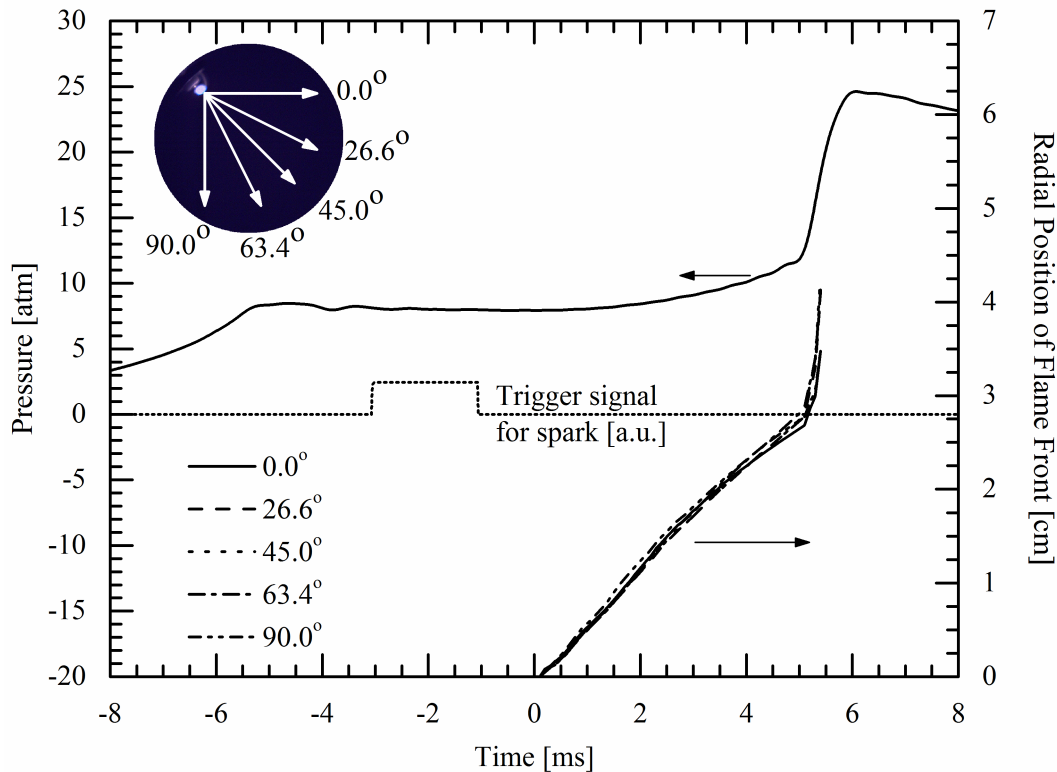
Figure 2.8: Time histories of the flame position as determined from the high-speed imaging data of the experimental results of Figure 2.3 ($\phi = 0.99$, inert to O_2 ratio = 4.99, $T_{EOC} = 976$ K, and $P_{EOC} = 8.4$ atm). The pressure time history and spark plug trigger signals are provided for reference. Time t = 0 ms corresponds to the first observation of the spark plasma. Measurements were made along five vectors with a common origin (set as the center of the spark plasma) as shown in the inset.

The propagation rates of the flame front(s) along the trajectories were determined by differentiating the smoothed flame position data with respect to time. The results based on the data of Figure 2.8 are presented in Figure 2.9. The average rate of propagation of the five trajectories is provided in Table 2.1 for each experiment where flame location was well identified. The propagation rate data were not corrected for stretch, density changes, or the effects of the proximity of and ignition energy of the spark discharge, and the results are not flame speed measurements. The propagation rate data describe the apparent or observed expansion rate of the flame surface. Laminar flame speed measurements cannot be accurately determined from these experiments for a variety of reasons. Flame stretch correction theory typically assumes spherical flames [38] and the flame surfaces observed in this study were irregular in many cases (see Figure 2.5). In addition, there was significant pressure rise during
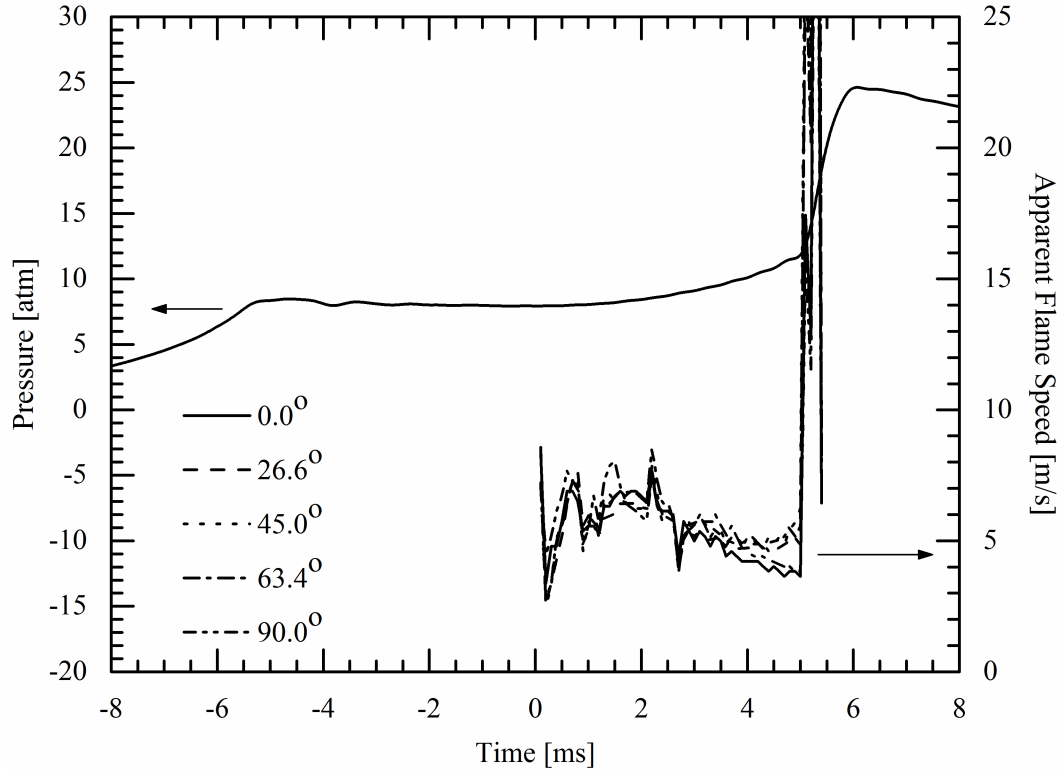
Figure 2.9: Results for apparent flame speed calculated using the derivative of the corresponding radial position data presented in Figure 2.8. Time t = 0.0 ms corresponds to the first observation of the spark plasma. The measurements are for the five trajectories presented in Figure 2.8.

the time of flame propagation in the current experiments, which was beyond even the most generous corrections for stretch in a confined vessel with weak pressure rise [39]. Down-selecting the data within each experiment to meet the weak pressure rise criterion does not allow for enough usable time history to determine meaningful flame speed data. As seen in Figure 2.9, the deceleration of the flame front as pressure in the test section increased was significant, with speeds decreasing by over 30% from the maximum rates of $\sim$ 6 m/s to less than 4 m/s immediately prior to autoignition for this experiment. The variability in the flame speed data at early times is due to convolution of the flame initiation with the spark plasma. A minimum flame radius of 6 mm is recommended for flame speed measurements in order to ignore the effects of the ignition source [40], which would lead to even greater down-selection of the data from these experiments. Further complicating the assignment of a laminar flame speed determination is that the flames were propagating into a mixture which was reacting, and consequently the unburned mixture composition was changing as a

32

function of time. For reference, calculated density ratios of the burned to unburned gases are provided in Table 2.1, but the propagation rates reported in the figures were not corrected for density.
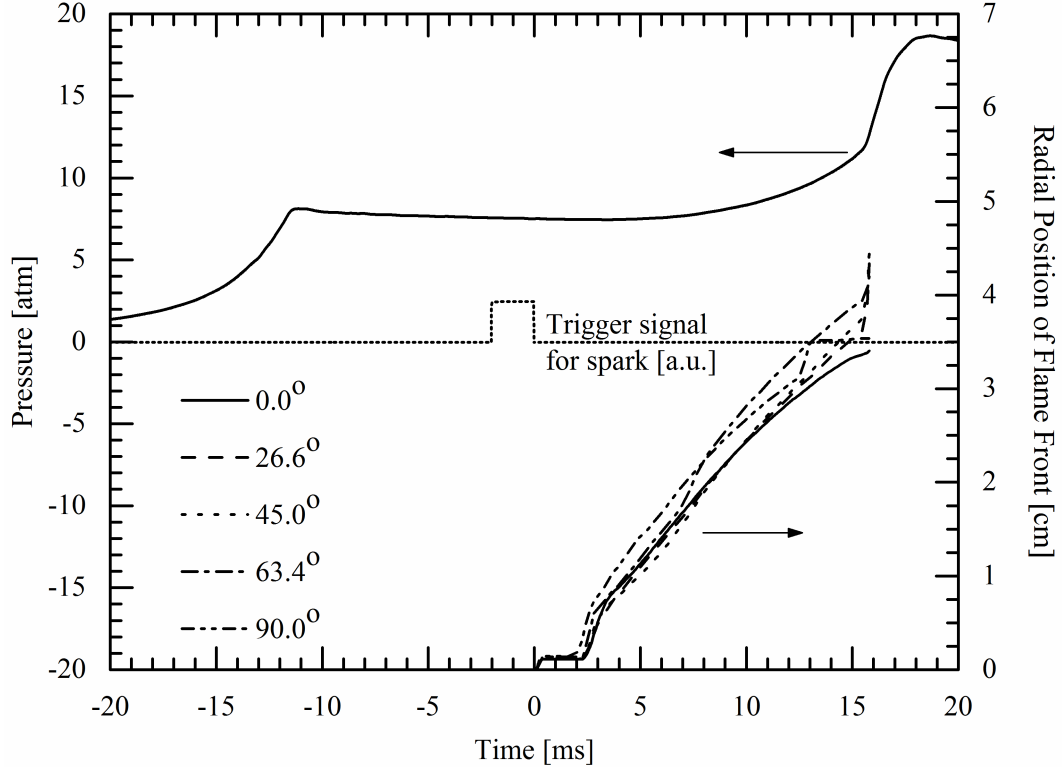
Figure 2.10: Time history of the flame position as determined from the high-speed imaging data of the experimental results of Figure 2.4 ($\phi = 0.7$, inert to O_2 ratio $= 4.99$, $T_{EOC} = 942$ K, and $P_{EOC} = 8.1$ atm). The corresponding pressure time history and spark trigger signal are shown for reference.

Figure 2.10 presents another set of flame position data corresponding to the spark-initiated experiment results presented in Figure 2.4 and Figure 2.5. For reference, the experimental conditions for the results presented in Figure 2.10 were $\phi = 0.70$, inert to O_2 ratio $= 4.99$, $P_{EOC} = 8.1$ atm, $P_{eff} = 8.2$ atm, $T_{EOC} = 942$ K, and $T_{eff} = 945$ K. As in Figure 2.8, t $= 0.0$ ms corresponds to the first observation of the spark plasma, and the origin for the measurements was the center of the spark plasma. Measurements were made along the five trajectories shown in Figure 2.8. Unlike in the data of Figure 2.8, the expansion of the flame fronts along the measurement trajectories in this experiment was not uniform spatially or temporally. As seen in the flame imaging (Figure 2.5), the flame surface created by the spark plasma in this experiment was more irregular in shape with multiple overlapping surfaces. As
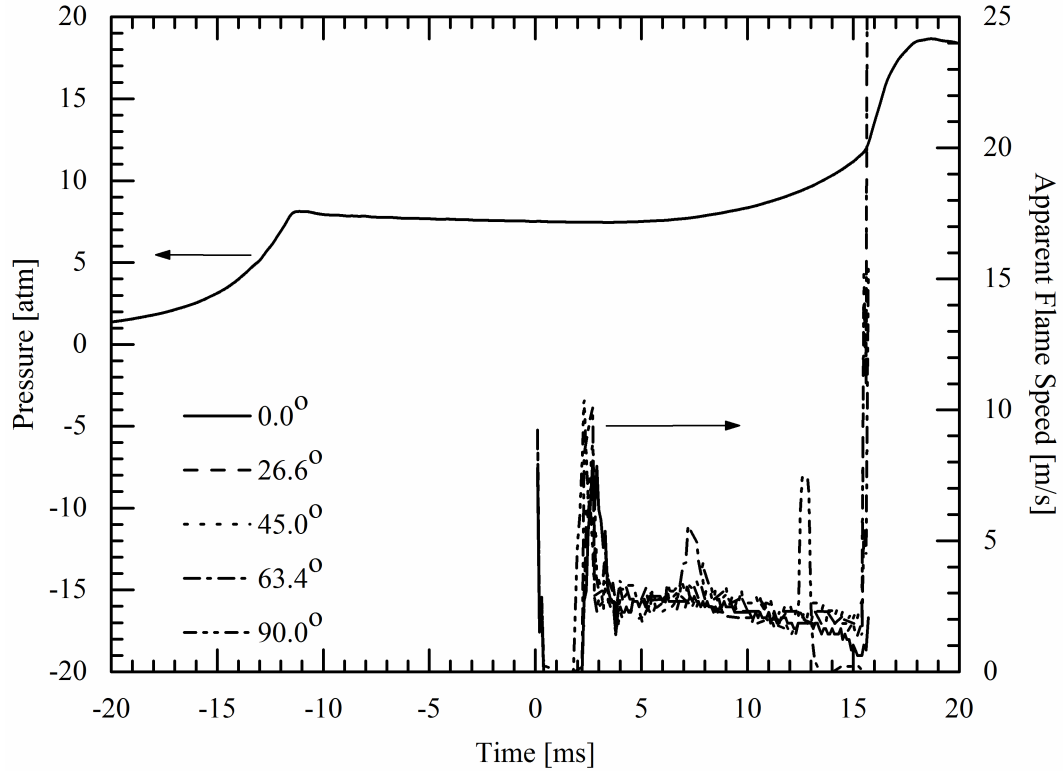
Figure 2.11: Results for apparent flame speed calculated using the derivative of the corresponding radial position data presented in Figure 2.10.

the flame surfaces interact and merge over time, abrupt changes in the flame surface along the measurement trajectories are recorded, as seen in Figure 2.10, and for this experiment, the flame development was not spatially or temporally uniform. The propagation rates derived from the flame position data of Figure 2.10 are presented in Figure 2.11. The apparent flame speeds were significantly slower ($\sim 2 - 3$ m/s) when compared to the equivalent dilution condition of Figure 2.9, in which propagation rates of $\sim 4 - 6$ m/s are observed. Deceleration of the flame surface as pressure increased in the test section is evident in the data, although not to the same extent as observed for the higher equivalence ratio example presented in Figure 2.9. The two experiments had similar effective pressures ($P_{eff} = 8.8$ and 8.2 atm) with slightly higher effective temperature for the data of Figure 2.9 ($T_{eff} = 985$ K) compared to Figure 2.11 ($T_{eff} = 945$ K). The lower propagation rates of Figure 2.11 are attributed to the slightly lower temperature and the lower equivalence ratio of $\phi = 0.7$ compared to $\phi = 0.99$.

Average propagation rates were determined for each of the experiments in which the spark plasma successfully initiated a flame. The results were evaluated to de-

termine if a correlation could be identified between the flame propagation rates and the ignition experimental conditions, including the reactant composition. The propagation rates were expected to be a function of the end of compression temperature and pressure, equivalence ratio, and dilution based on laminar flame theory. The cumulative effects of these parameters were determined by calculating the theoretical adiabatic flame temperature for each experimental condition using the thermochemistry for iso-octane and other reactants from the iso-octane mechanism (version 3) of Mehl et al. [41]. The initial reactant composition, temperature, and pressure were specified from each experimental condition. The computed results included the effects of dissociation on the adiabatic flame temperature. The results for the average flame propagation rates and the individual rates along each measurement vector are presented in Figure 2.12 as a function of the theoretical adiabatic flame temperature. Also included in the data are the conditions in which the spark plasma did not successfully initiate a flame.
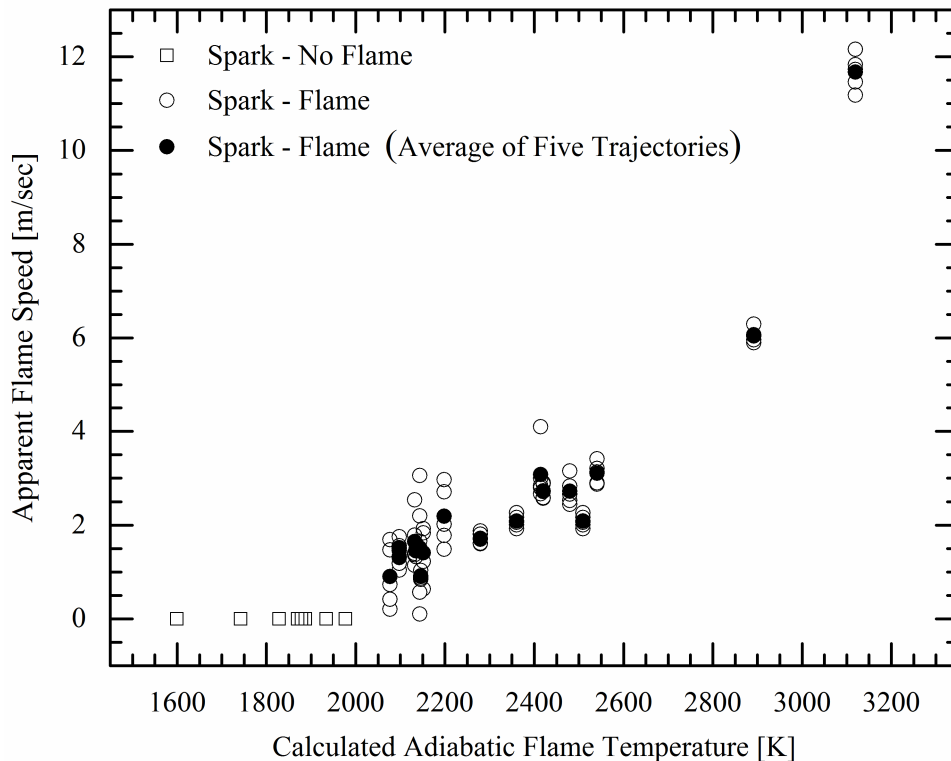
Figure 2.12: Experimental measurements of the average flame propagation rates as a function of the theoretical adiabatic flame temperature. The open symbols are the average propagation rates along each of the measurement vectors shown in the inset of Figure 2.8. The solid symbols are the overall averages for each experiment.

The data show a strong correlation between the observed propagation rates and the energy content of the mixture as represented by the adiabatic flame temperature. Conditions with low energy content could not sustain flames and increasing the mixture strength, increased the propagation rate of the flames. Based on these results, the effects of flame propagation on autoignition can be anticipated to be more significant for mixtures with higher energy content, and the data of Figure 2.12 support that there may be an energy threshold, e.g. $T_{ad} > 2000$ K, for the conditions studied here. It would be valuable to develop a quantitative and predictive measure of the impact of flame propagation on autoignition delay time. The data presented in the current work provide a valuable basis for developing such metrics; however, a larger range of pressures and temperatures must be considered for a more complete understanding of the range of effects that can be observed during flame/autoignition interactions.

2.5 Conclusions

The current work presents new data on the initiation and propagation of flames into premixed fuel/air mixtures at well-defined initial state conditions. The results of the study showed the effects of flame propagation were maximized when the flame was initiated early during the autoignition delay period (e.g. during the first quartile). Later ignition timing (e.g. during the second or third quartile of the autoignition delay period) reduced the impact of flame propagation even when flames were successfully initiated and sustained. When the effects of flame propagation were apparent on autoignition delay time, the impact was to accelerate ignition by approximately $2-31\%$. Image analysis allowed apparent propagation rates of the flames to be determined. The high-speed imaging data also allowed flammability limits to be identified at conditions directly relevant to advanced engine strategies. Dilution had significant effect on the lean flammability limits, increasing from a lean limit of $\phi = 0.35$ at air levels of dilution to $\phi = 0.65$ at inert:O_2 dilution of 7.5. The flammability limit was also well correlated with the theoretical adiabatic flame temperature. These results provide unique, vital, and quantitative new information for development and validation of theory and models of flame/autoignition interaction, as well as providing fundamental understanding of the physical and chemical interactions important to multi-mode combustion strategies like spark-assisted compression ignition. While the data encompass a relatively narrow range of pressures and temperatures, the results provide several quantitative benchmarks of the impact of flame propagation on auto-ignition

at well-controlled mixture and initial state conditions. Consequently, the data can be the basis for model validation as well as the development of broader fundamental combustion criteria to quantify the conditions where spark initiated flame propagation can impact auto-ignition both adversely (e.g. as in the case of end knock) and productively (e.g. SACI).

2.6 Acknowledgements

CHAPTER III

Computational Development of a Dual Pre-Chamber Internal Combustion Engine Concept

This chapter was published as Assanis, D., Engineer, N., Neuman, P., and Wooldridge, M., "Computational Development of a Dual Pre-Chamber Engine Concept for Lean Burn Combustion," SAE Technical Paper 2016-01-2242, 2016, doi:10.4271/2016-01-2242. [42]

3.1 Abstract

Pre-chambers are a means to enable lean burn combustion strategies which can increase the thermal efficiency of gasoline spark ignition internal combustion engines. A new engine concept is evaluated in this work using computational simulations of non-reacting flow. The objective of the computational study was to evaluate the feasibility of several engine design configurations combined with fuel injection strategies to create local fuel/air mixtures in the pre-chambers above the ignition and flammability limits, while maintaining lean conditions in the main combustion chamber. The current work used computational fluid dynamics to develop a novel combustion chamber geometry where the flow was evaluated through a series of six design iterations to create ignitable mixtures (based on fuel-to-air equivalence ratio, ϕ) using fuel injection profiles and flow control via the piston, cylinder head, and pre-chamber geometry. The desirable and undesirable features that guided the design progression are presented. Major combustion chamber design iterations involved changes to the pre-chambers position relative to the cylinder head deck plane, azimuthal orientation of the pre-chambers, and piston crown geometry. Further criteria were developed to assess the

flow interaction with the nozzle connections to the pre-chambers. The modeling results indicated appropriate fueling strategies achieved near stoichiometric fuel-to-air equivalence ratios in the pre-chambers with lean fuel-to-air equivalence ratios in the main chamber. The results also demonstrated the utility of the flow-alignment and chamber filling criteria to select the nozzle design for the pre-chambers.

The dramatic advances in digital computing has radically changed the process of engine research and development; significantly reducing the time from concept to reality. In this thesis, fundamental experiments, computational studies and experimental validation techniques have successfully guided the development of new engine hardware targeted to enable fuel lean, high-efficiency reciprocating engines. The following are the key conclusions and outcomes of this thesis.

3.2   Introduction

Lean burn combustion strategies are an attractive option to increase the thermal efficiency of gasoline spark ignition internal combustion engines, but engine design remains challenging due to the lean flammability limits of the fuel/air mixture. Lean after-treatment strategies can be a concern; however, recent advances show considerable promise for effective emissions control for lean burn gasoline direct injection engines [43]. Turbulent jet ignition originating from a combustion pre-chamber can help address mixture flammability limits by ejecting high enthalpy and highly reactive jets into the main chamber, enabling lean combustion in the main chamber. However, appropriate mixture conditions must be achieved in the pre-chamber for this strategy to be successful.

Pre-chambers have been studied extensively in the past, in particular for application in compression ignition engines, and pre-chambers have been successfully demonstrated as technology which can improve in-cylinder combustion robustness [44–46]. Past learnings of pre-chamber technologies, including studies of the effects of heat transfer and mixture stratification, have guided the size, shape, orientation, and number of pre-chambers [47, 48]. The engine concept proposed in this work is based on a new pre-chamber engine design where the spark electrodes are located in the pre-chamber and a direct injection (DI) fuel injector is located in the main chamber. Supplemental fueling (e.g. DI or port fuel injection (PFI)) is used to create the initial fuel/air charge in the main combustion chamber. To the best of our knowledge, this approach differs from any pre-chamber engine designs previously considered. The design was enabled by advances in numerical simulations, computational resources, fuel

injection hardware, and manufacturing techniques. Specifically, the objective of the design process documented here was to develop a combustion system where lean fuel-to-air equivalence ratios are created in the main chamber while near stoichiometric equivalence ratios are created in the pre-chambers using the DI fuel injector.

3.3 Background

With the passing of the Clean Air Act of 1970 and the subsequent establishment of the Environmental Protection Agency, engine technologies offering significantly reduced tailpipe emissions started gaining major attention. Notably, gasoline pre-chamber engine concepts offered a promising solution to decreasing mobile sources of air pollution by increasing fuel efficiency and by decreasing engine-out emissions [49]. Pre-chamber engine concepts are not a new technology to the automotive industry. H.R. Ricardo's internal combustion engine, documented in 1918, is the earliest pre-chamber concept found in the literature [13]. The pollution regulations of the 1970's brought renewed focus on the pre-chamber engine concept from research institutions and industry [16–22]. Most of the pre-chamber engine concepts suffered from atypical induction designs that required complicated valvetrain arrangements [16]; however, recent advances in numerical simulations and computational resources allowed gasoline pre-chamber engine concepts to be systematically considered in new configurations. The comprehensive review by Toulson et al. [48] outlined the progress of pre-chamber initiated combustion systems throughout history and provided sound engineering and scientific foundations for new engine designs which leveraged the best features of pre-chambers. Attard et al. [50] demonstrated an auxiliary-fueled turbulent jet ignition pre-chamber concept in a GM Ecotec engine platform capable of achieving 42% peak net indicated thermal efficiency without the need for a complicated valvetrain induction system. In comparison, the standard GM Ecotec engine platform achieved a peak net indicated thermal efficiency of 37.9% in stoichiometric spark ignition mode of operation.

The work presented in this paper focused on designing a prototype pre-chamber engine that reduces system complexity by eliminating the need for an auxiliary fuel injector located in the pre-chamber. Instead, the pre-chambers were designed to be fueled using an injection event from a fuel injector centrally mounted in the main combustion chamber (i.e. a gasoline DI system). This design concept leverages the advanced capabilities of modern fuel injectors and targets overall fuel lean operation. The technical approach used CFD to evaluate non-reacting in-cylinder flows of fuel

and air achieved through different engine geometries. The designs were evaluated using metrics defined in the study to assess the efficacy of the flow at achieving the desired equivalence ratios in the pre-chambers and the main chamber.

3.4   Computational Methodology

The commercial software CONVERGE™(versions 2.1.0 – 2.2.0) was used for the CFD study. The software platform was selected based on the adaptive mesh refinement capabilities. Matlab R2014a-R2014b was used to post-process the output files and derive flow metrics. Ensight 10.1 was used to visualize the output data. Relevant boundary conditions and initial conditions were derived from a validated GT-Power (v7.4) engine model for all cases.

The flow field in the three-dimensional, moving boundary domain was modelled as compressible, viscous and non-reactive and used a k-ε turbulence model and temperature law-of-the-wall boundary conditions. The pressure solver first used a point-wise successive over-relaxation algorithm before using an efficient geometric multigrid procedure. A finite volume numerical discretization scheme was used to solve momentum, energy and species equations. Pressure-velocity coupling was accomplished using the pressure-implicit-with-splitting-of-operators method in conjunction with the Rhie-Chow interpolation scheme.

Iso-octane, i-C_8H_{18}, was used as the fuel and air was 23% oxygen (mass basis) and 77% nitrogen for all simulations. Dilution of the fuel/air charge with exhaust gas residual species was not considered in these studies. The spray rate profile was modeled as a square step function with a targeted peak injection pressure of 149 ± 1 bar. The duration of the fuel injection event was varied to achieve the total mass of fuel desired. The fuel injector was represented as two identical nozzles 180° opposed in the azimuthal direction, each with a nozzle diameter of 150 μm, circular injection radius of 75 μm, and nozzle radial position of 1.5 mm.

The liquid fuel spray, injected at 335 K, was modeled using 50,000 parcels per injector based on a sensitivity study and best practices recommendations from the software manufacturer. The parcels were modeled as a bulk injection with the fuel droplet size distribution based on the nozzle size, and the parcels were distributed evenly throughout the spray cone [51]. Kelvin-Helmholtz (KH) and Rayleigh-Taylor (RT) models were used to represent the primary spray breakup. The secondary spray breakup was modeled using child parcels and by examining the competing effects of the KH and RT breakup models [52]. The specific model parameters used for the

simulations are provided in the supplementary material found in Appendix B and were based on the recommendations by CONVERGE for engine simulations of the type considered here. Further detail on the modeling parameters and theory can be found to in Senecal et al. [53] and Richards et al. [52].

The initial engine geometry for the new engine concept was based on a conventional inline four cylinder 2.0 L forced-induction gasoline production engine. The geometry of a single cylinder of the base engine is presented in Figure 3.1.
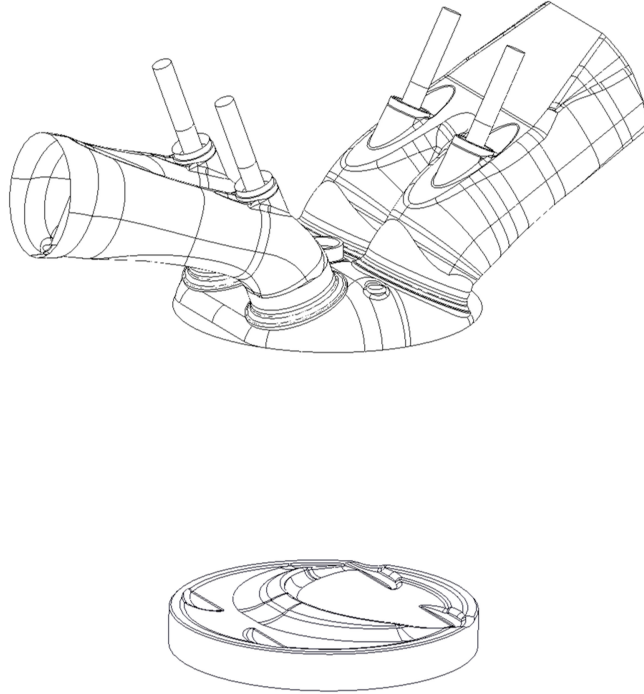
Figure 3.1: Production base geometry (bottom dead center position) used as the starting point for the engine design process.

The production engine featured a four-valve design, centrally-mounted spark plug, side-mounted direct injector, and a piston crown designed to enhance mixing. The geometric specifications of the base engine and the final engine design (designated the Zeta prototype) are presented in Table 3.1.

A total of seven regions (defined by virtual boundaries in the simulation) were defined to develop flow metrics to evaluate the performance of the different engine designs. The boundaries, regions, associated initial conditions, and event timings are all provided in the supplementary material in Table B.1, Table B.2, and Table B.3. All calculations used initialization values for turbulent kinetic energy (TKE) of 1.0 m^2/s^2 and for TKE dissipation rate of 10 m^2/s^3. The computational mesh was a modified cut-cell Cartesian grid [52]. The base cell size for the entire engine geometry mesh

Table 3.1: Summary of the specifications of the initial and final engine designs. Specification Base Engine Zeta Prototype

Specification	Base Engine	Zeta Prototype
Bore	86.0 mm	86.0 mm
Stoke	86.0 mm	86.0 mm
Connecting Rod Length	149.25 mm	146.25 mm
Wrist Pin Offset	0.8 mm	0.8 mm
Compression Ratio	9.5	10.25
Intake Valve Diameter	32.7 mm	35.0 mm
Intake Valve Opening[a]		316 CAD
Intake Valve Closing[a]		582 CAD
Exhaust Valve Diameter	26.0 mm	29.0 mm
Exhaust Valve Opening[a]		164 CAD
Exhaust Valve Closing[a]		403 CAD

[a] Valve events are specified at 1 mm lift.

was set as a 4 mm cubic cell. Both fixed embedding and adaptive mesh refinement were utilized to locally refine the base mesh and create efficient and accurate grids at each time step. Portions of the main combustion chamber and the pre-chambers were further refined between 1 and 0.5 mm cubic cells. The volume defined by the projected bore area extended 17 mm past the cylinder head deck plane into the cylinder head and was populated with 1 mm cubic cells to ensure a smooth continuation of the flow from the port to the main combustion chamber. The remaining volume defined by the projected bore area into the cylinder head was populated with 2 mm cubic cells to help transition the flow from the base 4 mm cubic mesh found in the ports. Two layers of 0.5 mm cubic cells were embedded off the intake and exhaust valve angle boundaries to ensure the flow past the valves was accurately captured during the valve opening and closing events. The volume surrounding and including the fuel spray was refined to 0.5 mm cubic cells to ensure the spray region was sufficiently resolved. Figure 3.2 features a representative mesh of the final Zeta prototype just before an injection event is about to occur at 60° bTDC.

Velocity-based adaptive mesh refinement was used for the cylinder and intake system regions. A maximum allowable cell count of 1,000,000 cells could be achieved due to the adaptive mesh refinement. When the sub-grid velocity field exceeded 1.0 m/s, the affected cells and immediate neighbors were refined by reducing the cell size to 0.5 mm during the next time step. The total maximum cell count for the simulation results presented here was less than 990,000 cells, and the maximum cell count during the injection event was less than 725,000 cells. The cell counts were sufficient to
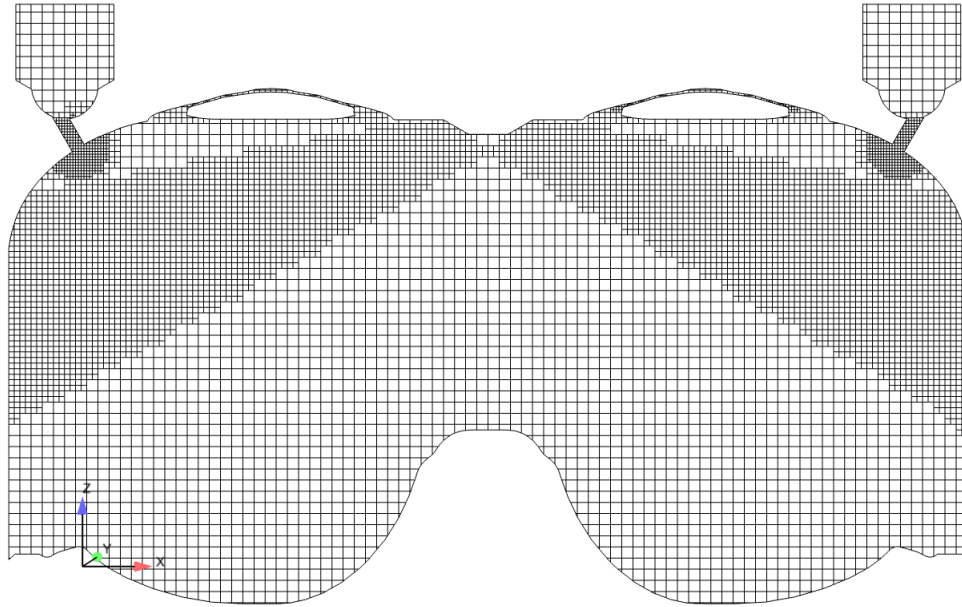
Figure 3.2: Example mesh highlighting the fixed cell embedding at the piston centerline for the final Zeta prototype just before the booster injection occurs at 60° bTDC.

obtain the desired sub-grid velocity field criterion of less than 1.0 m/s. The grid and refinement techniques are based on best practices recommendations [52,53] to ensure a sufficiently resolved grid for gasoline, direct-injection, non-reacting simulations.

3.5   Prototype Development

The objective of the computational study was to identify an engine design which could create local fuel/air mixtures in the pre-chambers above the ignition and flammability limits (i.e. with fuel-to-air equivalence ratios at near stoichiometric values, ϕ ~ 1.0), while maintaining lean conditions in the main combustion chamber. Rapid compression facility studies by Assanis et al. serve as a guidance for the flammability limits of lean and dilute iso-octane air mixtures in a combustion chamber [1]. While spark plugs will be used to ignite the mixtures in the pre-chambers, spark plugs were not included in the simulations and all flow was non-reacting.

A series of six prototype iterations, visual representations provided in Figure 3.3, were considered to meet the project targets for fueling. The designs varied the in-cylinder flow, the placement of the pre-chambers, and the fueling strategy to meet

the target equivalence ratios for the pre-chamber and the main combustion chamber. The naming convention was based on the generation of the design, e.g. Alpha, Beta, etc. ending with Zeta. A summary of the major design features for each iteration is presented in Table 3.2 and Table 3.3.

Alpha Prototype	Beta Prototype	Gamma Prototype

Pre-chambers

Pre-chambers

Pre-chambers

Delta Prototype	Epsilon Prototype	Zeta Prototype
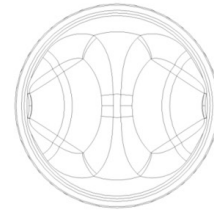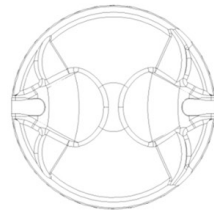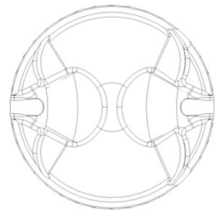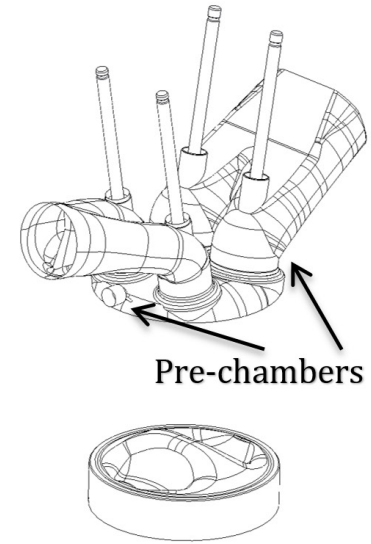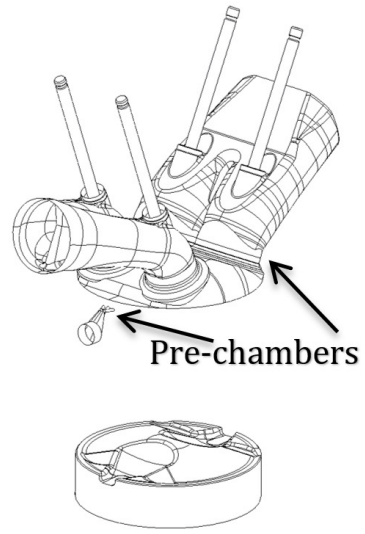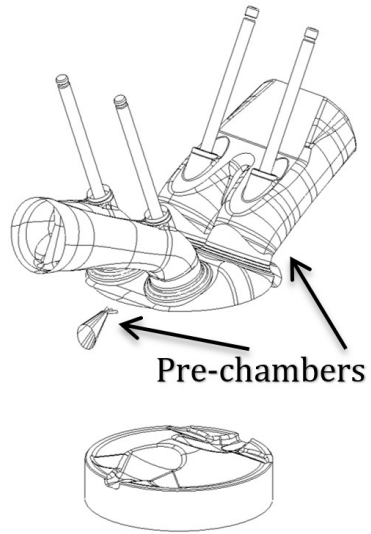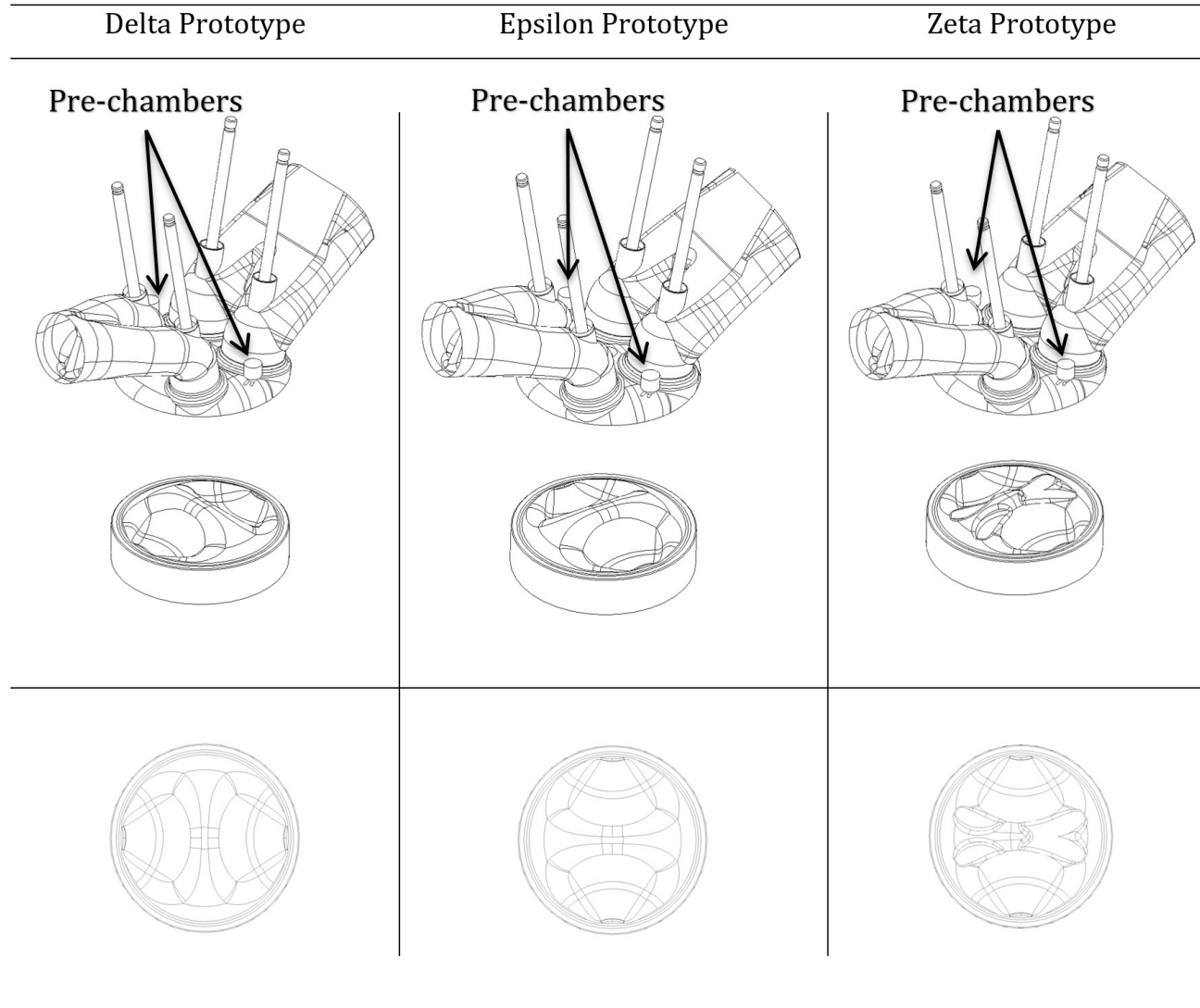
Figure 3.3: Visual representations of the Alpha through Zeta prototype iterations (bottom dead center position) in each upper panel with top-view of the associated piston crown in each lower panel. The arrows indicate the locations of the pre-chambers.

Table 3.2: Overview of key design features of the Alpha through Gamma prototype iterations and conclusions of initial computational simulations based on a 1 mg booster fuel injection event.

Prototype	Key Design / Revision Features	Conclusions
Alpha	• Orifices located in liner parallel to cylinder head deck. • Fuel spray was wall guided by the piston.	• Low pre-chamber equivalence ratio ($\phi \sim 0.15$) • Poor pre-chamber fuel vapor fraction ($\sim 45\%$ of the fuel mass in each pre-chamber) • Substantial main chamber wall film (70% of the total fuel mass) • Slight pre-chamber wall film (<5% of the total fuel mass)
Beta	• Central orifices widened and angled upwards to align with injector spray cone centerline. • Cut-out reliefs introduced in cylinder head dome to reduce wall wetting due to spray impingement.	• Higher pre-chamber equivalence ratio ($\phi \sim 0.6$) • Poor pre-chamber vapor fraction ($\sim 45\%$ of the fuel mass in each pre-chamber) • Minimal main chamber wall film (<0.5% of the total fuel mass) • Increased pre-chamber wall film ($\sim 23\%$ of the fuel mass in each pre-chamber)
Gamma	• Pre-chambers relocated to the cylinder head under ports. • Combustion chamber dome re-designed. • Intake port re-designed for enhanced tumble. • Fuel spray now air guided by charge motion.	• Low pre-chamber equivalence ratio ($\phi \sim 0.1 - 0.2$) • Excellent pre-chamber vapor fraction (100% of the fuel mass in each pre-chamber) • Slight main chamber wall film (<2% of the total fuel mass) • Pre-chamber wall film eliminated

Table 3.3: Overview of key design features of the Delta through Zeta prototype iterations and conclusions of initial computational simulations based on a 1 mg booster fuel injection event.

Prototype	Key Design / Revision Features	Conclusions
Delta	• Pre-chambers rotated 90° azimuthally about central Z-axis.	• Moderate pre-chamber equivalence ratio ($\phi \sim 0.3$) • Excellent pre-chamber vapor fraction (100% of the fuel mass in each pre-chamber) • High main chamber wall film (<10% of the total fuel mass) • Pre-chamber wall film eliminated
Epsilon	• Piston rotated 90° azimuthally about central Z-axis.	• Moderate pre-chamber equivalence ratio ($\phi \sim 0.3$) • Excellent pre-chamber vapor fraction (100% of the fuel mass in each pre-chamber) • High main chamber wall film (<8% of the total fuel mass) • Pre-chamber wall film eliminated
Zeta	• New piston geometry with valve cut-outs for improved range of valvetrain phasing	• Moderate pre-chamber equivalence ratio ($\phi \sim 0.3$) • Excellent pre-chamber vapor fraction (100% of the fuel mass in each pre-chamber) • Main chamber wall film eliminated • Pre-chamber wall film eliminated

The pre-chambers were designed to be indirectly fueled by a single injector located in the main combustion chamber. One end of each pre-chamber included the orifices to connect the pre-chamber to the main chamber. The number, size and orientation of the connecting orifices affect the pre-chamber filling process and were considered variable design parameters in this study. In an effort to simplify the pre-chamber design, no poppet valve assembly or auxiliary fuel injectors (features previously demonstrated in the literature, see [17] and references therein) were located in the pre-chamber volume. Although spark plugs were not included in the simulation, packaging constraints of the pre-chambers were imposed to allow the pre-chamber spark plugs to be accessible for installation and maintenance. The pre-chambers were also located so they would not interfere with neighboring cylinders. Ease of manufacturing was also considered with the pre-chamber design.

The geometries of the piston crown, combustion chamber dome, and the intake port were designed to create favorable charge motion so a combustible mixture could be inducted into the pre-chambers by the time the piston reached the top dead center (TDC) position. The surface area to volume ratio of the pre-chamber geometry was selected to decrease heat transfer losses. The production base engine geometry featured a centrally mounted spark-plug and a side-mounted injector. As noted earlier, the dual pre-chamber engine concept features a centrally mounted fuel injector in the main chamber with two opposed spray plumes targeted towards the pre-chambers. The central location of the fuel injector allowed for greater flexibility in creating a symmetric fuel spray pattern target flow to each of the pre-chambers.

The fueling amount used in the simulations was based on a typical engine operating condition of 2,000 RPM and 4 bar brake mean effective pressure (BMEP). This engine operating point required approximately 16 mg of fuel for typical SI operation. Since the dual pre-chamber engine concept targeted lean burn operation, the simulations considered 2 mg of fuel injected directly into the main combustion chamber by the direct injector. This fueling event is referred to as the booster injection, and is meant to create ignitable mixtures in the dual pre-chambers.

In addition to the booster fuel injection event targeted for fueling the pre-chambers, a global injection event would be required in the engine to create the overall fuel lean charge in the main combustion chamber. This global injection event could be provided by the DI or a PFI injector. The global injection event would occur before the booster DI event, providing a background or baseline level of fuel in the main chamber. The booster injection would occur after the global injection event, late in the intake stroke, and would introduce a small amount of fuel targeted to create the

near stoichiometric conditions in the pre-chambers. For this study, the global injection event was not included in the simulations, as it was assumed the global injection event would create a consistent background level of fuel in the main chamber and pre-chambers. This represents the most challenging situation for the booster injection, when there is no pre-existing background level of fuel in the main chamber or pre-chambers.

3.6 Results and Discussions

3.6.1 Prototype Performance

The major conclusions from the computational studies of the design prototypes are presented along with the major design features in Table 3.2 and Table 3.3. A key metric of prototype performance was the state of the fuel in the main chamber and pre-chambers. A summary of the fuel state from a booster injection event of 1 mg of fuel is presented by prototype iteration in Figure 3.4. The physical changes outlined in Table 3.2 and Table 3.3 were made to achieve fully vaporized fuel in the pre-chambers; a design feature which was met by the Zeta prototype.

Brief summaries of the design features of the prototypes are provided here. The Alpha prototype modified the production base geometry while attempting to integrate the pre-chambers as per the criteria described earlier. The intake port, exhaust port, and combustion chamber dome were unchanged. The two, diametrically opposed, pre-chambers were placed in the liner below the intake and exhaust ports. The pre-chambers were placed sufficiently below the cylinder head deck so the limiting dimension of the spark plug could clear the cylinder head gasket. Each conically shaped pre-chamber was sized as 1% of the total combustion chamber volume and included three horizontal connecting orifices, each with a nominal diameter of 1.25 mm. The pre-chamber volume sizing and orifice diameters were in alignment with recommendations set forth by Gussak et al. [15]. The Alpha prototype piston featured two scallops pointing towards each pre-chamber. When the piston was in the TDC position, the pre-chamber connecting orifices remained unobstructed. The Alpha prototype aimed to induct the charge mixture into the pre-chamber by transferring the charge mixture from the squish region through the connecting orifices to the pre-chamber.

For the Alpha prototype fueling strategy, two pencil sprays (i.e., with narrow spray cones), limited by the combustion chamber dome clearance, were aimed at a 125.5° included spray angle facing the narrow end of each scallop. One mg of fuel was
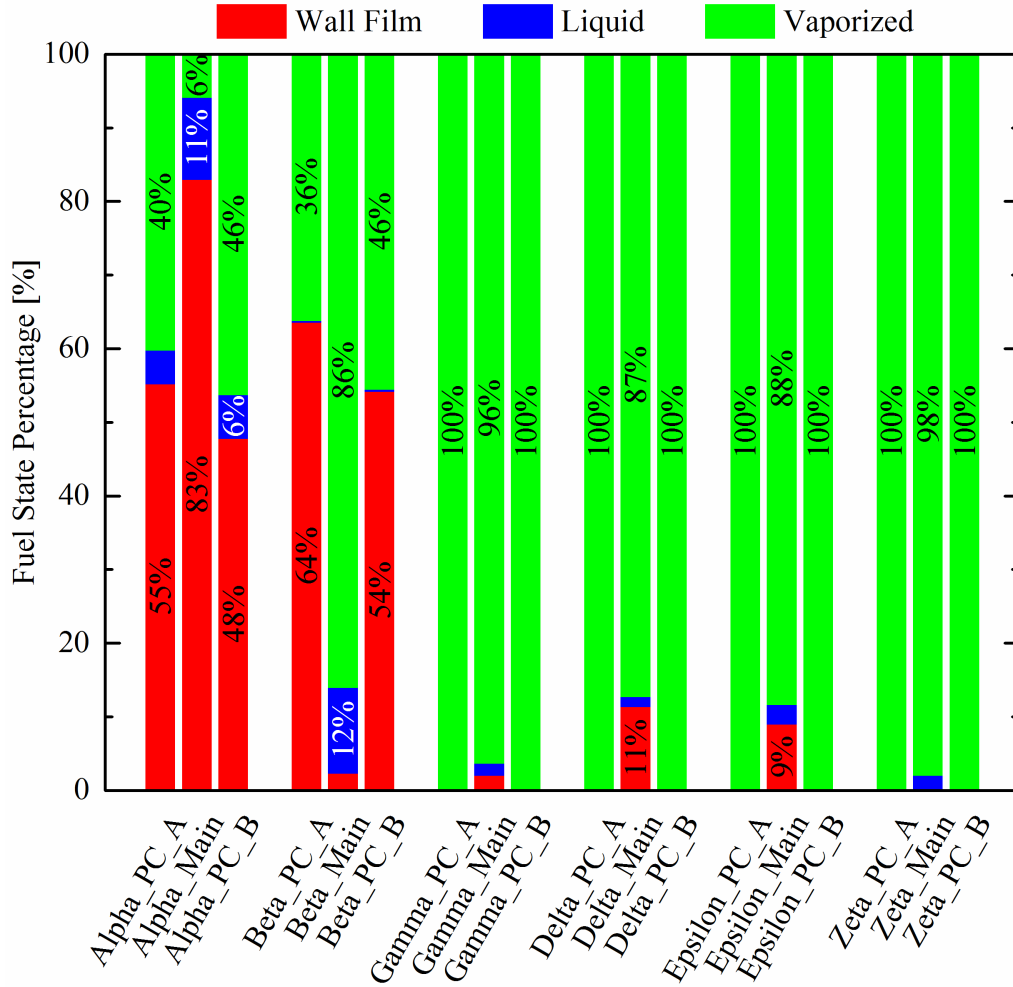
Figure 3.4: Summary of the fuel state (wall film, liquid, or vaporized) in the main chamber and pre-chambers by prototype iteration.

injected at 149.5 bar rail pressure for a duration of 3.54 CAD. Spray patterns with included cone angles of 2.6° and 5° were simulated at the start of the injection (SOI) timings of 35° bTDC, 20° bTDC, and 5° bTDC. The most successful spray pattern, 5° cone angle and 20° bTDC SOI, resulted in only 6.6% of the total fuel vaporized in the two pre-chambers at TDC. In summary, the Alpha prototype with a 1 mg fuel injection was able to achieve $\phi = 0.15$ and $\phi = 0.13$ in pre-chamber A and B, respectively. The vaporized fuel fraction was 41% and 46% in pre-chambers A and B, respectively, with the remainder of the fuel fraction in the liquid phase in each pre-chamber.

Using the most successful Alpha prototype spray profile, the mass of fuel injected was increased to 10 mg while keeping all other variables constant. The amount of vaporized fuel in the pre-chambers at TDC was approximately the same as for the

1 mg fuel injection at 6.2%. When the speed of the engine was doubled to 4000 RPM while setting the fueling amount at 1 mg, the amount of vaporized fuel in the pre-chambers at TDC decreased slightly to 6.0%.

The Beta prototype improved on the Alpha prototype by angling the central connecting orifice upwards to better match the fuel spray angle. The included spray angle for the two fuel jets was increased to 142.5° to directly target the central connecting orifice. The fueling amount was increased to 2 mg at the same rail pressure. Spray patterns with included cone angles of 2.6° and 5° were simulated at SOI timings of 60° bTDC, 40° bTDC, and 20° bTDC. The most successful spray pattern using 2 mg of fuel, a 5° cone angle and a 40° bTDC SOI, yielded ~50% of the total fuel as vapor in the two pre-chambers at TDC.

The Beta prototype with a 2 mg injection was able to achieve $\phi = 1.18$ (with a vaporized fuel fraction of 50%) and $\phi = 1.24$ (with a vaporized fuel fraction of 51%) in pre-chamber A and B, respectively. While the pre-chambers inducted enough fuel to achieve the design target of nearly stoichiometric mixtures, there was significant concern about the amount of liquid fuel present at TDC in each pre-chamber. 36.3% of the total fuel was predicted to result in wall films in the pre-chambers, occurring mostly in the connecting central orifice. The Beta design also raised concerns that the central orifice could clog during engine operation from fuel film effects such as coking or varnishing. The high levels of wall films could also be a source of unburned hydrocarbon and particulate emissions. The Gamma prototype aimed to improve the amount of vaporized fuel in the pre-chambers while simultaneously reducing the amount of liquid fuel in the pre-chambers. The Gamma prototype avoided the use of the direct pencil type spray profile. Instead, the fuel spray was air-guided by rebounding the fuel off of a re-designed piston surface and into the pre-chambers which were re-located in the cylinder head. The approach allowed significantly longer mixing time, which increased vaporization of the fuel. To further enhance mixing and direct the fuel, the charge motion tumble was improved over the base production geometry by changing the intake valve angle and corresponding port design.

The new spray profile had the added benefit of eliminating the limitation of wetting the combustion chamber dome. So the included spray cone angle was increased to 20° to further assist fuel mixing. Sprays with included spray angles of 70°, 90°, and 140° were investigated at SOI of 40° bTDC. At 60° bTDC SOI, sprays with included spray angles of 40°, 80°, and 140° were evaluated. The velocity vector field was examined by creating various cut-planes along the cylinder. Comparing the velocity vectors of the cells along the two centerline cut-planes yielded interesting findings. The

pre-chamber connecting orifices in the Gamma prototype were located in a region of significant recirculation. The charge mixture was circulated back towards the center of the combustion chamber instead of being inducted into the pre-chamber. Co-incidentally, 90° rotated in the azimuthal direction, the flow field was extremely favorable for re-locating the pre-chambers.

The Delta prototype featured the piston orientation of the Gamma prototype, but the pre-chambers were relocated 90° in the azimuthal direction in the cylinder head. The same parametric study of SOI and spray angle used to evaluate the Gamma prototype was applied to evaluate the Delta prototype. The highest amount of vaporized fuel in the two pre-chambers at TDC for the Delta prototype was associated with the 140° included spray angle and 60° bTDC SOI, and a 1 mg injection yielded $\phi = 0.29$ and $\phi = 0.30$ in pre-chambers A and B, respectively. The vaporized fuel fraction was 100% for both pre-chambers, a significant improvement over the Beta prototype.

The Epsilon prototype was identical to the Delta prototype, but the piston was rotated 90° in the azimuthal direction so the injection event could benefit from the proper orientation of the piston scallops. The intake and exhaust valve timings for the Epsilon prototype were identified using GT-Power to achieve the largest trapped air mass given the range of authority of the factory variable valve timing. The new piston orientation required the exhaust valve to be advanced by 10 CAD to prevent piston and valve interaction. The intake valve timing remained unchanged. The same parametric study of spray cone angle and SOI used for the Gamma and Delta designs was applied to the Epsilon prototype. The Epsilon prototype was able to induct a larger amount of charge mixture into the pre-chambers using the 20° and 40° included spray angles in comparison with the Delta prototype. These spray angles relied more significantly on the piston crown geometry to guide the charge mixture into the pre-chambers. The best fueling strategy for the Epsilon prototype occurred with the same SOI and same spray angle as the Delta prototype, and resulted in an approximately equal amount of charge mixture inducted in each pre-chamber. The tumble, caused by the valve angle and port geometry, was sufficiently intense that the tumble flow was the primary transport mechanism for the induction of the charge mixture into the pre-chambers at the included spray angle of 70°.

The Zeta prototype featured the same combustion chamber geometry as the Epsilon prototype, but the piston crown geometry was modified to avoid piston and valve interaction. A similar parametric study of spray cone angle, included spray angle, and SOI was conducted for the Zeta prototype. The spray pattern with the best results for the Zeta prototype was achieved with a 20° included spray cone angle

Table 3.4: Comparison of the model predictions for fuel mass and vapor fraction by region in the various prototypes at TDC for a 1 mg booster injection. The best results for pre-chamber equivalence ratio for the different spray cone angles and included spray angles considered are presented for each design.

Model	Start of Injection[a] [°bTDC]	Main Chamber ϕ	Vapor Fraction	Pre-Chamber A ϕ	Vapor Fraction	Pre-Chamber B ϕ	Vapor Fraction
Alpha	20°	0	6%	0.15	41%	0.13	46%
Beta	40°	0.01	81%	0.61	45%	0.63	46%
Gamma	60°	0.04	96%	0.09	100%	0.19	100%
Delta	60°	0.04	87%	0.29	100%	0.3	100%
Epsilon	60°	0.04	88%	0.29	100%	0.28	100%

[a] bTDC

and a 140° included spray angle. The results for the equivalence ratio at TDC in the pre-chambers and the main chamber for each of the prototype designs are compared in Table 3.4. The model predictions show the target goals of controlling the relative fuel quantities in the pre-chambers and the main chamber were met in the Delta, Epsilon and Zeta designs, and the Zeta design further achieved complete vaporization of the fuel in the pre-chamber with 98% vaporization in the main chamber.

The success of the Zeta prototype was due to the bulk charge motion developing a split reverse tumble motion. The intake port, combustion chamber dome, and piston geometry were designed to enable this motion. The fuel injected into the main chamber during the booster injection was successfully vaporized and transported towards and inducted into the pre-chambers. Figure 3.5 shows the velocity vector field of the Zeta prototype 1 mg fuel injection simulation on the centerline cut plane at 60° bTDC.

Based on the positive results for the Zeta model predictions for fuel distribution and phase, a larger parametric space for fuel mass was explored for the Zeta prototype using a 20° spray cone angle and a 140° included spray angle, with fueling amounts from 1 mg to 7 mg and SOIs of 50°, 60° and 70°. Table 3.5 summarizes the results for fuel mass by region. The SOI of 60° bTDC yielded the best results in terms of equivalence ratios of vaporized fuel in the pre-chambers and the main chamber. Figure 3.6 presents the equivalence ratio in the pre-chambers and the main chamber for SOI of 60° bTDC as a function of the booster fuel mass injected. The pre-chambers achieved near stoichiometric mixtures of fully vaporized fuel with the 7 mg booster injection. The results also show the main chamber was fuel lean throughout the range
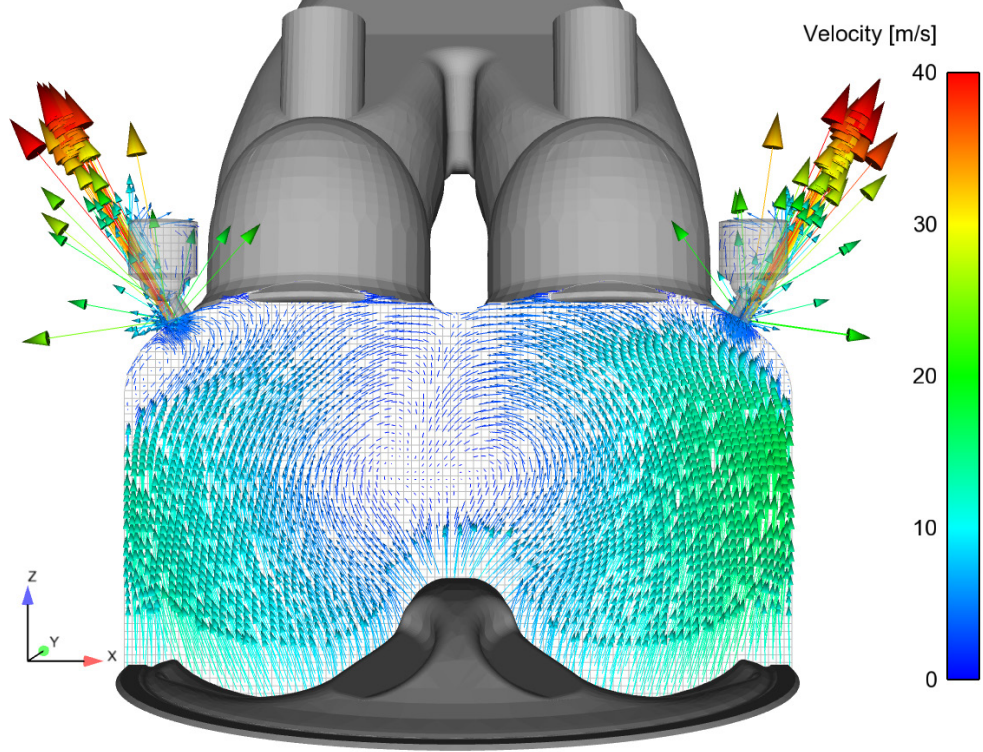
Figure 3.5: Velocity vector field at the centerline cut plane of the Zeta prototype at 70° bTDC highlighting the split reverse tumble motion of the bulk flow field for 1 mg of fuel injected at SOI = 60° bTDC.

of fuel mass considered.

Figure 3.6 and Table 3.5 show the amount of fuel injected in the booster event can be lower than 7 mg and achieve $\phi > 0.8$ conditions in the pre-chambers. The results indicate when the booster fueling event is superimposed on the conditions created by a global fuel injection event, near stoichiometric conditions can be achieved in the pre-chambers.

The results of the computational simulations were also interrogated to understand the transient behavior of the flow into and out of the pre-chambers. Using the flow field near the pre-chamber orifices, a flow field alignment metric was developed with the form:

$$Vel_{ratio} = \frac{\hat{V}_{zone} \bullet \hat{n}_{orifice}}{|\hat{V}_{zone}|} \tag{3.1}$$

where $\hat{V}_{zone}$ is the average velocity vector in a spherical region outside the pre-chamber orifices and in the main chamber, and $\hat{n}_{orifice}$ is the vector normal to the planar area of the opening of each orifice, with the positive direction chosen as towards

Table 3.5: Summary of model predictions for fuel mass and vapor fraction by region in the Zeta prototype at TDC for an included spray cone angle of 20° and an included spray angle of 140°.

Fueling Amount	Start of Injection[a] [°bTDC]	Main Chamber		Pre-Chamber A		Pre-Chamber B	
		ϕ	Vapor Fraction	ϕ	Vapor Fraction	ϕ	Vapor Fraction
1 mg	60°	0.06	98%	0.28	100%	0.27	100%
2 mg	60°	0.11	98%	0.48	100%	0.47	100%
3 mg	50°	0.17	95%	0.52	100%	0.52	100%
3 mg	60°	0.17	97%	0.62	100%	0.62	100%
3 mg	70°	0.17	98%	0.61	100%	0.59	100%
4 mg	50°	0.22	94%	0.61	100%	0.60	100%
4 mg	60°	0.22	95%	0.74	100%	0.74	100%
4 mg	70°	0.23	98%	0.72	100%	0.71	100%
5 mg	60°	0.28	93%	0.78	100%	0.83	100%
6 mg	60°	0.33	91%	0.90	100%	0.91	100%
7 mg	60°	0.38	90%	0.97	100%	0.97	100%

[a] bTDC

the pre-chamber. The dot product of $\hat{V}_{zone}$ and $\hat{n}_{orifice}$ gives an absolute measure of how well the flow field is aligned with the orifice orientation.

Normalizing Vel_{ratio} by the magnitude of $\hat{V}_{zone}$ enables direct comparison between different flow conditions and engine designs. In this form, Vel_{ratio} quantifies the contribution of the local flow to filling and emptying the pre-chamber, where Vel_{ratio} can have a value between -1 and 1. A Vel_{ratio} value of 0 indicates the local flow is bypassing the connecting orifice. A Vel_{ratio} value of +1 indicates the local flow is perfectly aligned and filling the pre-chamber. A Vel_{ratio} value of -1 indicates the flow is perfectly aligned and emptying the pre-chamber.

Figure 3.7 and Figure 3.8 present the results for Vel_{ratio} for the Beta and Zeta prototypes, respectively. The Beta and Zeta simulations were selected to highlight key features of the transient flow behavior. In the figures, the time histories for Vel_{ratio} for each of the six orifices are presented. The three orifices for each of the two pre-chambers are designated by their location relative to the exhaust valves, intake valves, and the central position.

Both prototype engine designs showed the full range of potential values for Vel_{ratio} from -1 to +1. When the piston changed directions, either at BDC (540 CAD) or TDC (720 CAD), the Vel_{ratio} captured the expected change in flow direction. Both engine designs showed the pre-chambers should be well-purged during the expansion
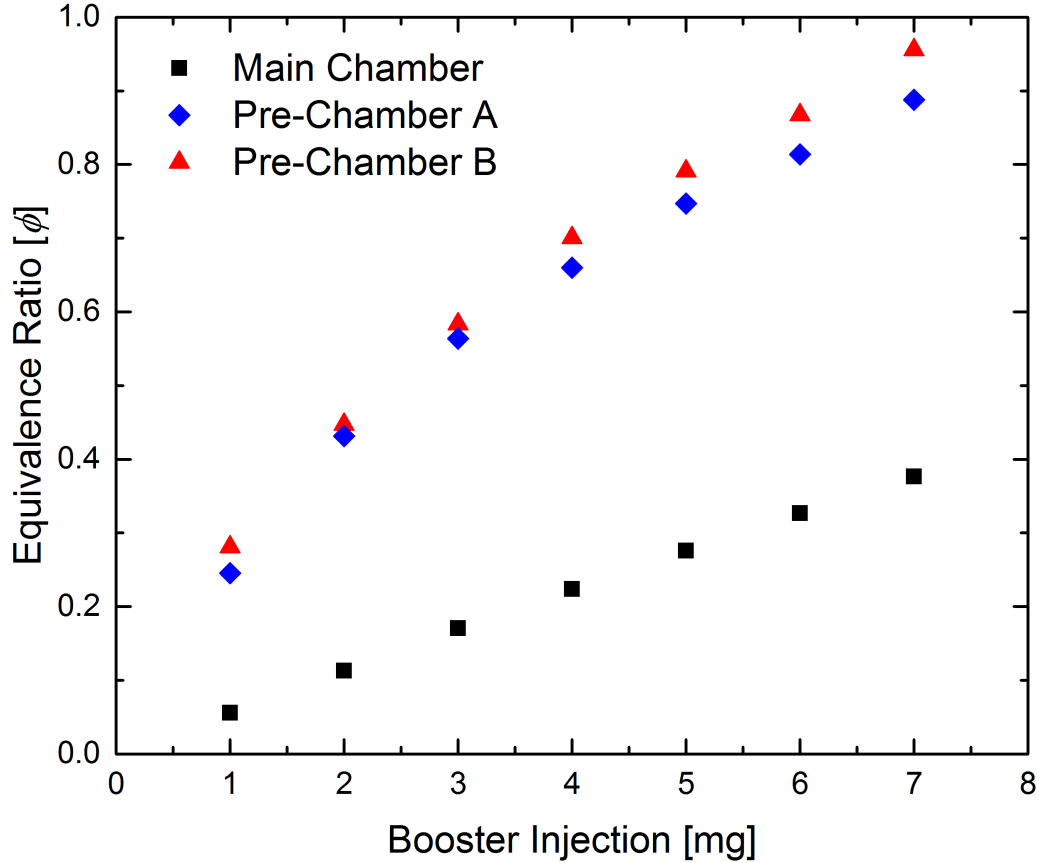
Figure 3.6: Equivalence ratio by region as a function of the fuel mass in the booster injection event for 20° included spray cone angle, 140° included spray angle, and SOI of 60° bTDC.

stroke. The Beta prototype had an intake valve closing event, IVC, at 623 CAD, while the Zeta prototype had an intake valve closing event at 582 CAD. Both engine designs showed flow sensitivity immediately following IVC; however, the Zeta flow was more sensitive, with larger oscillations in Vel_{ratio} over a longer portion of the cycle. The lower sensitivity of the Beta design was due to the local flow being saturated in the alignment with the orifices, with $Vel_{ratio} \simeq 1$, for a majority of the time between IVC and TDC. Recall the Beta design targeted direct filling of the pre-chambers by the booster fuel spray, and the direct alignment of the liquid fuel spray led to unacceptably high liquid films in the pre-chamber.

When comparing the values for Vel_{ratio} for the different orifices for the Zeta predictions in Figure 3.7, there is a period of time before the intake valve closes (~ 560 CAD to 580 CAD) where the orifices on the exhaust side of the chamber had flow exiting the pre-chambers while flow through the other orifices were filling the pre-chambers. This may lead to short-circuiting of the flow, and this type of behavior
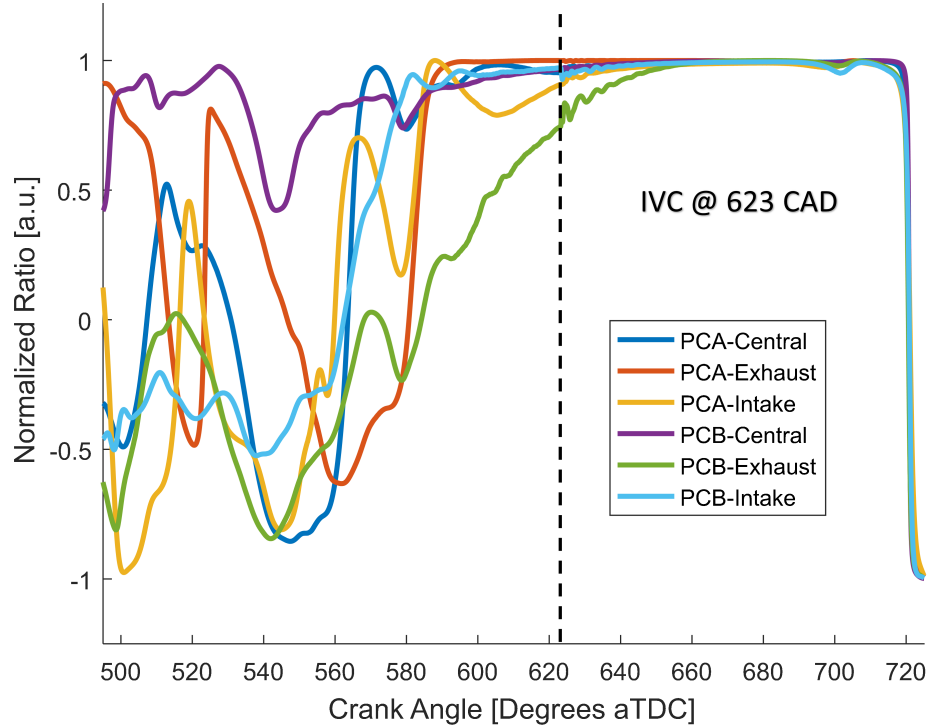
Figure 3.7: Vel_{ratio} for the pre-chamber orifices of the Beta prototype for a non-spraying simulation.

can be a constraint on the timing of the booster fuel injection event. However, this type of behavior can also be desirable for purging the residuals from the pre-chambers depending on the timing. Similar simultaneous inflow and outflow behavior, although more erratic, was observed for the Beta model predictions before IVC. Note the decaying oscillations observed after IVC in the Zeta prototype results are likely due to the rapid numerical separation of the intake port and the combustion chamber and are likely an artifact of the solver. All convergence criteria are satisfied through this portion of the cycle. Soon after IVC, all orifices exhibited filling behavior for the Zeta model predictions (and the Beta model predictions). This portion of the cycle is when the booster fuel injection event occurred. A significant window of time when the flow is well-aligned with filling the pre-chambers is critical during this portion of the cycle to enable flexibility in the timing of the booster fuel injection event.

The intake and exhaust orifices for each pre-chamber were at significantly different angles for the Zeta prototype, yet Figure 3.8 shows the Vel_{ratio} values were comparable to the values for the central orifice. In other words, the flow alignment metric results for the Zeta prototype indicate little sensitivity of the flow to the angle of the pre-chamber orifices. This allows flexibility in strategically targeting the exhaust orifices

59
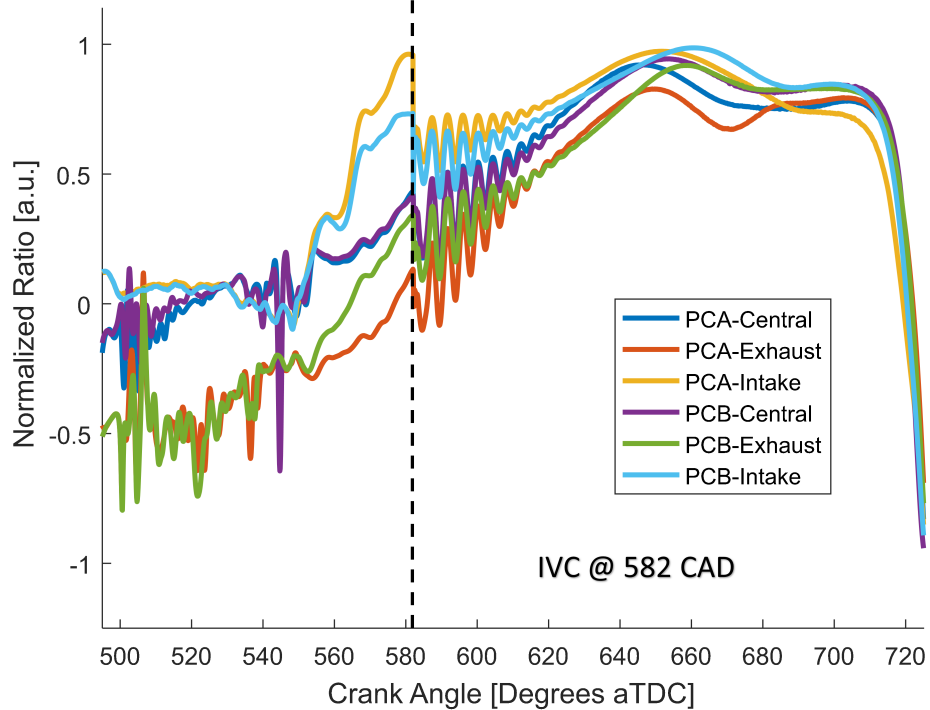
Figure 3.8: Vel_{ratio} for the pre-chamber orifices of the Zeta prototype for a non-spraying simulation.

of each pre-chamber to enable the shortest and most complete main chamber burn possible.

3.7 Summary and Conclusions

This work documented the development and evaluation of a new engine concept using computational simulations of non-reacting flow. The objective of the computational study was to evaluate the feasibility of several engine design configurations combined with fuel injection strategies to create local fuel/air mixtures in the pre-chambers above the ignition and flammability limits, while maintaining lean conditions in the main combustion chamber.

Through a series of six design iterations, the Zeta prototype was able to achieve the desired ignitable mixture in the pre-chamber at TDC by using an appropriate fuel injection profile and flow control via the piston, cylinder head, and pre-chamber geometry. The ignitable mixture was achieved using an injection strategy of 7 mg of fuel at 60° bTDC SOI with a spray pattern featuring a 20° included spray cone angle and a 140° included spray angle. Each pre-chamber was able to achieve $\phi = 0.97$, which was near the nominal design target, while maintain a sufficiently lean global

equivalence ratio of $\phi = 0.38$ in the main chamber. The fuel was fully vaporized in the pre-chambers and was 90% vaporized in the main chamber. This was achieved by the two, diametrically opposed, pre-chambers being indirectly fueled from a centrally mounted fuel injector in the main chamber and using the bulk charge motion to improve fuel spray mixing. The results of this design study show difficulties associated with pre-chamber charge preparation of indirectly fueled pre-chamber engine designs can be overcome.

Additionally, a flow field alignment metric was developed based on the flow field near the pre-chamber orifices. The metric quantified the contribution of the local flow to the filling and emptying of the pre-chamber and aided in understanding of the transient nature of the pre-chamber filling dynamics. Regardless of combustion chamber geometry, number of orifices, or pre-chamber location, the optimal injection strategy will be one that introduces the appropriate amount of vaporized fuel near the pre-chamber orifices at a span of time where the near orifice flow field is at the highest alignment with the normal vector of the orifice opening.

Current work focuses on building, characterizing and testing of the Zeta prototype via an optically accessible single cylinder engine. Experimental studies are in progress to validate the CFD model predictions and to further develop this lean burn combustion engine concept.

3.8   Acknowledgements

3.9   Definitions / Abbreviations

Abbreviations	Definition
Letters	
BDC	Bottom Dead Center
bTDC	before Top Dead Center
CFD	Computational Fluid Dynamics
DI	Direct Injection
KH	Kevin Helmholtz
PFI	Port Fuel Injection
RPM	Revolutions Per Minute
RT	Rayleigh Taylor
TDC	Top Dead Center
Greek Symbols	
γ	Ratio of Specific Heats
ε	Turbulent Dissipation
κ	Turbulent Kinetic Energy
ϕ	Equivalence Ratio
Symbols	
$^\circ$	Degrees

CHAPTER IV

The Dual Pre-Chamber Engine

4.1 Introduction

Phase 1 of the dual pre-chamber (DPC) engine research and development project ended with the design of an engine geometry which computational fluid dynamics (CFD) modeling results (using the software code Converge, a product of Convergent Science) predicted would achieve targeted flow features for the fuel-to-air equivalence ratio, ϕ. The objective of Phase 2A of the DPC Engine project was to build metal and optically accessible versions of the Zeta prototype in a single-cylinder configuration intended to demonstrate if the hardware achieved the desired flow dynamics predicted by the CFD model. The following sections describe in detail the hardware development and the engine installation.

4.2 Engine Specifications

The physical version of the Zeta DPC prototype engine was built with some modifications compared with the CFD design. The specifications of the computational and physical engines are provided in Table 4.1. Some key differences between the computational and physical Zeta prototypes include the stroke and the compression ratio. The changes in the physical dimensions of the engine were made to balance between using the existing single-cylinder infrastructure at the University of Michigan (UM) and using the geometry of the CFD simulations which leveraged a Hyundai design for a four cylinder 2.0 L forced-induction gasoline production engine.

Figure 4.1 presents an image of the DPC prototype installed in room 1096 of the W.E. Lay Automotive Laboratory at the UM. The engine was supported by a dynamometer, temperature-controlled coolant system, piston-based fueling system, intake air system with boosted pressure capability, intake and exhaust plenums, and

Table 4.1: Summary of the CFD and physical engine specifications for the DPC Zeta Prototype.

Specification	CFD Zeta Prototype	Physical Zeta Prototype
Bore	86.0 mm	86.0 mm
Stoke	86.0 mm	76.5 mm
Connecting Rod Length	146.25 mm	$\sim$ 141 mm
Wrist Pin Offset	0.8 mm	0.0 mm
Compression Ratio	12.56:1	$\sim$ 10.66:1
RPM	2000	600
Intake Valve Diameter	35.0 mm	35.0 mm
Intake Valve Opening[a]	316 CAD	280 CAD
Intake Valve Closing[a]	582 CAD	634 CAD
Exhaust Valve Diameter	29.0 mm	29.0 mm
Exhaust Valve Opening[a]	164 CAD	100 CAD
Exhaust Valve Closing[a]	403 CAD	448 CAD

[a] Valve events are specified at 1 mm lift.

a temperature and pressure controlled oil system. The in-house designed and custom built intake and exhaust plenums, required to damp pressure oscillations, are visible in Figure 4.1. A custom data acquisition and signal processing system (shown in Figure 4.2) was designed and built for the DPC system to interact with the engine, the dynamometer and the custom designed and built fuel injectors provided by Delphi.

Two configurations of the physical engine hardware were created for testing. One configuration used a full-metal cylinder liner, and was used to test clearances, seals, valve timing and establish motoring baseline performance. The second configuration used a transparent cylinder liner made from Corning HPFS 7980UV-OC3 fused silica to allow optical access to visualize the fuel and air flow fields. Figure 4.3 presents an image of the fully-transparent cylinder liner installed in the DPC Zeta prototype engine.
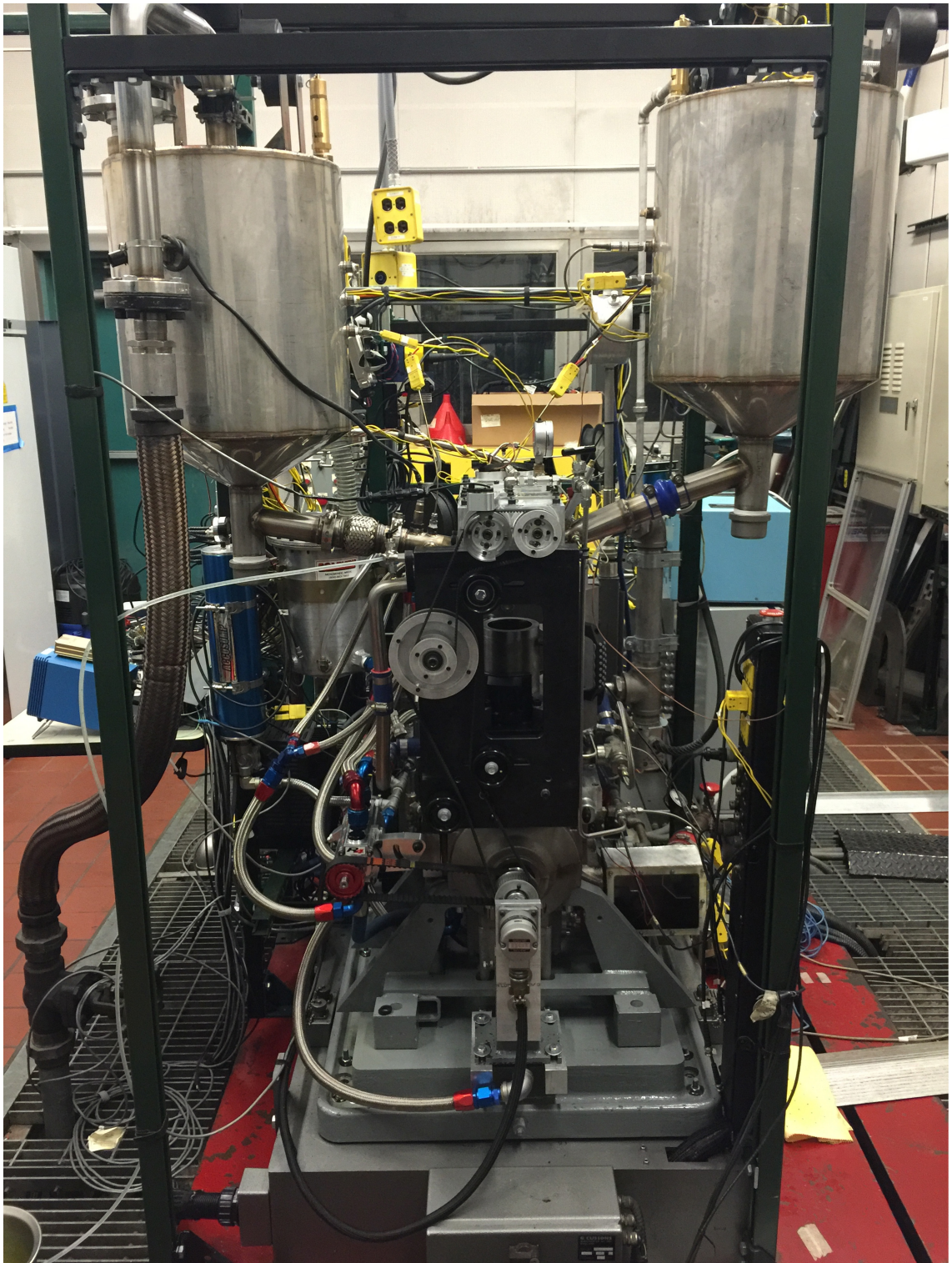
Figure 4.1: DPC prototype engine located in the UM 1096 W.E. Lay Automotive Laboratory test cell.
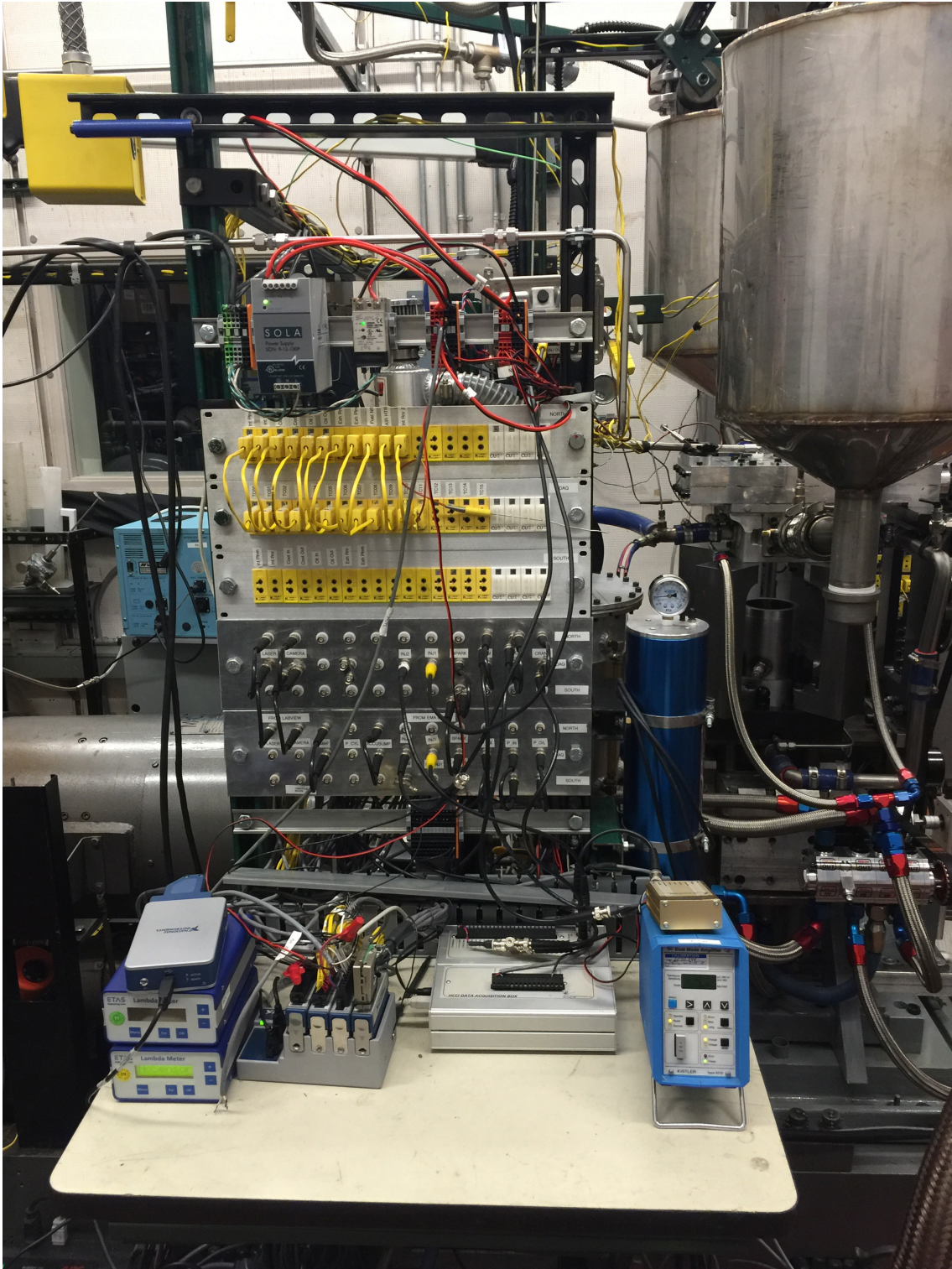
Figure 4.2: The data acquisition and signal generation systems created for the DPC prototype engine.

Figure 4.3: The fully transparent cylinder liner installed in the Zeta prototype engine and illuminated using the LED lighting system.

4.3 Custom DPC Cylinder Head

The following section highlights important aspects of the custom designed and built Dual Pre-Chamber Engine, specifically focusing on the complicated cylinder head assembly.
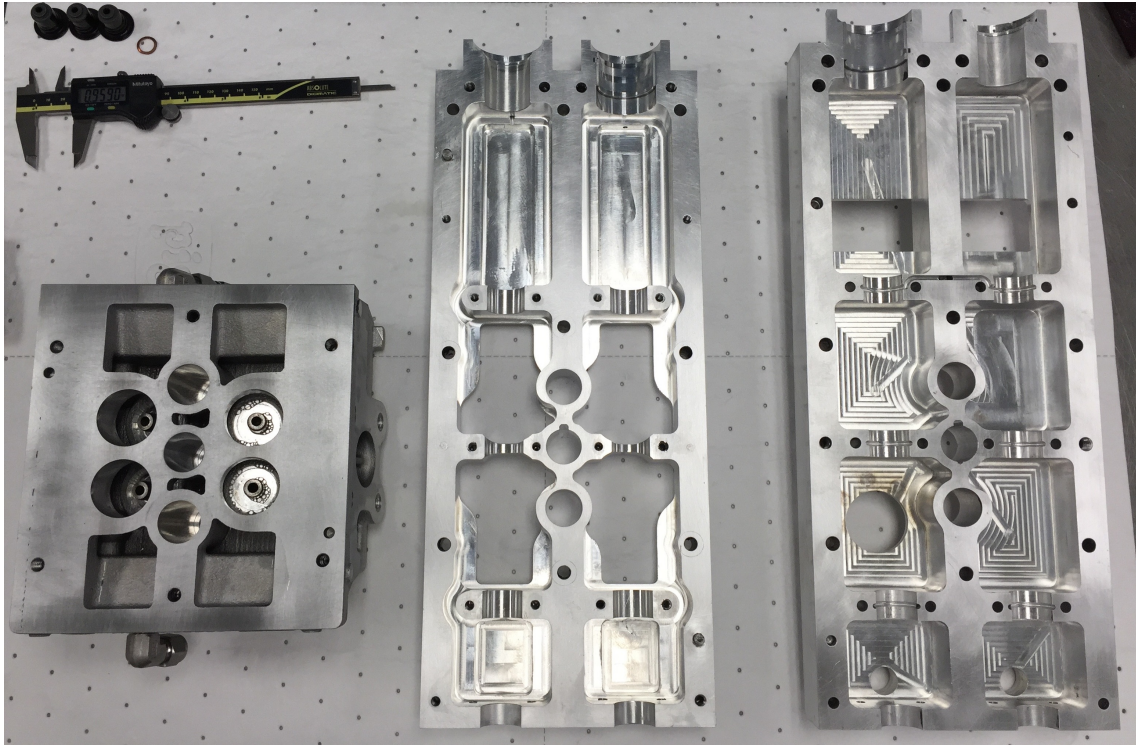
Figure 4.4: Left to Right: Custom cylinder head, Lower cam carrier, upper cam carrier.
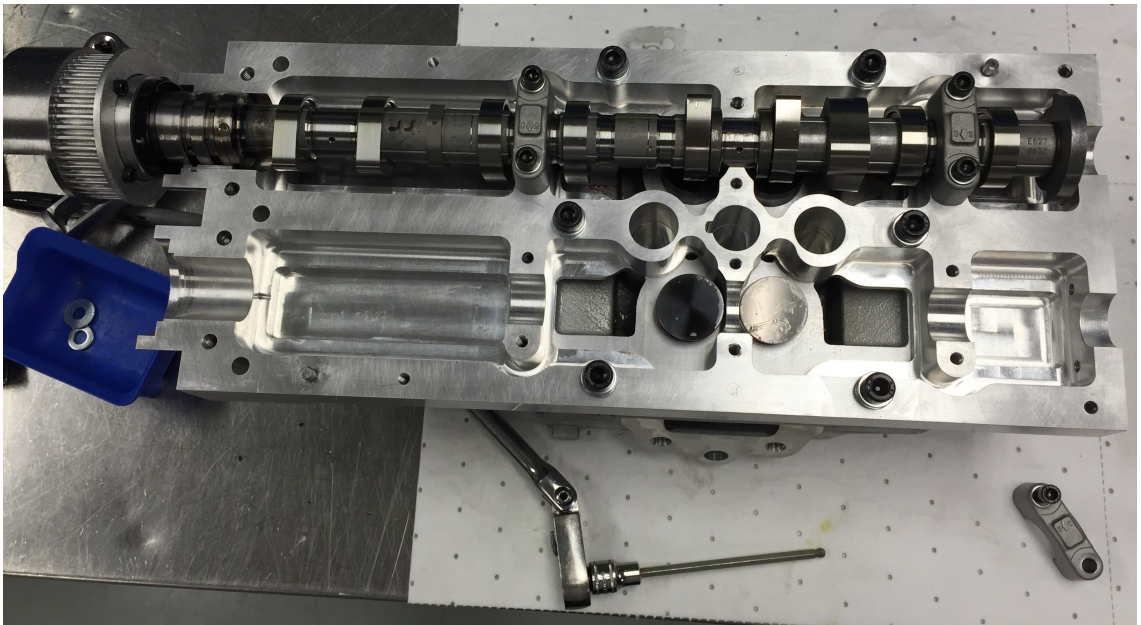
Figure 4.5: Set-up for adjusting proper valve lash prior using lower camshaft carrier and conventional camshaft journal caps, prior to installing and sealing the upper camshaft carrier.

Figure 4.6: Spark plugs, pre-chamber retention nuts, and pre-chamber insert.
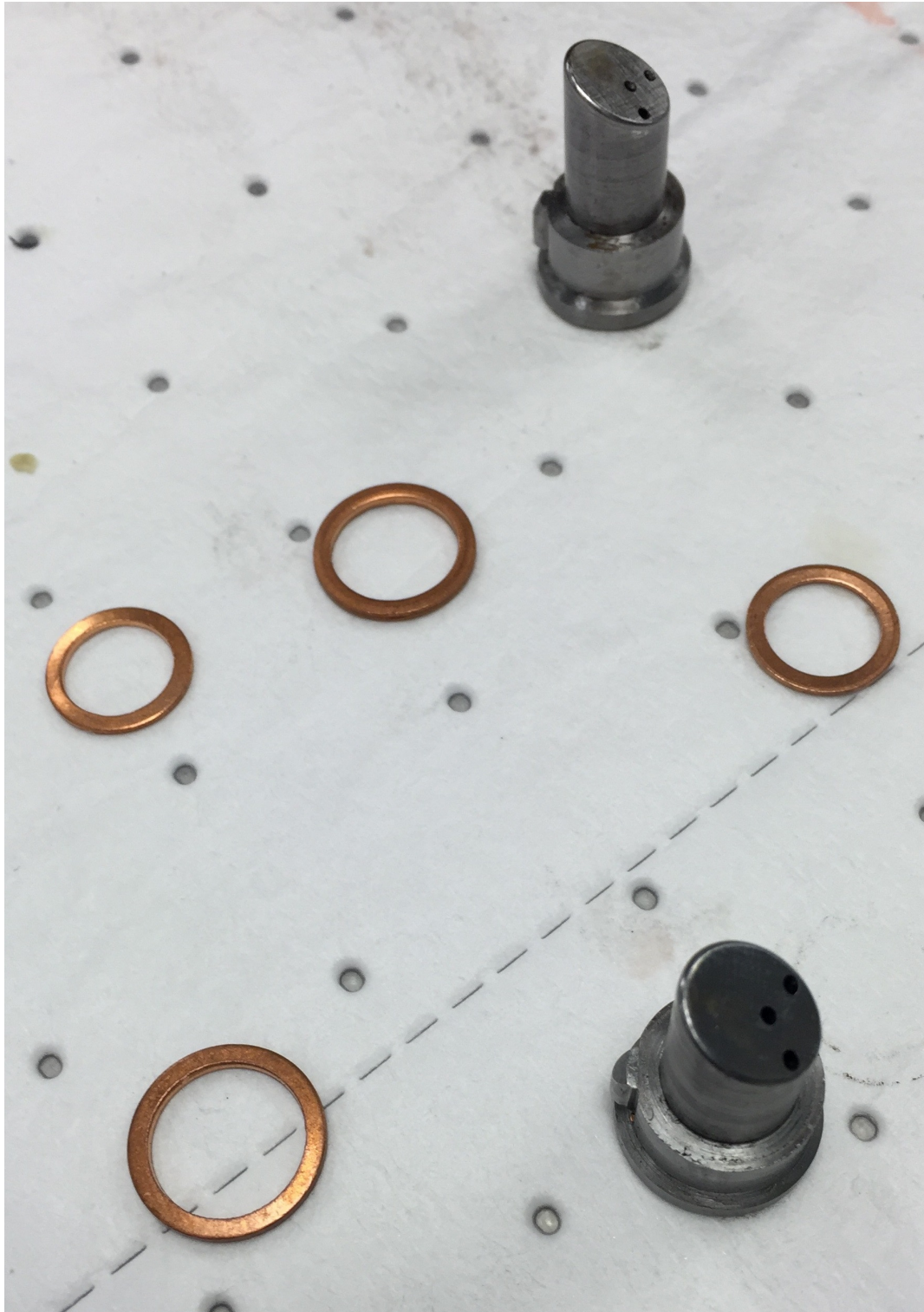
Figure 4.7: Close-up of the pre-chamber insert featuring the pre-chamber orifice geometry.

Figure 4.8: Combustion chamber dome featuring the pre-chamber location at the 3 o'clock and 9 o'clock positions. The 6 o'clock shadow is the pressure transducer port. A brass plug is installed in the center, where the direct injector is installed.
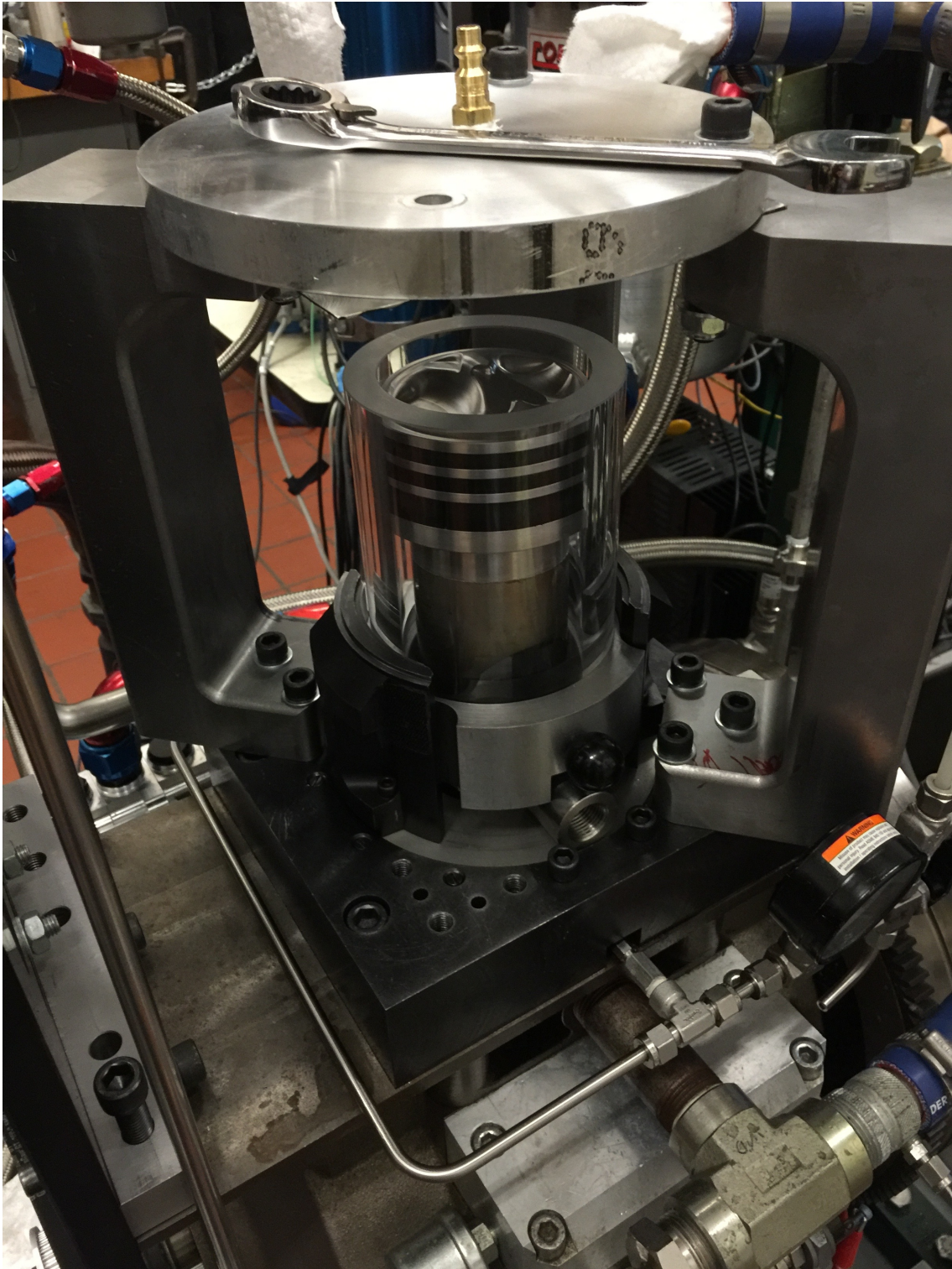
Figure 4.9: Assembly used to determine the health of Torlon piston rings by quantifying leakage rate.

Figure 4.10: Profile close-up view of the Zeta prototype piston geometry installed in the optical liner with the Torlon compression rings.

Figure 4.11: Top view of the Zeta prototype piston geometry with modeling clay used for checking injector, valve, and combustion chamber dome clearancing.

4.4 Custom Fuel Injector

The CFD studies were used to determine an optimized fuel spray patterns that can indirectly fuel the two pre-chambers using a centrally mounted gasoline direct injector. The desired spray patterns, seen in Figure 4.12, would feature two plumes that are 180 degrees opposed with cone angles of 20° and a center-center spray angle of 140°. This injector would be operated at 200 bar injection pressures and 0 – 10 mg fuel delivery.
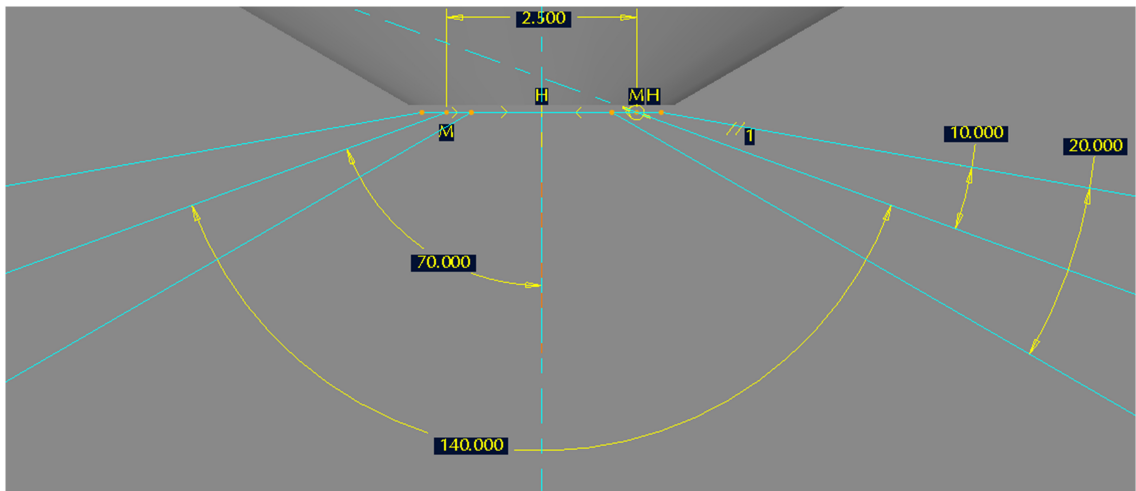
Figure 4.12: Desired spray profile from CFD.

Several manufacturers were approached to build a fuel injector system which would create the fuel sprays identified in the CFD study. Some challenges to this aspect of the project were the timeline to build and deliver the system to the UM, compatibility with the Zeta head architecture, and the ability to create a fuel injector with a large spread angle between the two fuel spray plumes. A decision matrix, outlined in Table 4.2 and Table 4.3, was developed to aid in the selection of the best suited manufacturer.

Table 4.2: Custom fuel injector manufacturer decision matrix using gasoline direct injection technology.

Gasoline DI Technology	Weight	Delphi 3/-3		Bosch 3/-3		Continental 3/-3		Xtreme-DI 3/-3		Exergy 3/-3	SNS 3/-3	Denso 3/-3	
Able to meet desired timing	10	2	Yes	0	8-12 weeks	-1	No	3	4 weeks			0	?
Desired spray characteristics for commercialization	9	3	Yes	3	Yes	3	Yes	1	Maybe			3	Yes
Manufacturability of desired injector & spray pattern	8	2	Yes	3	Cone angle	3	Cone angle	3		DIESEL ONLY	DIESEL ONLY	1	
Carryover feasibility to future project phases	8	3	Great	3	Great	3	Great	-2				2	
Development support and communication	7	3	Excellent	2	Good	3	Excellent	1	Marginal			-2	
Facility upgrade cost (ECU, Fuel cart, etc.)	6	1	ECU	3	As is	1	ECU	3	As is			0	???
Fueling and controlling strategy	6	2		3	As is	2		3	As is			0	???
Cost	5	2	$4K-6K per	0	$3K-5K per	2	?	3	$1K per			0	?
		136		125		114		105				37	

Table 4.3: Custom fuel injector manufacturer decision matrix using diesel common rail injection technology.

Diesel Technology	Weight	Delphi 3/-3		Bosch 3/-3		Continen 3/-3		Xtreme-DI 3/-3	Exergy 3/-3	SNS 3/-3		Denso 3/-3	
Able to meet desired timing	10	2	YES	1	8-12 weeks	-1	No		3	3	3 weeks	0	?
Desired spray characteristics for commercialization	9	-2	NO	-2	NO	-2	0		-2	-2	No	-2	NO
Manufacturability of desired injector & spray pattern	8	2	YES	3		0	?		2	2	Yes	1	
Carryover feasibility to future project phases	8	1		1		1		GDI ONLY	1	-1		1	
Development support and communication	7	3	Good	0		3	Good		2	2		-2	
Facility upgrade cost (ECU, Fuel cart, etc.)	6	-2	Fuel Cart	-2	Fuel Cart	-2	Fuel Cart		-2	Fuel Cart	-2	Fuel Cart	-2	Fuel Cart
Fueling and controlling strategy	6	2		2		2			2	2		2	
Cost	5	2	$4K-6K per	0	$3K-5K per	0	?		2	3	$1K per	0	?
		57		24		1			60	49		-16	

78

Based on this decision matrix, the gasoline direct injector route was selected and the optimal partner, was determined to be Delphi. Mark Sellnau of Delphi proposed his group could meet the design criteria for the system and agreed to design and build several prototype fuel injectors for the project at no cost to Hyundai or the UM. This was a significant cost-share in-kind for the project. This custom injector, shown in Figure 4.13, proved to be very challenging to manufacture due to packaging requirements. Figure 4.14 shows the injector nozzle (bottom) view of the custom DPC fuel injector prototype mounted in the DPC cylinder. It was determined a clocking feature, detailed in Figure 4.16 was needed to properly align the two plumes to target the three pre-chamber orifice openings.

Figure 4.13: Custom DPC fuel injector prototype.
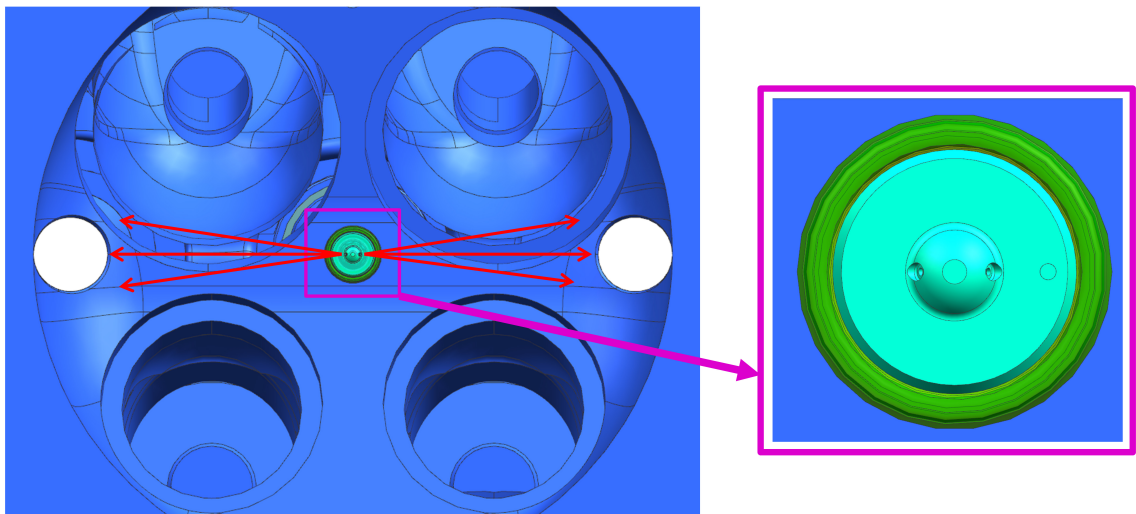
Figure 4.14: Injector nozzle orifice orientation relative to the pre-chambers.

Figure 4.15 shows the side view of the custom DPC fuel injector prototype installed in the DPC engine model. Packaging the alignment feature, wire harness, and spring retention clip proved to be a challenge given the lack of necessary space. Of concern was also the ability to easily remove the injector for servicing purposes and interchangeability for testing various injector configurations. The spring retainer clip, seen in yellow, provides the downwards force to ensure the injector is securely

Figure 4.15: Different views of the fuel injector prototype installed in DPC cylinder head.

seated. The T-bar manifold, which sits on top of the injector, is intended to supply the injector with liquid fuel. The seal to the injector is achieved through an annular o-ring seal. The same T-bar can be clamped down on the cylinder head using two bolts to preload 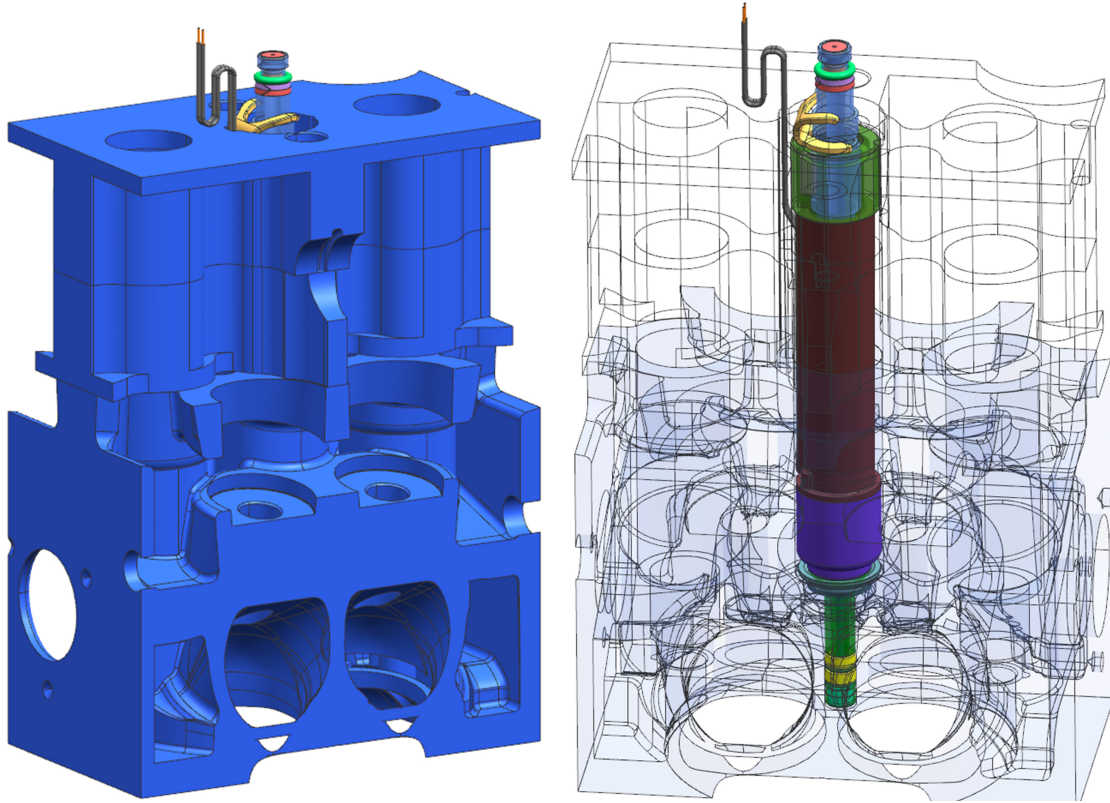the spring retainer clip, thus becoming a retaining T-bar. In a conventional engine, the spring retainer clip easily slides out the side and a standard injector removal tool can be used. Due to the majority of the spring retainer being located with the cylinder head, sideway removal was no longer an option. The overall injector height could not be increased any further. To solve this problem, an integrated ring, seen in green, that sits below the spring retainer clip, seen in yellow, was developed. The integrated ring features multiple attachment points for a custom injector removal tool. This integrated ring also acts as a fine tune alignment feature, allowing multiple rings to be made to change the relative alignment between the injector alignment feature and the cylinder head alignment feature. Additionally, the hard plastic connector was necessary to be removed and a pigtail connector was packaged.

Through several iterations, the fuel injector design and packaging was completed.
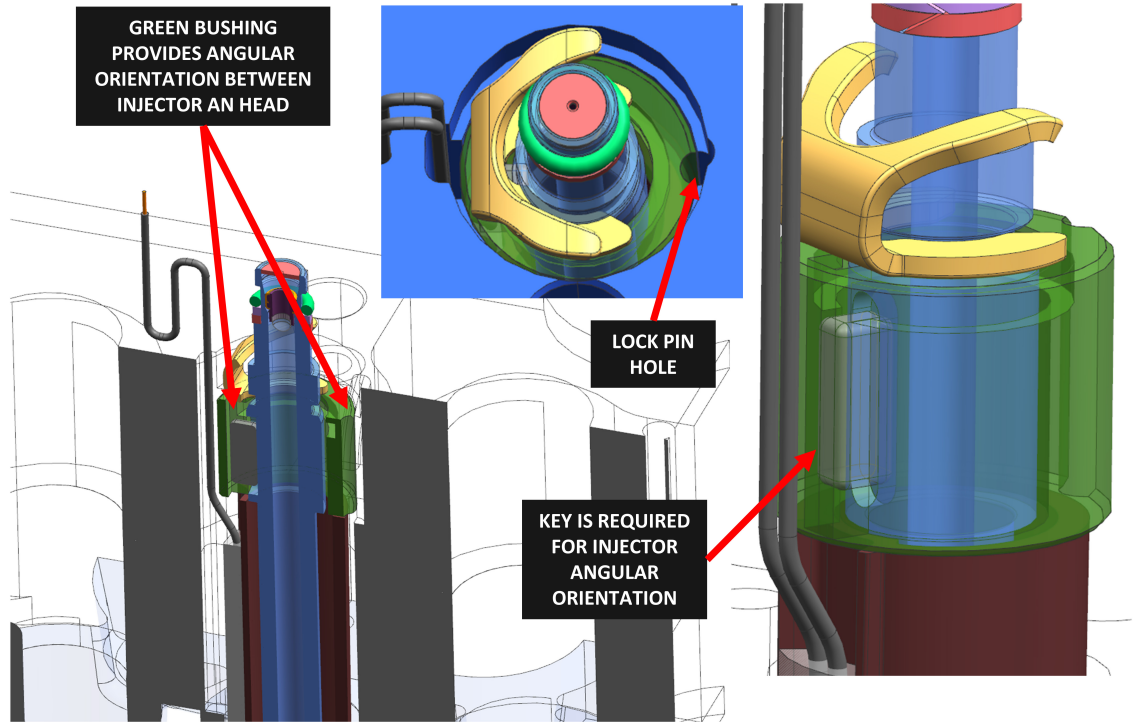
Figure 4.16: Highlights of the injector rotational indexing system for the prototype DPC fuel injector. The injector angular orientation relative to the cylinder head will be accomplished via the green bushing that locks to the cylinder head by inserting a lock pin.

Figure 4.17 shows the body of one of the fabricated prototype fuel injectors, and Figure 4.18 shows one of the fuel injectors installed in the DPC Zeta prototype head. The fuel injector was based on a modified version of the production Delphi Multec 14 (M14) solenoid injector. Each injector featured a custom 2-hole nozzle, a keyed angular reference feature to clock orientation, and an extension pigtail. The fuel injector system consisted of a spherical rail, custom retaining T-bar, and custom fuel injector. A batch of six identical fuel injectors were designed and built by Delphi for the project.

Delphi conducted tests of the fuel injector spray properties using n-heptane as the fuel. Figure 4.19 and Figure 4.20 present results of the Delphi DPC injector testing at two rail pressures. The data of Figure 4.19 corresponded to approximately 6.9 mg of fuel injected and showed an average angle between the fuel sprays of 134°. The data of Figure 4.20 corresponded to approximately 9.5 mg of fuel injected and showed an average angle between the fuel sprays of 140° for the same injectors as Figure 4.19. The results indicated the axis of the center of the spray plumes may vary as a function of fuel rail pressure.

Figure 4.17: One physical example of the custom Delphi fuel injectors created for the DPC Zeta prototype engine.
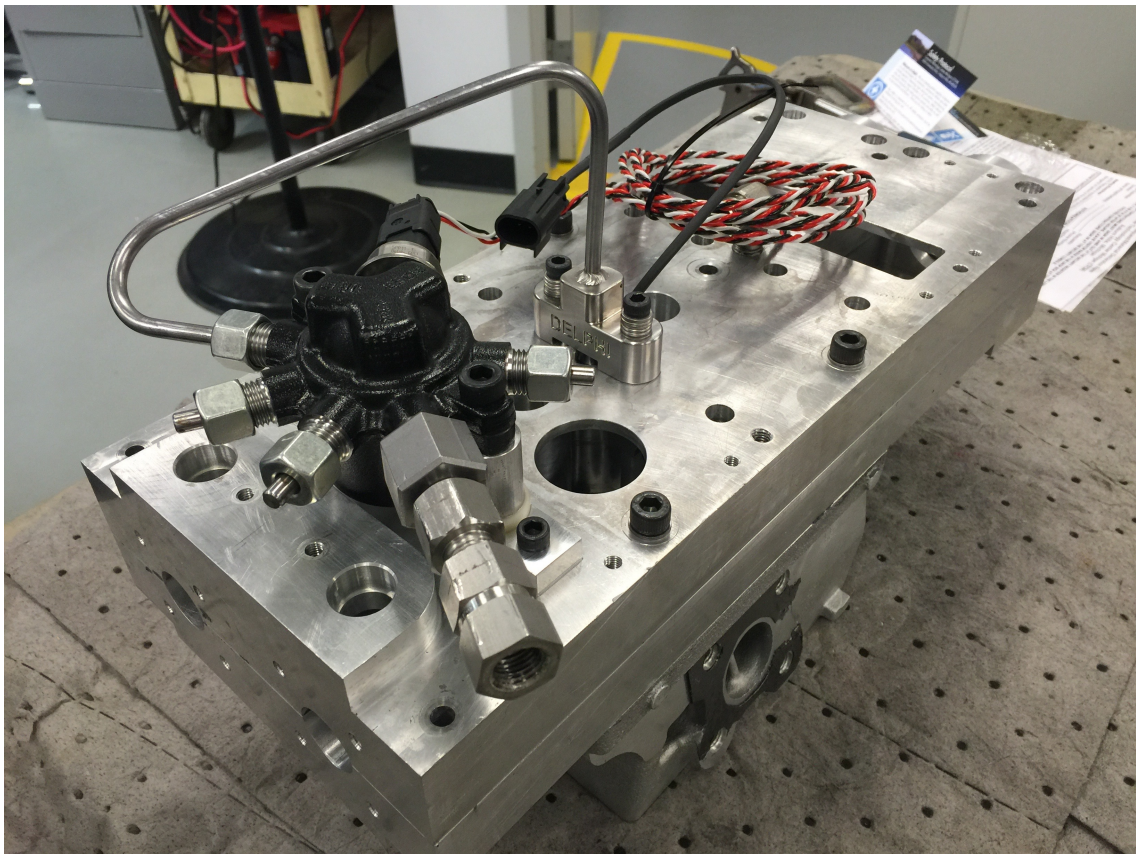
Figure 4.18: One of the Delphi fuel injection systems installed in the DPC Zeta prototype cylinder head.

	Penetration (mm)	Spray Angle (°)	Bend Angle (°)			Penetration (mm)	Spray Angle (°)	Bend Angle (°)
S/N 101	44.7	35.6	1.2		S/N 101	42.6	133.9	0.7
S/N 102	42.2	35.1	1.2		S/N 102	42.3	134.4	0.3
S/N 103	42.8	34.5	-0.3		S/N 103	41.8	134.6	0.3

Figure 4.19: Delphi results for fuel injector performance of injector builds B267-001, B267-002, and B267-003 at a fuel rail pressure of 100 bar, an injection duration of 1.5 ms, and using n-heptane fuel in a confined spray chamber. Included in the figure are the penetration distances, and spray and bend angles for front and side-view imaging.

	Penetration (mm)	Spray Angle (°)	Bend Angle (°)
S/N 101	49.6	43.2	0.9
S/N 102	48.8	44.1	-1.6
S/N 103	49.0	44.5	-0.5

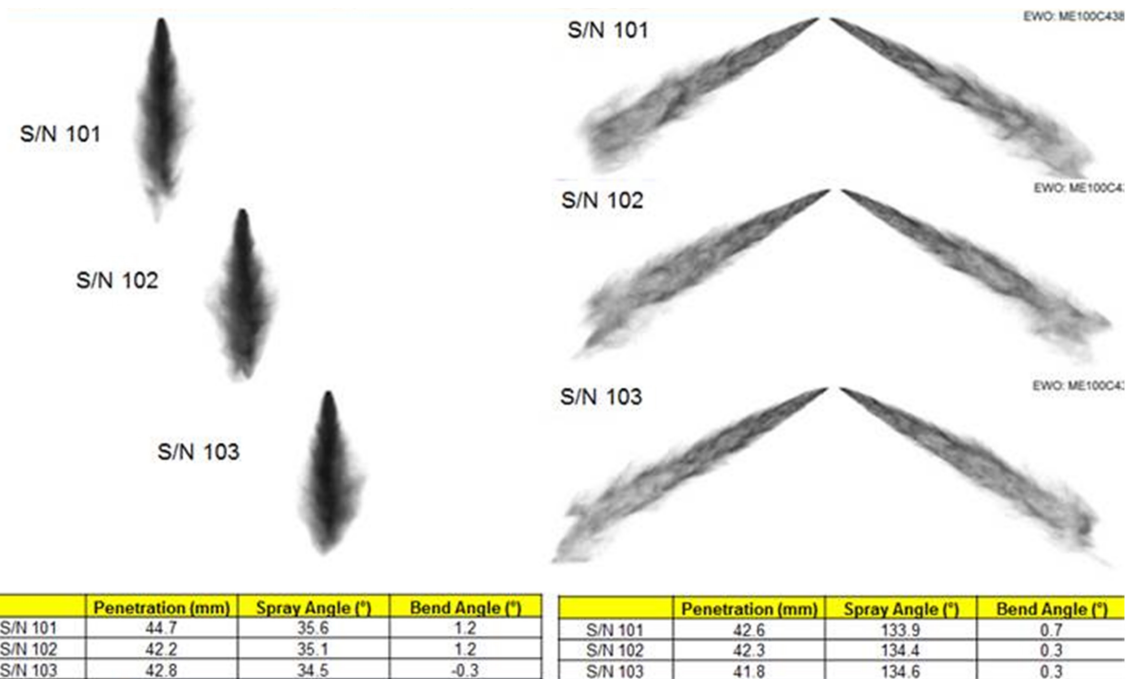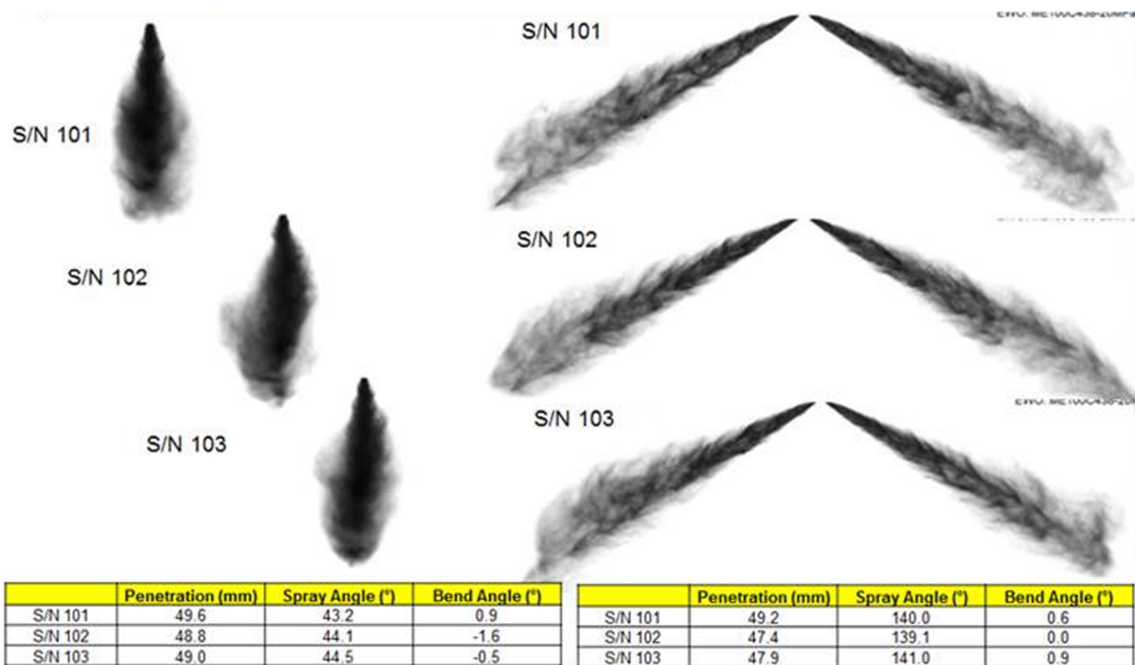|	Penetration (mm)	Spray Angle (°)	Bend Angle (°)
S/N 101	49.2	140.0	0.6
S/N 102	47.4	139.1	0.0
S/N 103	47.9	141.0	0.9

Figure 4.20: Delphi results for fuel injector performance of injector builds B267-001, B267-002, and B267-003 at a fuel rail pressure of 200 bar, an injection duration of 1.5 ms, and using n-heptane fuel in a confined spray chamber. Included in the figure are Delphi determined penetration distances, spray and bend angles for frontal and side-view imaging.

CHAPTER V

Experimental Validation of a Dual Pre-Chamber Internal Combustion Engine Concept

5.1 Introduction

Phase 1 of the dual pre-chamber (DPC) engine research and development project ended with the design of an engine geometry which computational fluid dynamics (CFD) modeling results (using the software code Converge, a product of Convergent Science) predicted would achieve targeted flow features for the fuel-to-air equivalence ratio, ϕ. Specifically, the primary goal of the CFD study was to achieve a flow design which would create near stoichiometric fuel-to-air equivalence ratios ($\phi = 1.0$) in two pre-chambers with lean equivalence ratios ($\phi < 1.0$) in the main combustion chamber. After several iterations on the geometry, a "Zeta" prototype was designed which met the project objectives with good flexibility in fuel injection strategies (e.g. injection timing and fuel mass). In Phase 2A of the DPC Engine project consisted of building metal and optically accessible versions of the Zeta prototype in a single-cylinder configuration. and to demonstrate if the hardware achieved the desired flow dynamics predicted by the CFD model. The objectives of Phase 2B, experimental validation studies, of the DPC Engine project were to demonstrate if the hardware achieved the desired flow dynamics predicted by the CFD model. High-speed imaging of fuel injection and the air charge flow was applied to compare with the simulation results. The following sections describe the diagnostic systems used, the results of the engine testing, and conclusions.

The lower stroke and compression ratio of the physical engine were not expected to change the major flow features which were the focus of the current engine design and testing. Lower engine speed than CFD studies was used in the physical experimental validation studies for component protection, particularly to protect the fused

85

silica liner. Lower engine speed reduces in-cylinder turbulence and therefore fuel/air mixing. Thus, the results of these validation studies were expected to indicate lower mixing outcomes.

5.2 Experimental Approach

5.2.1 Diagnostic Specifications

The two most important diagnostics for the DPC Zeta prototype were the in-cylinder pressure transducer and the imaging system. The transient in-cylinder pressure (which was referenced to the absolute intake manifold pressure) was measured using a Kistler 6125C21 in-cylinder pressure transducer and Kistler 5010B charge amplifier. The intake and exhaust absolute manifold pressures were measured using two Omega DPG409-030A gauges. The analog pressure transducer signal was recorded using a LabView 2012 custom data acquisition program with a 32 bit National Instruments cDAQ-9174 chassis utilizing a National Instruments 9206 card operating at 100 kHz speed. The imaging system consisted of a high speed color digital 1280 x 800 pixel CMOS camera (Vision Research Phantom V711) capable of a 7 gigapixel/second throughput, a high speed macro lens (Nikon 105 mm f/2.8 AAF Micro) for front-view imaging, a high speed macro zoom lens (Nikon 80 – 200 mm f/2.8 AF-D ED Macro) for side-view imaging, and a high-speed LED lighting system consisting of a VideoStrobe-Flood Controller (Visual Instrumentation Corporation 201300AW) operating two 1 x 3 LED arrays (Visual Instrumentation Corporation 900420W) in "flooding" mode. Additional details regarding the camera performance, spectral response of the CMOS sensor, white-balancing and zero signal leveling frequency and procedures can found in Assanis et al. [1]. Approximately a dozen lenses were trialed to identify to the best combination for the front- and side-view imaging studies. The imaging system was focused on the combustion chamber centerline, with the primary focus on the fuel injector nozzles. For the front-view imaging, a resolution of 768 x 256 pixels, a frame rate of 36,000 fps, and exposure setting of 27 μs were used. For the side-view imaging, a resolution of 512 x 512 pixels, a frame rate of 10,000 fps, and exposure setting of 99 μs were used.
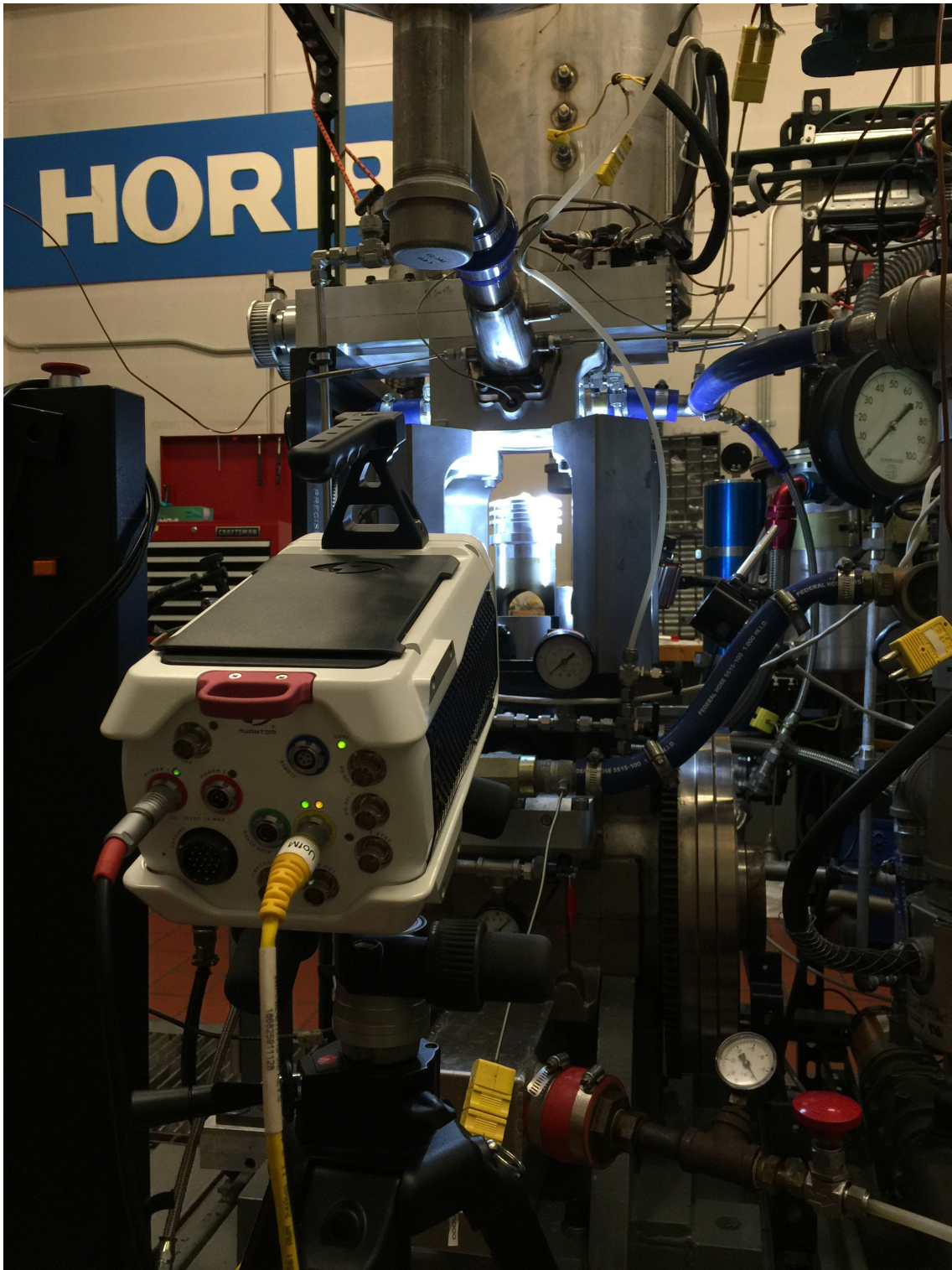
Figure 5.1: High-speed camera system in the configuration for front-view or intake orientation of fuel injection and air flow imaging.
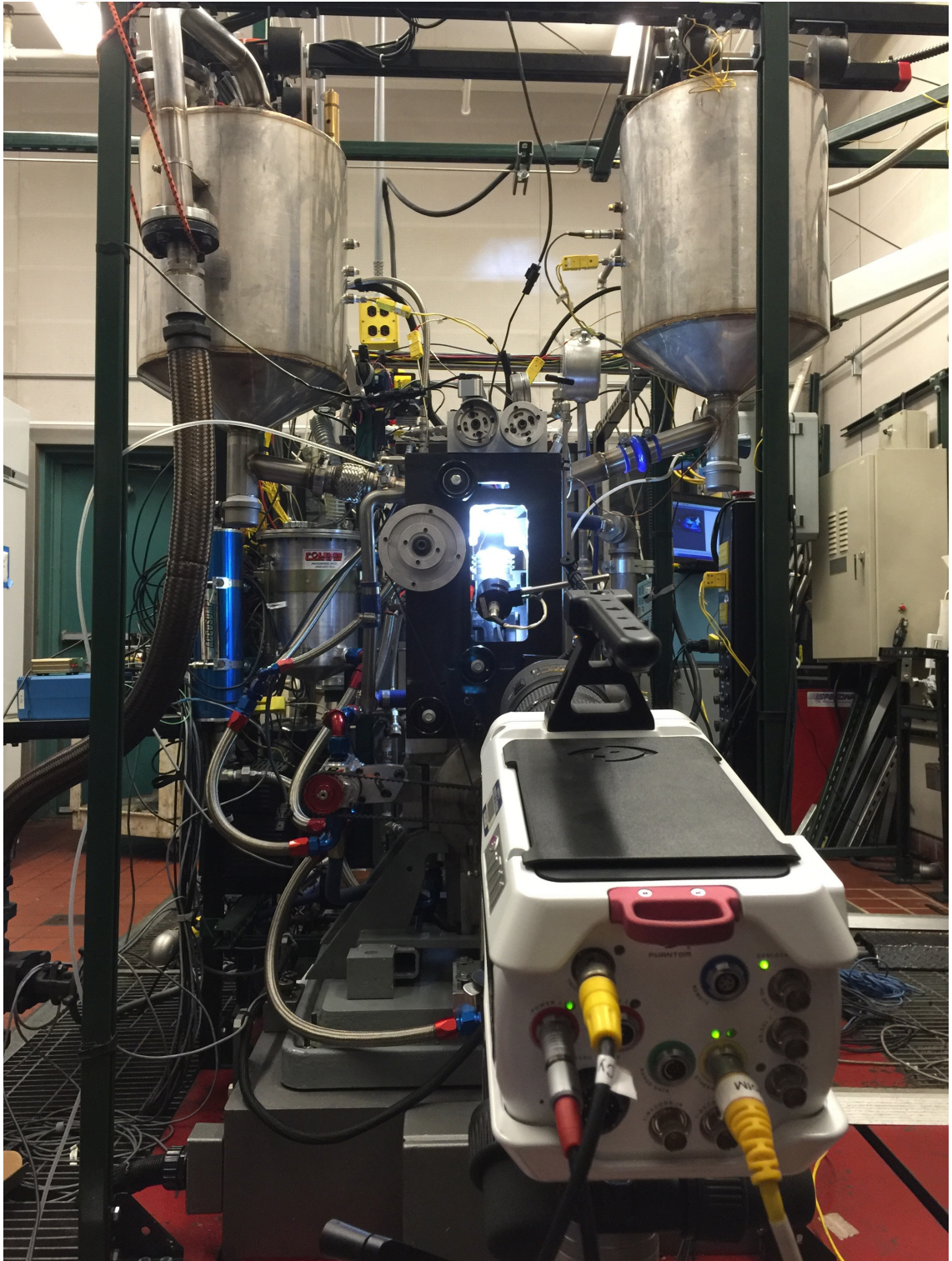
Figure 5.2: High-speed camera system in the configuration for side-view or timing belt orientation of fuel injection and air flow imaging.

The pressure data were used to determine the baseline motoring conditions of the engine, and to establish the integrity or health of the engine in terms of the piston seals and other potential sources of leaks in the air flow. The imaging data were used to determine the quantitative physical characteristics of the fuel sprays and the qualitative characteristics of the air flow (via moisture condensation). Figure 5.1 and Figure 5.2 show the orientation of the camera when imaging from the front and side of the engine, respectively.

5.2.2 Operating Conditions

The fixed engine operating conditions used for the Phase 2 imaging study are provided in Table 5.1. Low speeds were used to protect the metal and optical engine components. A slight pressure rise across the engine was used for the initial engine break-in and imaging studies. A moderate coolant temperature was used as a compromise between condensation on the optical liner and concerns of the effects of thermal expansion that could occur with higher coolant temperatures. A reference grade certification gasoline was used to provide traceable gasoline properties. The fuel rail pressure was slightly lower than the CFD simulations, which used a fuel injection pressure of 150 bar, due to hardware limitations.

Table 5.1: Summary of operating conditions used in the DPC Zeta prototype fuel and air imaging studies.

Parameter	Testing Range
Engine speed	600 ± 5 RPM
Intake Manifold Pressure	95.0 ± 2.0 kPa
Exhaust Manifold Pressure	101.5 ± 2.0 kPa
Coolant Temperature	$45° \pm 3°$ C
Injector Build	B267-001 and B267-005
Fuel Type	HF-0072
Fuel Rail Pressure	100 ± 5 bar
Start of injection (SOI) timing	180°, 120°, 90°, 75°, and 60° bTDC
Injection Duration	0.25, 1.0, and 2.50 ms

5.3 Results

5.3.1 In-cylinder Pressure Diagnostics

Results for the in-cylinder pressure of the Zeta prototype engine during motoring conditions using the metal and fused silica cylinder liners are presented in Figure 5.3. The average maximum in-cylinder pressure was 1580 kPa using the metal liner, and the coefficient of variation (COV) of the maximum pressure for 48 cycles was 0.24%. The data demonstrate the engine successfully retained air pressure throughout the cycle with negligible cycle-to-cycle variability. The performance for the optical liner was also excellent, with a slightly lower average maximum in-cylinder pressure of 1520 kPa and a corresponding COV for peak pressure for 48 cycles of 0.24%. The slightly lower peak pressure is expected with the optical liner as the piston rings will not seal as well with the fused silica liner in comparison with the metal liner.
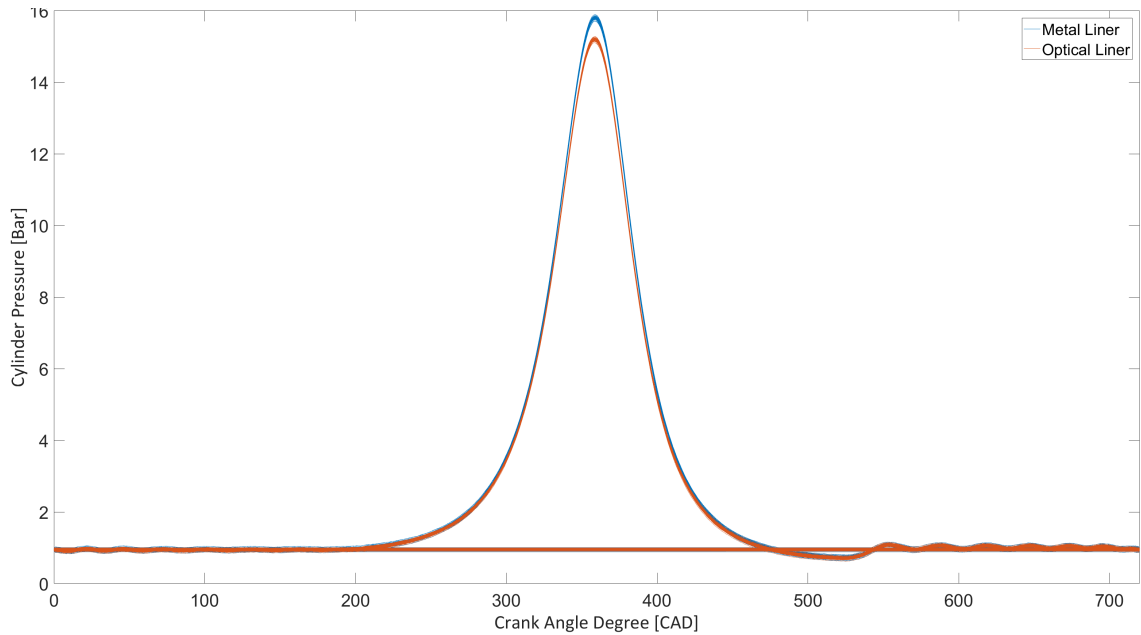

Figure 5.3: In-cylinder pressure time histories for the motoring conditions listed in Table 5.1 using the metal and optical cylinder liners.

5.3.2 Fuel spray imaging

Typical imaging data of the fuel spray development from the frontview are presented in Figure 5.4 for a start of injection (SOI) timing of 90° bTDC an injection duration of 0.25 ms, and fuel injection pressure $P_{inj} = 100$ bar. The injection event represented approximately 1.25 grams of fuel injected. The images in Figure 5.4 were

false colored to highlight the spray features. A sharpening filter was applied and other image settings were adjusted for presentation clarity. The images show excellent separation between the spray plumes. The sprays developed with little spread to the spray cone angle as a function of time, until impingement of the spray on the cylinder liner is observed later in the imaging sequence ($\sim 86.5°$ bTDC).

CAD = 90.0° bTDC

CAD = 89.8° bTDC

CAD = 89.6° bTDC

CAD = 89.4° bTDC

CAD = 89.2° bTDC

CAD = 89.0° bTDC

CAD = 88.8° bTDC

CAD = 88.6° bTDC

CAD = 88.4° bTDC

CAD = 88.2° bTDC

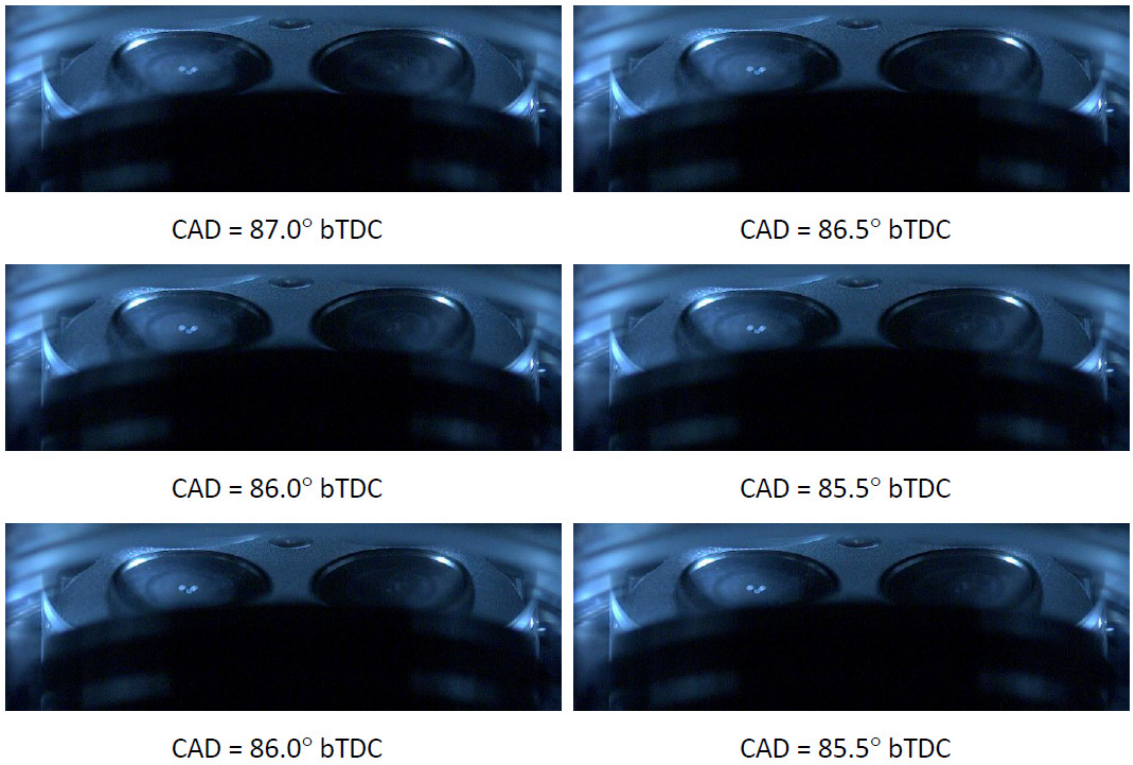CAD = 88.0° bTDC

CAD = 87.5° bTDC

Figure 5.4: Imaging sequence of fuel injection for SOI of 90° bTDC and an injection duration of 0.25 ms.

The imaging data were analyzed to determine the penetration distance of the tip of the two fuel spray plumes (d_1 of the left plume and d_2 of the right plume), injection speed, plume cone angle, and plume to plume spray angle as a function of time. The results for penetration distance are presented in Figure 5.5 and qualitatively indicate the fuel spray develop symmetrically. The measured penetration length was estimated as biased by approximately $\pm$ 4% due to the 16° off-axis camera position. For the image analysis the origin was set at the nozzle exit for each spray. The piston obstructed the camera view of the full spray plumes at 631.3 CAD. The injection spray tip velocities were determined to be 75 ± 5 m/sec for both spray plumes. From the imaging data, the spray angle between the central axes of the two spray plumes was $126° \pm 4°$, and the spray cone angles were $d_1 = 7.5° \pm 2.0°$ and $d_2 = 9.5° \pm 2.0°$. The separation angle from the imaging is within 10% of the Delphi characterization using the spray chamber and n-heptane fuel.
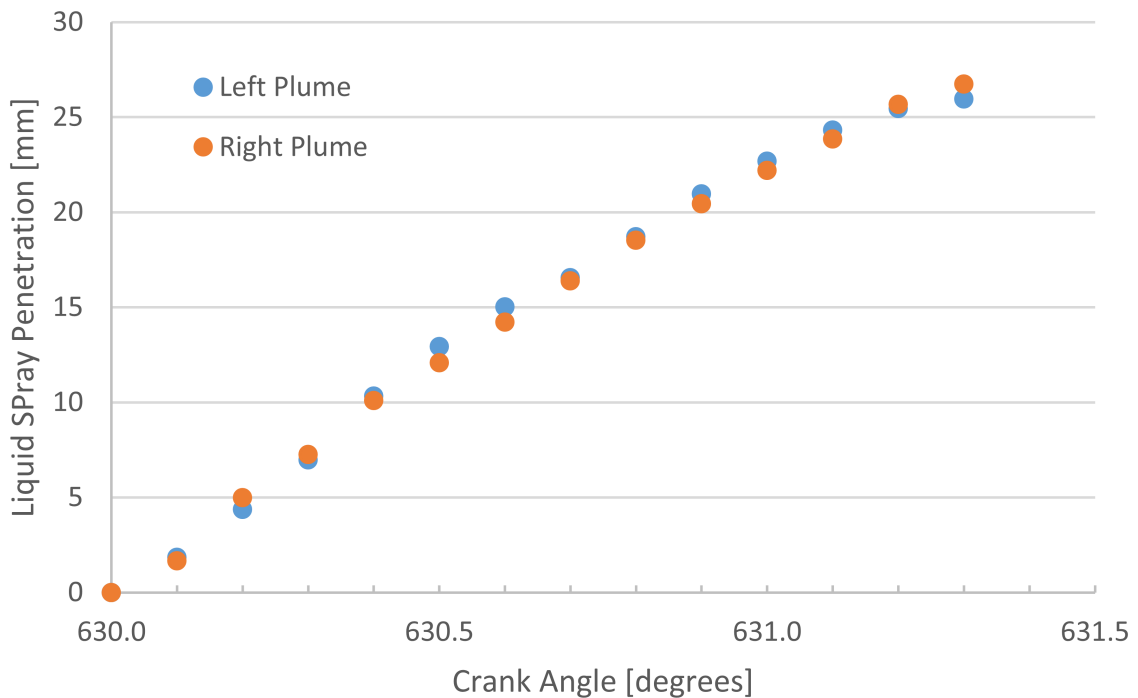

Figure 5.5: Penetration distances of the two fuel sprays presented in the imaging sequence of Figure 5.4 for SOI of 90° bTDC and an injection duration of 0.25 ms.

Figure 5.7 presents spray imaging results for SOI $= 75°$ bTDC, injection duration of 1 ms, and $P_{inj} = 100$ bar. This injection event represented approximately 4.41 milligrams of fuel injected. The images have not been corrected for off-axis viewing, but they have been enhanced for clarity. At the more retarded injection timing, the fuel sprays again show excellent separation, and little change in the spray cone angles
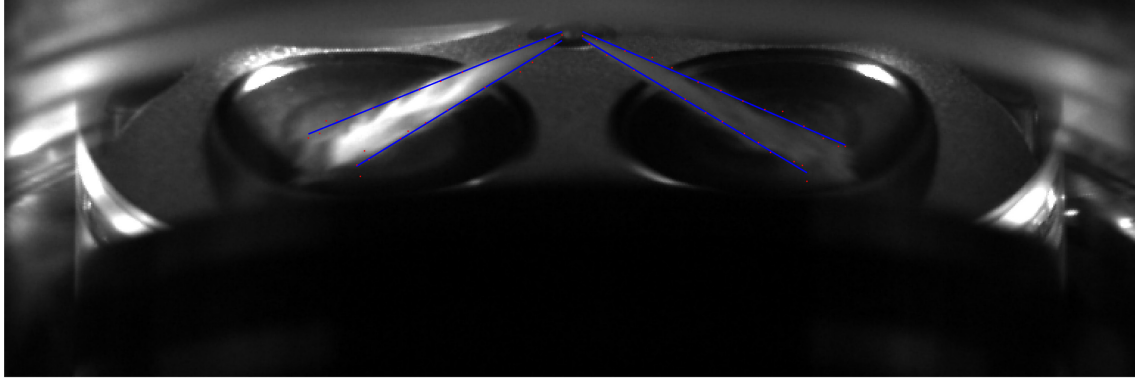
Figure 5.6: Detailed imagine processing alogrithm is used to determine the plume cone angles and plume to plume spray angles for spray pattern presented in Figure 5.4.

as the spray developed. Due to the later injection timing and the longer fuel injection duration, the piston occludes the spray interaction with the cylinder walls. However, the piston obstructed the camera view of the full spray plumes at 646.2 CAD.

The spray penetration distance corresponding to the imaging data of Figure 5.7 are presented in Figure 5.8 and qualitatively indicate the fuel sprays develop symmetrically. As with the earlier injection timing, the results show excellent symmetry between the two plumes. The measured penetration length was estimated as biased by approximately $\pm$ 4% due to the same 16° off-axis camera position. The imaging data were also analyzed to determine the penetration distance of the tip of the two fuel spray plumes (d_1 of the left plume and d_2 of the right plume), injection speed, plume cone angle, and plume to plume spray angle as a function of time. For the image analysis portion, the origin was set at the nozzle exit for each spray. The injection spray tip velocities were determined to be $d_1 = 67 \pm 5$ m/sec and $d_2 = 70 \pm 5$ m/sec for the respective spray plumes. From the imaging data, the spray angle between the central axes of the two spray plumes was 128° $\pm$ 4°, and the spray cone angles were $d_1 = 7.1° \pm 2.0°$ and $d_2 = 6.8° \pm 2.0°$. The separation angle from the imaging is once again within 10% of the Delphi characterization using the spray chamber and n-heptane fuel.

The experimental results for the fuel spray imaging are in good qualitative agreement with the CFD results for the spray development. For example, Figure 5.10 presents the simulation predictions for equivalence ratio (where high ϕ indicates high concentrations of fuel) for a higher engine speed condition of 2000 RPM with a higher fuel injection pressure Pinj $= 150$ bar compared with the experimental engine conditions. However, the fuel mass used in the CFD simulation (4 mg) was similar to

the experimental conditions of Figure 5.7. The SOI for the CFD simulation was 60° bTDC; more retarded by 15° compared with the experimental data of Figure 5.7 which used SOI = 75° bTDC. The CFD results showed two distinct sprays which developed and impinged on the cylinder liner walls where the piston motion induced flow along the line wall and into the pre-chambers, as observed in the imaging experiments. Figure 5.11 presents CFD simulation results for the same conditions as Figure 5.10, however, with a higher injected fuel mass of 7 mg. As expected, the higher fuel mass extends the duration of the fuel spray event in the simulation results. The penetration distances for the two CFD simulations are presented in Figure 5.12 and Figure 5.13. As observed experimentally, the two sprays in the CFD simulations develop symmetrically. Comparison of the absolute values of the penetration distances showed the same order of magnitude for the spray development, but with faster penetration rates observed in the physical experiments at early times. Both the physical and computational experiments showed a change in the rate of penetration; however, the experiments exhibited slower penetration rate at later times, which was the opposite trend predicted by the CFD simulations. The decrease in the penetration rate is consistent with expectations based on other fuel spray studies documented in the literature. The differences in the penetration rates of the CFD and physical experiments may be due to differences in the operating conditions, engine geometry or assumptions used in the spray model; however, the bulk behavior is in good agreement.
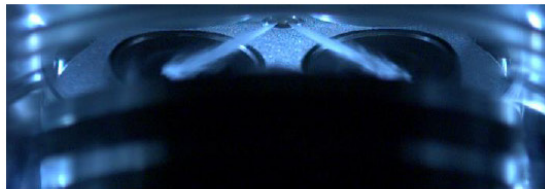
CAD = 75.0° bTDC

CAD = 74.7° bTDC

CAD = 74.4° bTDC

CAD = 74.1° bTDC

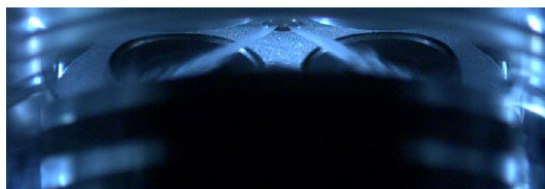CAD = 73.8° bTDC

CAD = 73.5° bTDC

CAD = 73.2° bTDC

CAD = 72.9° bTDC

CAD = 72.6° bTDC

CAD = 72.3° bTDC
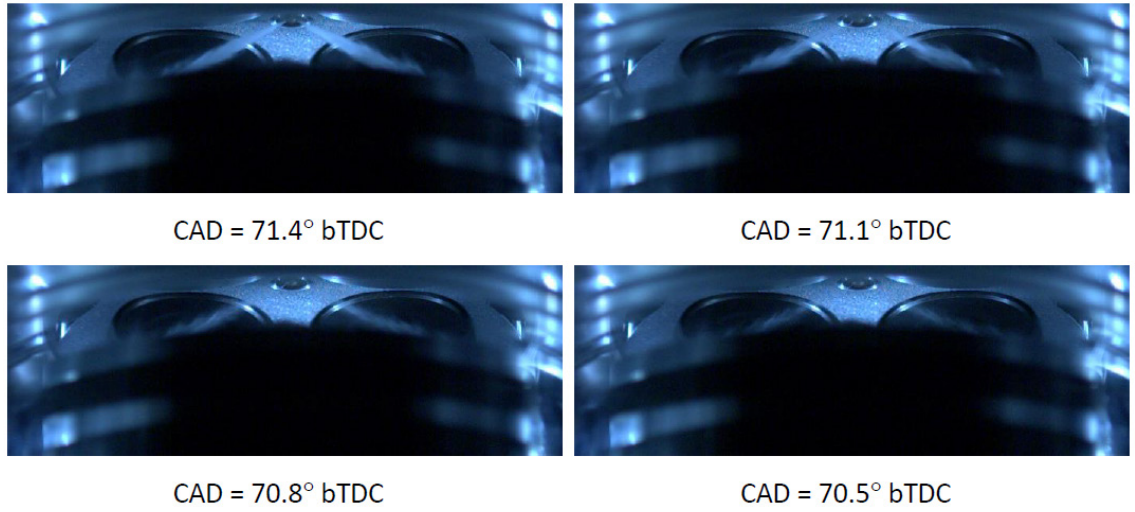
CAD = 72.0° bTDC

CAD = 71.7° bTDC

Figure 5.7: Imaging sequence of fuel injection for SOI of 75° bTDC and an injection duration of 1 ms
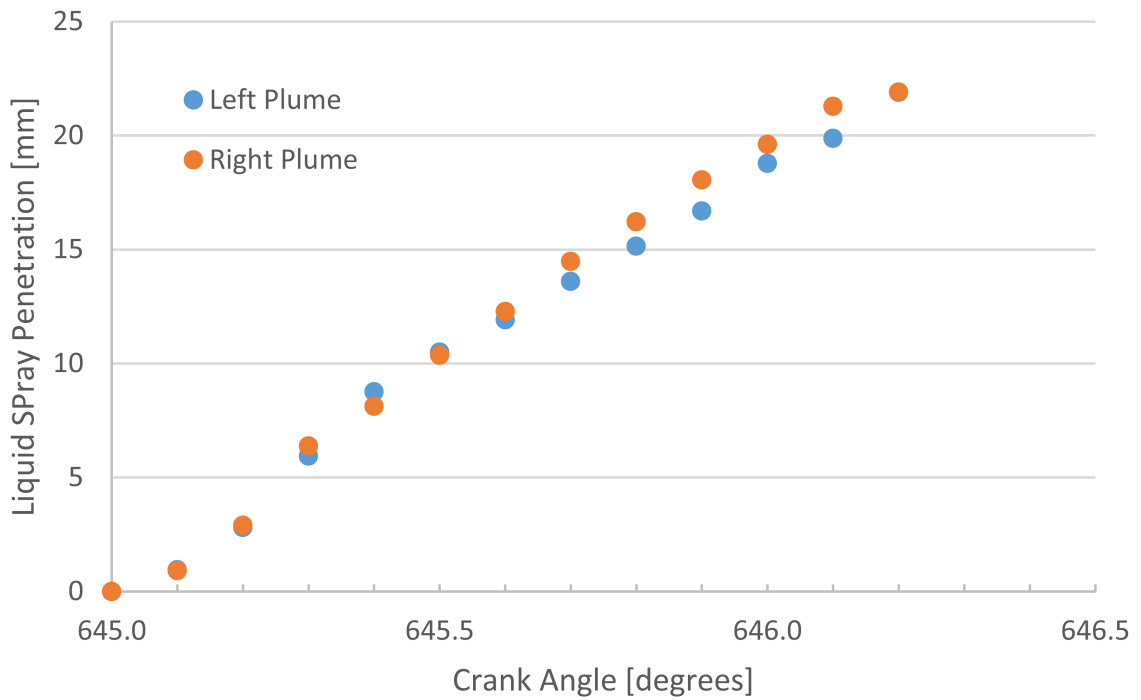

Figure 5.8: Penetration distances of the two fuel sprays presented in the imaging sequence of Figure 5.7 for SOI of 75° bTDC and an injection duration of 1 ms.
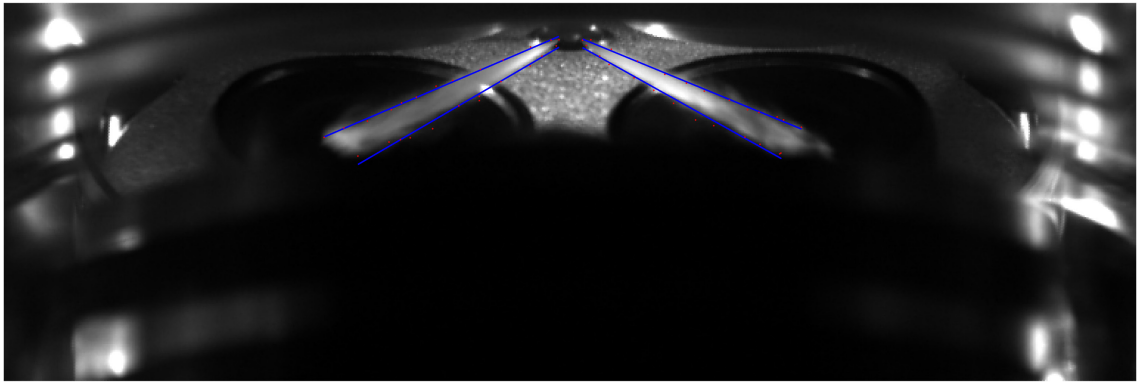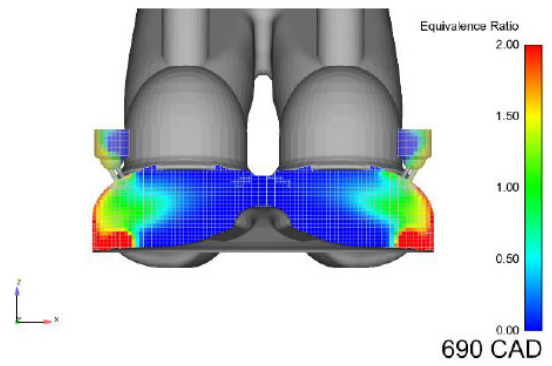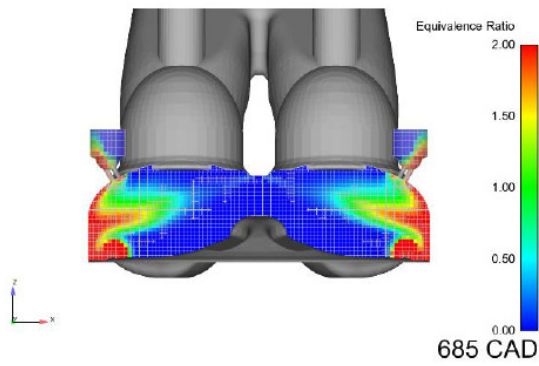
Figure 5.9: Detailed imagine processing algorithm is used to determine the plume cone angles and plume to plume spray angles for spray pattern presented in Figure 5.7.

655 CAD

660 CAD

665 CAD

670 CAD

675 CAD

680 CAD

685 CAD

690 CAD

100
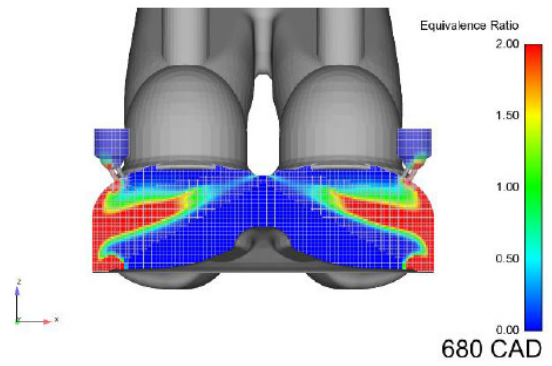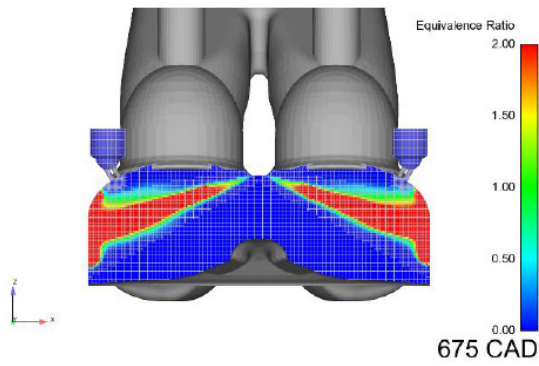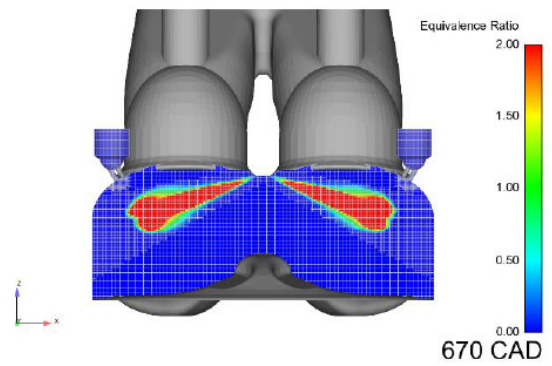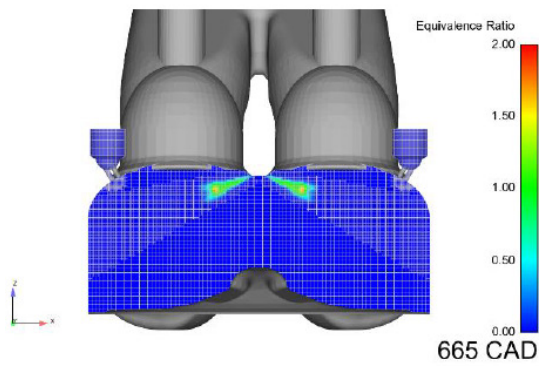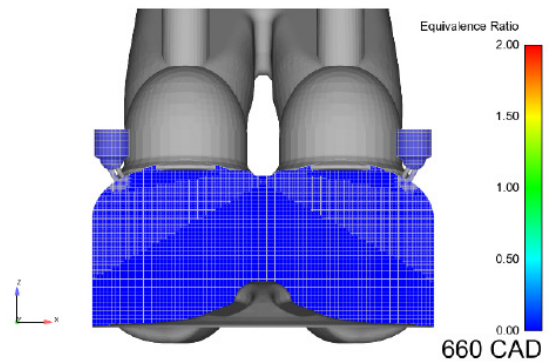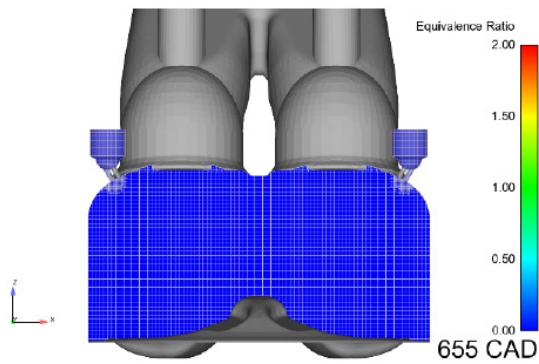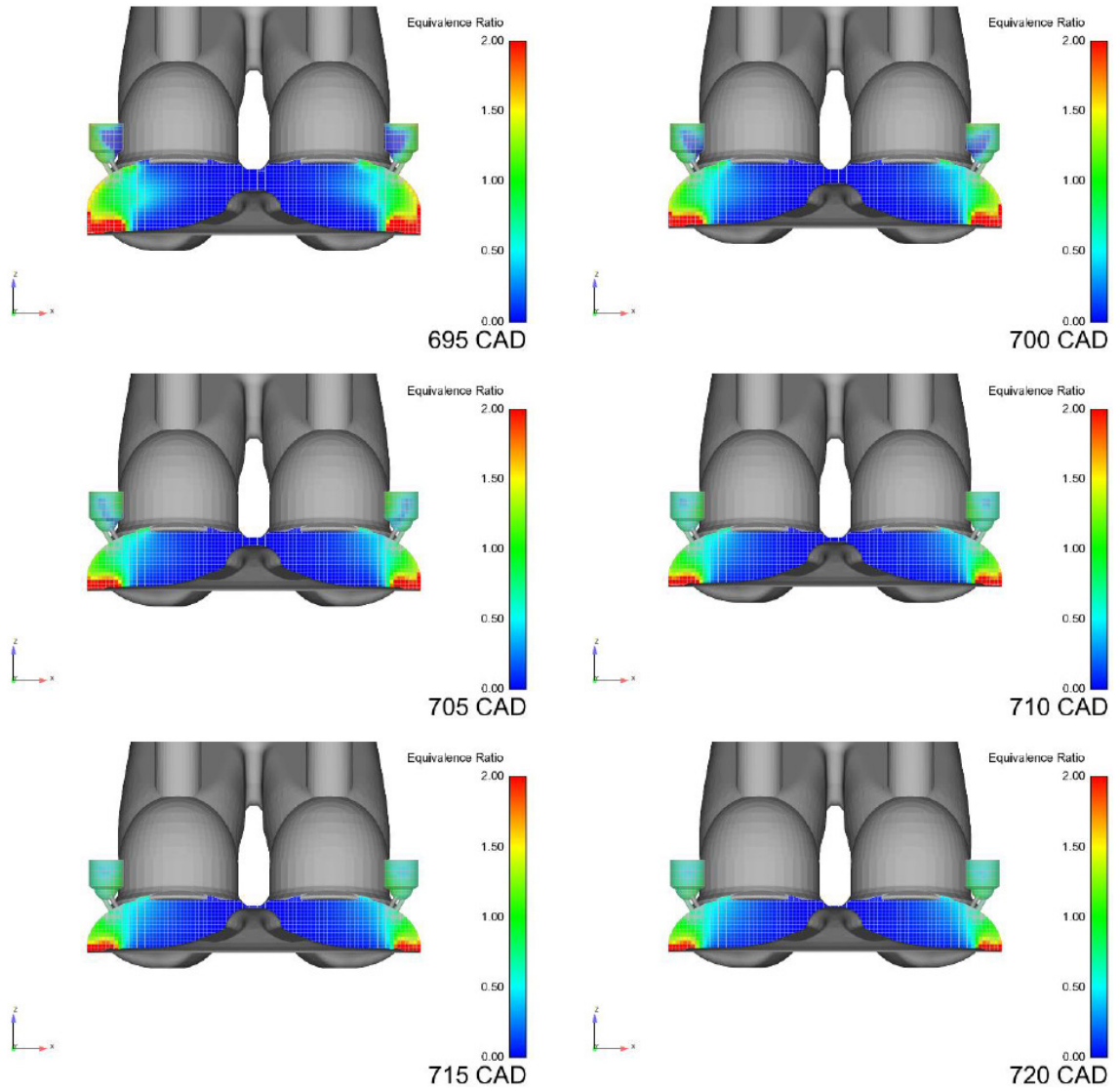
Figure 5.10: CFD results for equivalence ratio for conditions of 2000 RPM, 4 mg of fuel, $P_{inj} = 150$ bar, SOI = 60° bTDC (660 CAD).

655 CAD

660 CAD

665 CAD

670 CAD

675 CAD

680 CAD

685 CAD

690 CAD

102
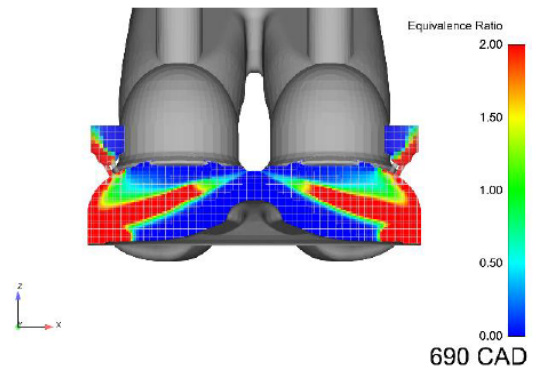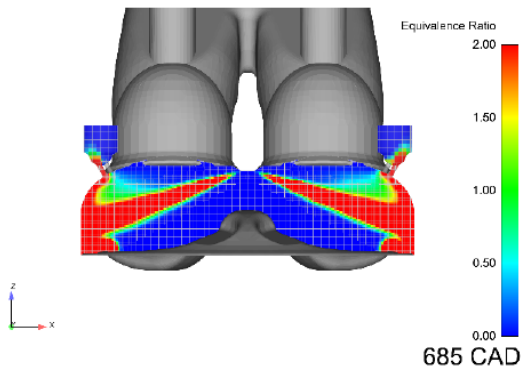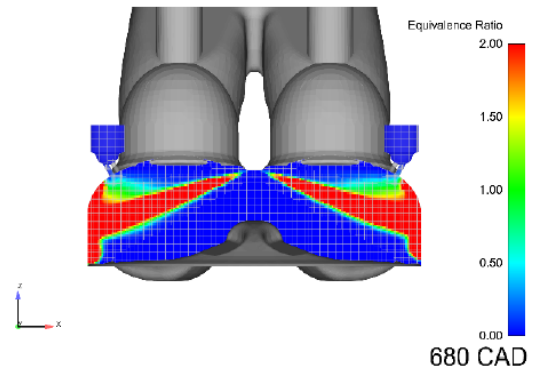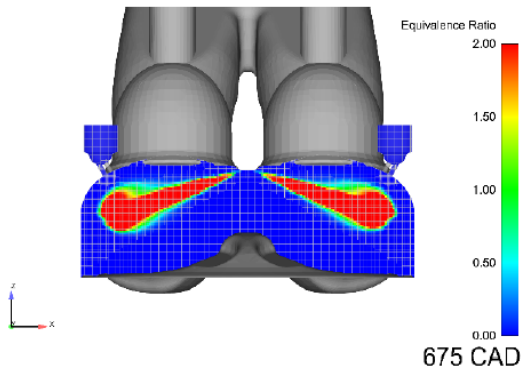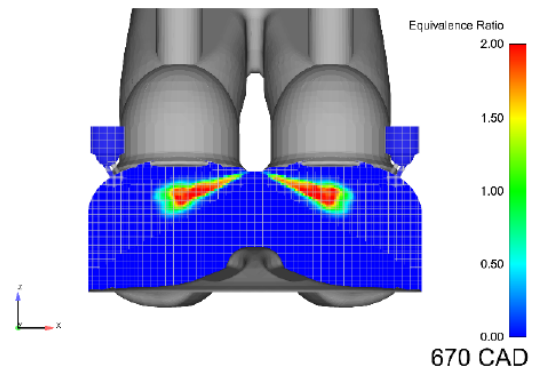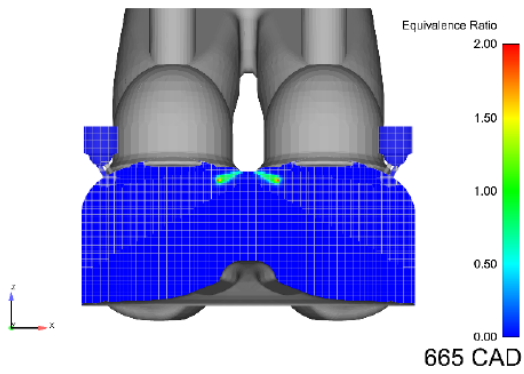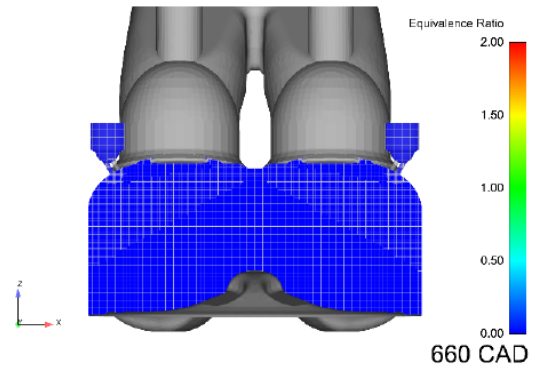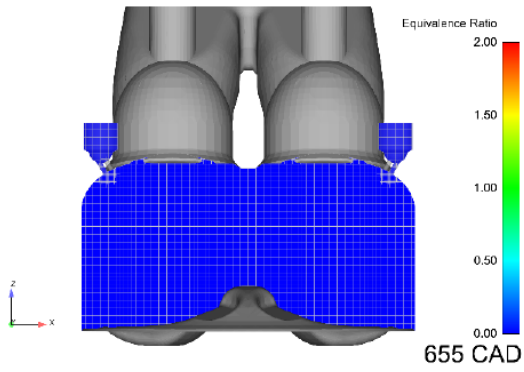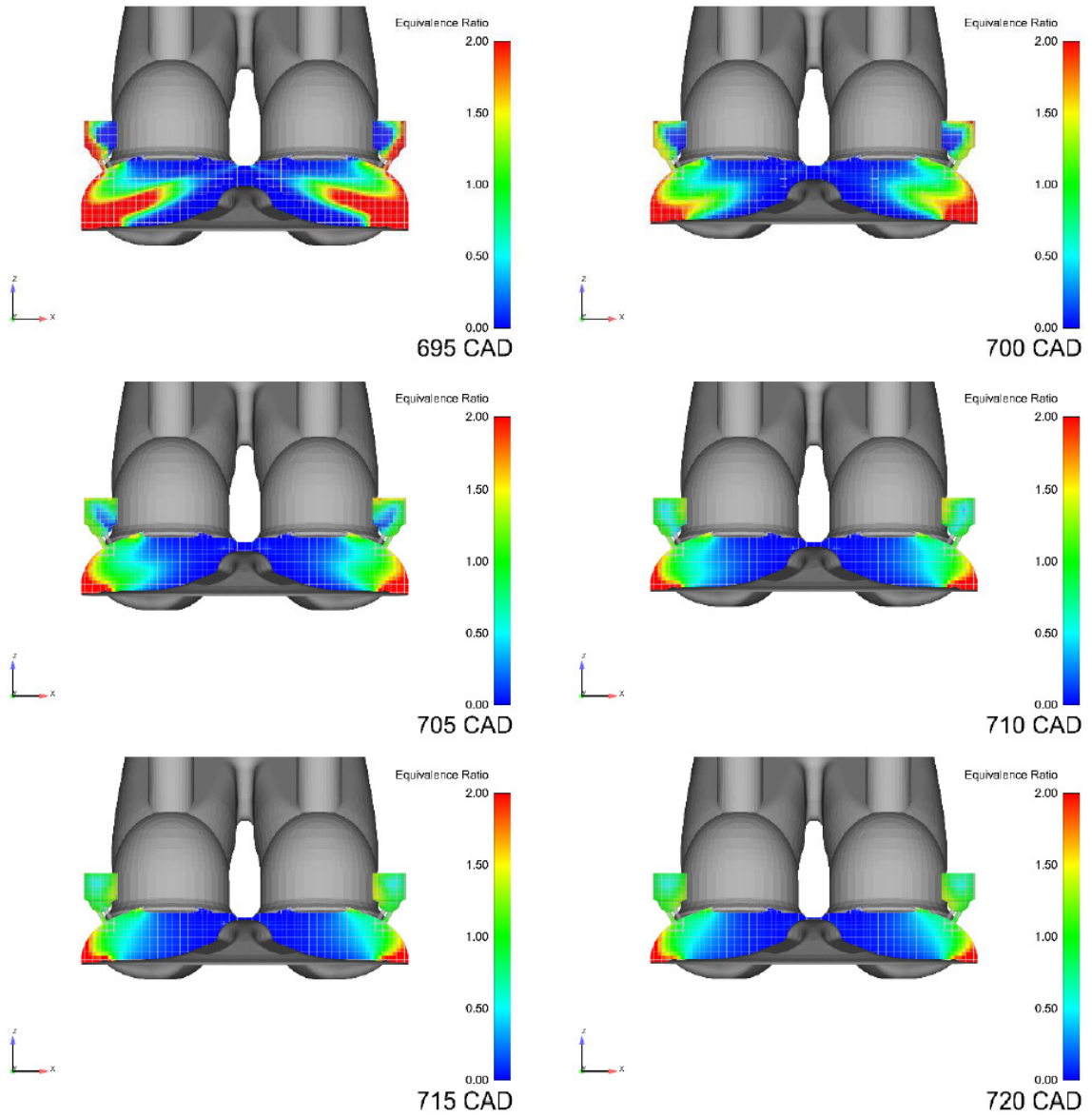
Figure 5.11: CFD results for equivalence ratio for conditions of 2000 RPM, 7 mg of fuel, P_{inj} = 150 bar, SOI = 60° bTDC (660 CAD).
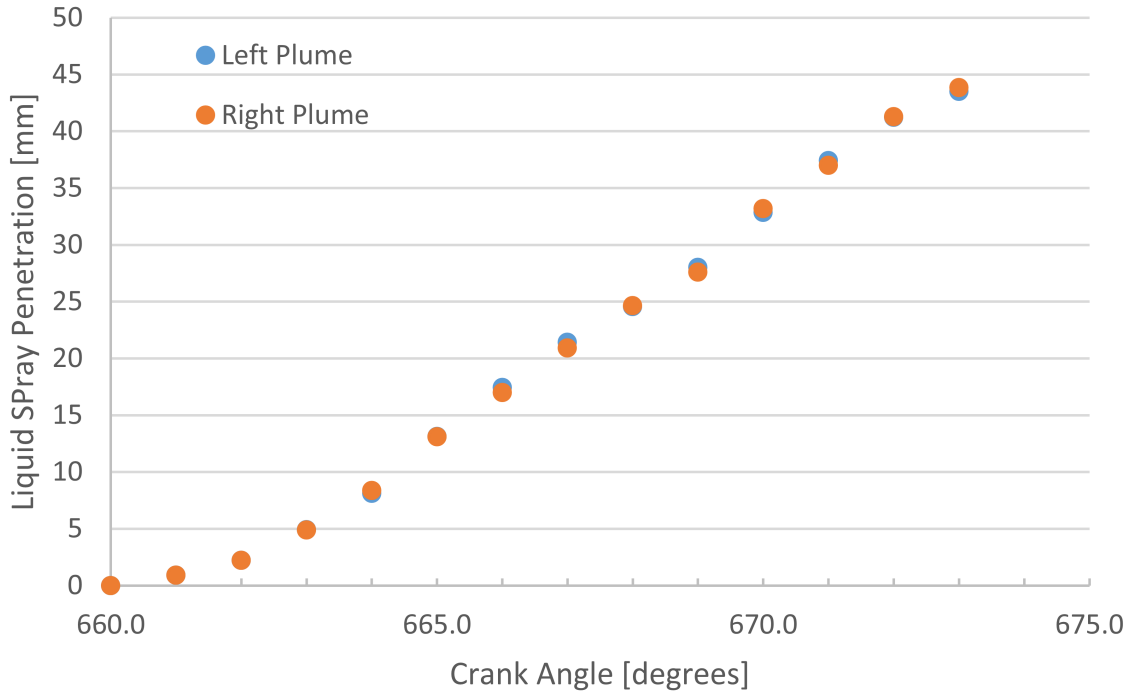
Figure 5.12: Penetration distance measurements for CFD results for conditions of 2000 RPM, 4 mg of fuel, $P_{inj} = 150$ bar, SOI = 60° bTDC. These measurements correspond to Figure 5.10.
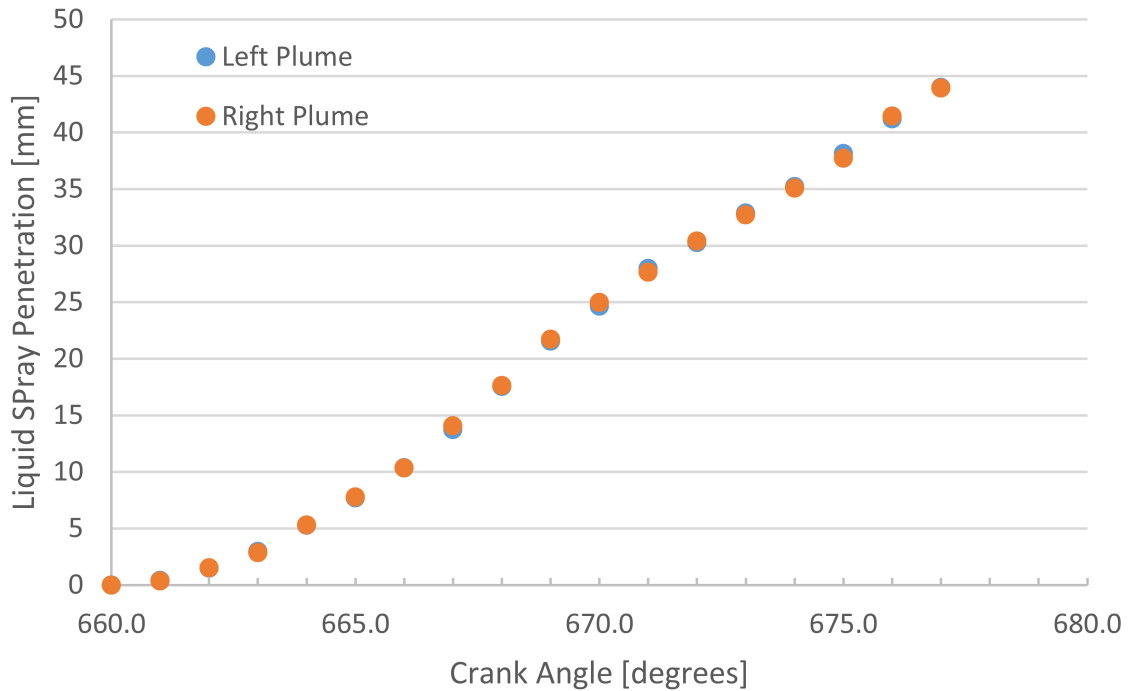
Figure 5.13: Penetration distance measurements for CFD results for conditions of 2000 RPM, 7 mg of fuel, $P_{inj} = 150$ bar, SOI = 60° bTDC. These measurements correspond to Figure 5.11.

5.3.3　Air flow imaging

The air used in the engine studies was not dried prior to use, and consequently the water moisture naturally present in the air provided the basis to image the flow field as water condensed in the bulk charge of the fuel/air mixture. Figure 5.14 presents results of imaging the water condensation and subsequent flow motion of the water droplets. Unfortunately, this type of *in situ* particle seeding for flow imaging was only available for a portion of the cycle as the water droplets evaporated during compression heating. The contrast in the images is low, making the flow direction difficult to see, but the images indicate vortices developing off the surface of the piston. In comparison, Figure 5.15 shows the CFD predictions for the tangential projection of the velocity vector field at the piston centerline at 2000 RPM. The vector field shows the split reverse tumble motion developed in the flow, as well as the strong pre-chamber inflow and outflow flow field patterns.

CAD = 25° aTDC

CAD = 30° aTDC

CAD = 35° aTDC

CAD = 40° aTDC

CAD = 45° aTDC

CAD = 50° aTDC
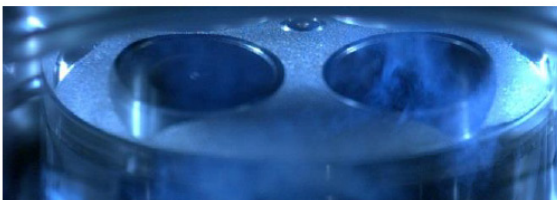
CAD = 55° aTDC

CAD = 60° aTDC

CAD = 55° aTDC

CAD = 60° aTDC

CAD = 65° aTDC
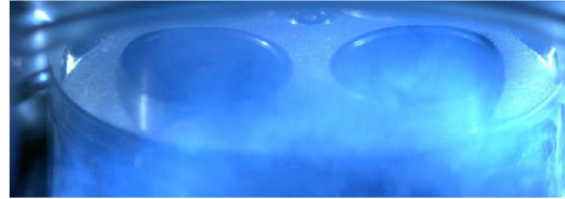
CAD = 70° aTDC

CAD = 75° aTDC

CAD = 80° aTDC

CAD = 85° aTDC

CAD = 90° aTDC

CAD = 95° aTDC

CAD = 100° aTDC

CAD = 105° aTDC

CAD = 110° aTDC

CAD = 115° aTDC

CAD = 120° aTDC

CAD = 125° aTDC

CAD = 130° aTDC

CAD = 135° aTDC

CAD = 140° aTDC

CAD = 145° aTDC

CAD = 150° aTDC

CAD = 155° aTDC

CAD = 160° aTDC
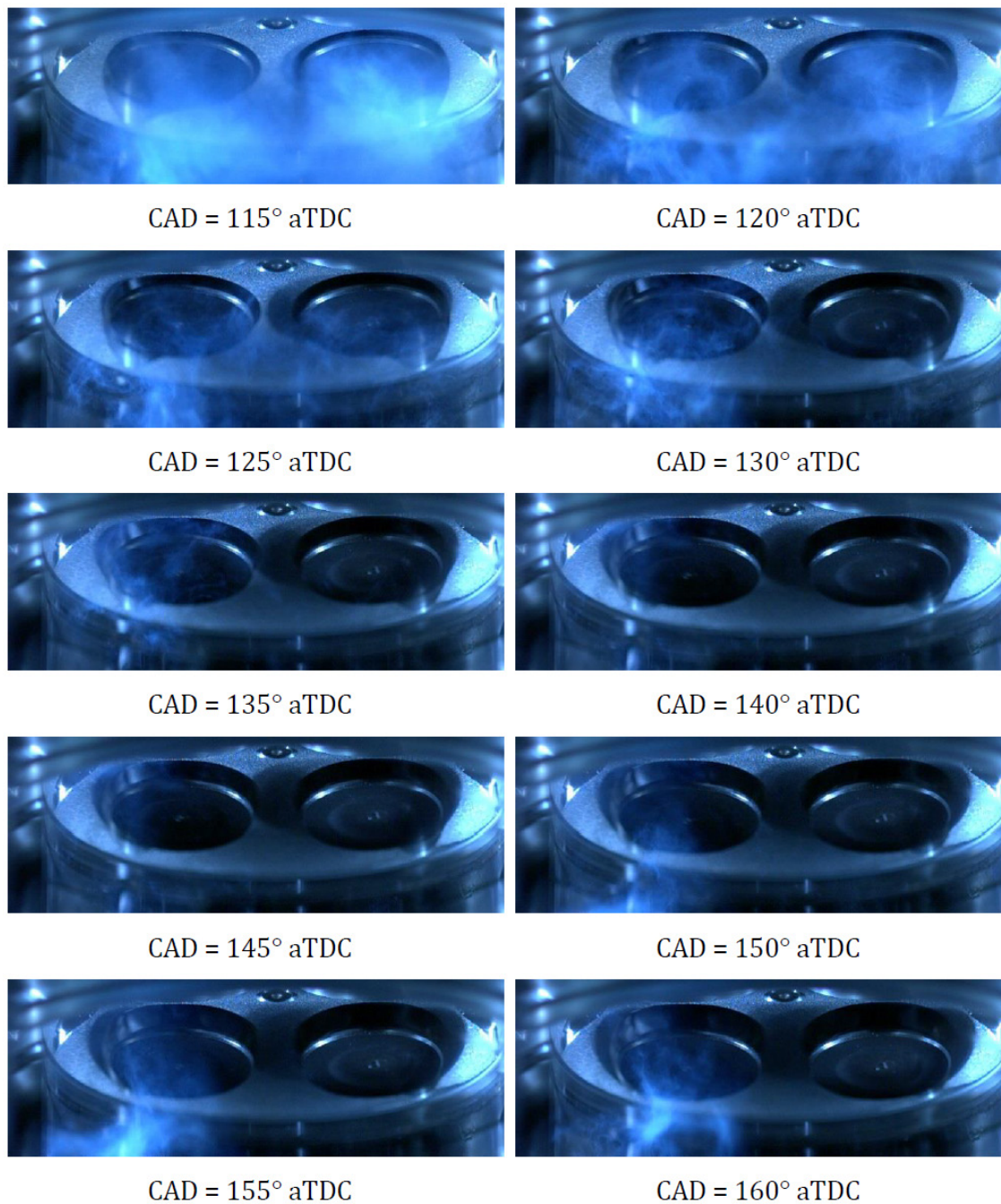
Figure 5.14: Imaging results of water condensation during expansion cooling of the air charge and subsequent water droplet motion. The imaging sequence is from the expansion stroke of the fuel injection cycle with SOI of 45° bTDC and an injection duration of 1 ms.

590 CAD

600 CAD

610 CAD

620 CAD

630 CAD

640 CAD

109

650 CAD

660 CAD

670 CAD

680 CAD

690 CAD

700 CAD

110

710 CAD

720 CAD

730 CAD

740 CAD

750 CAD

760 CAD
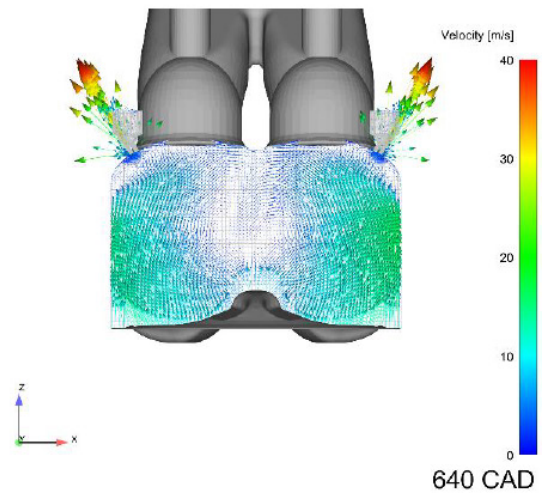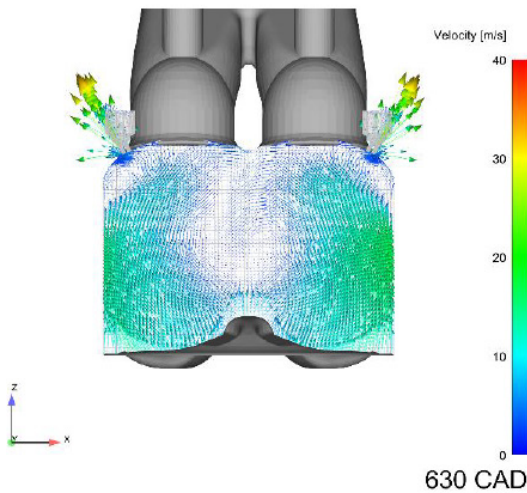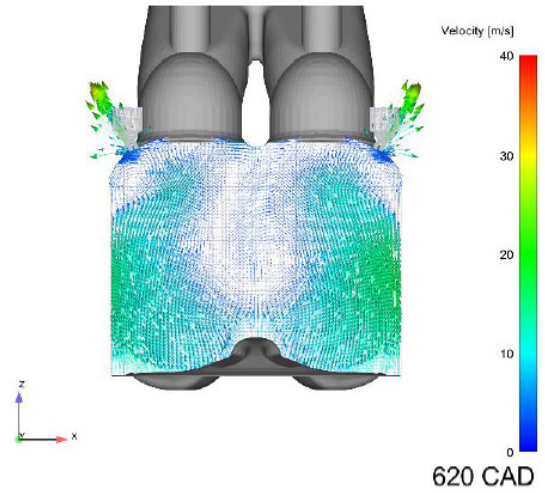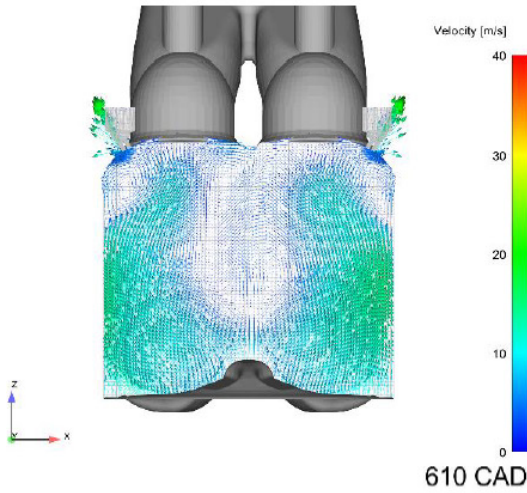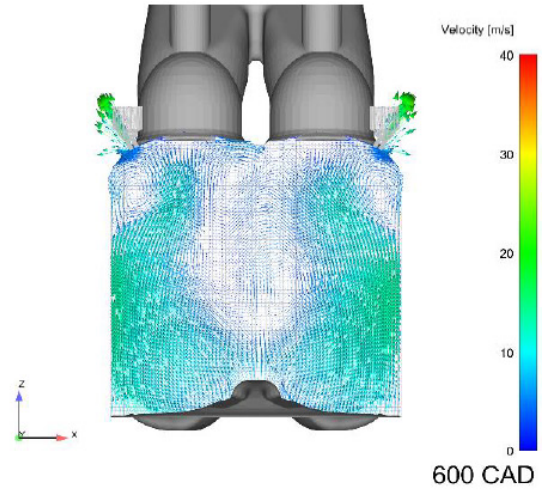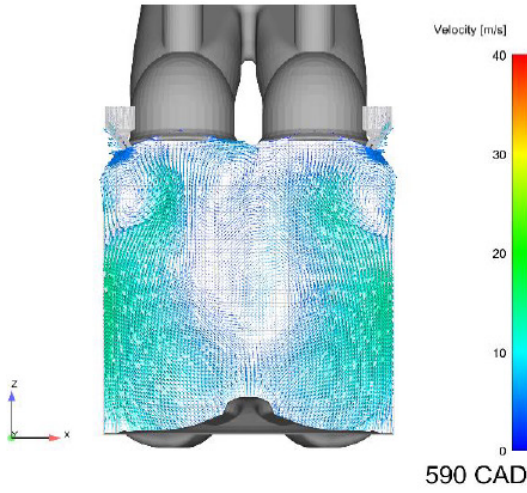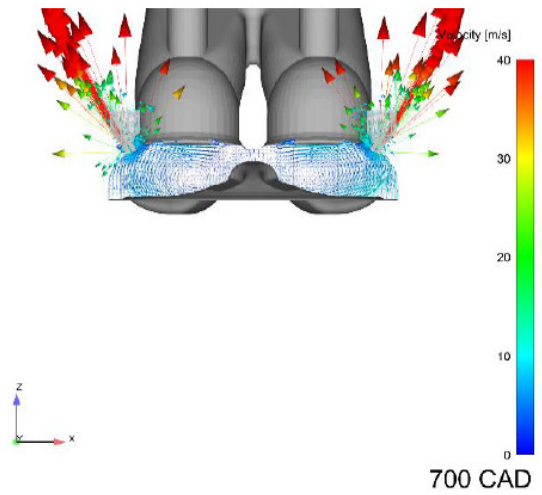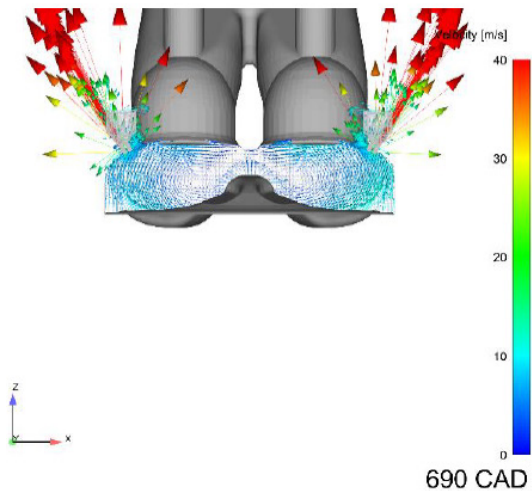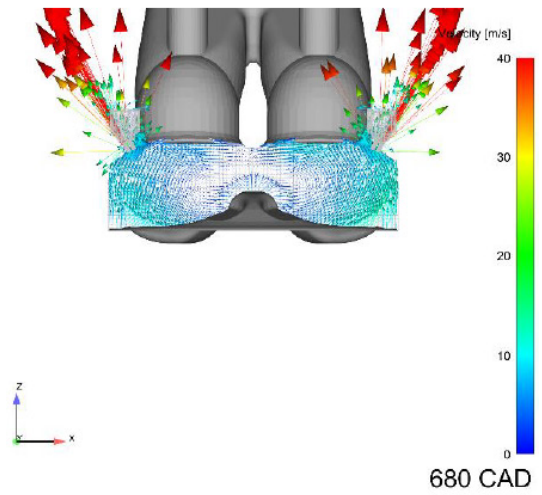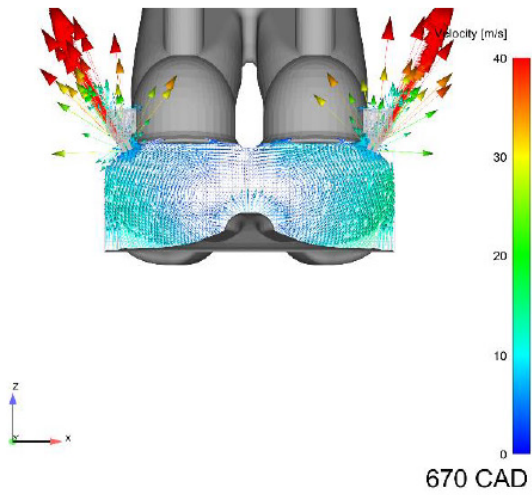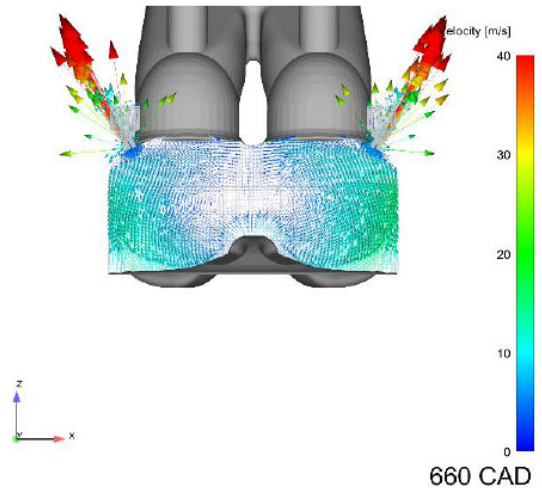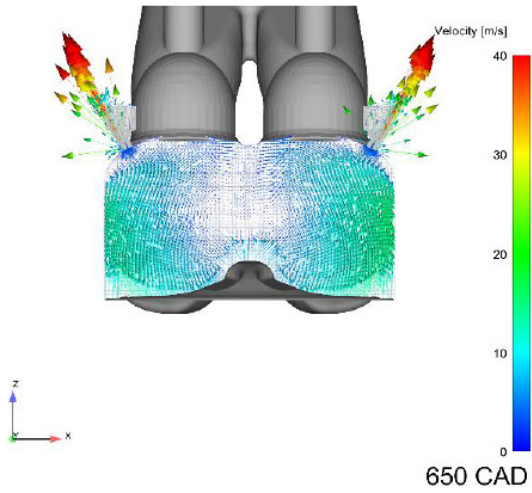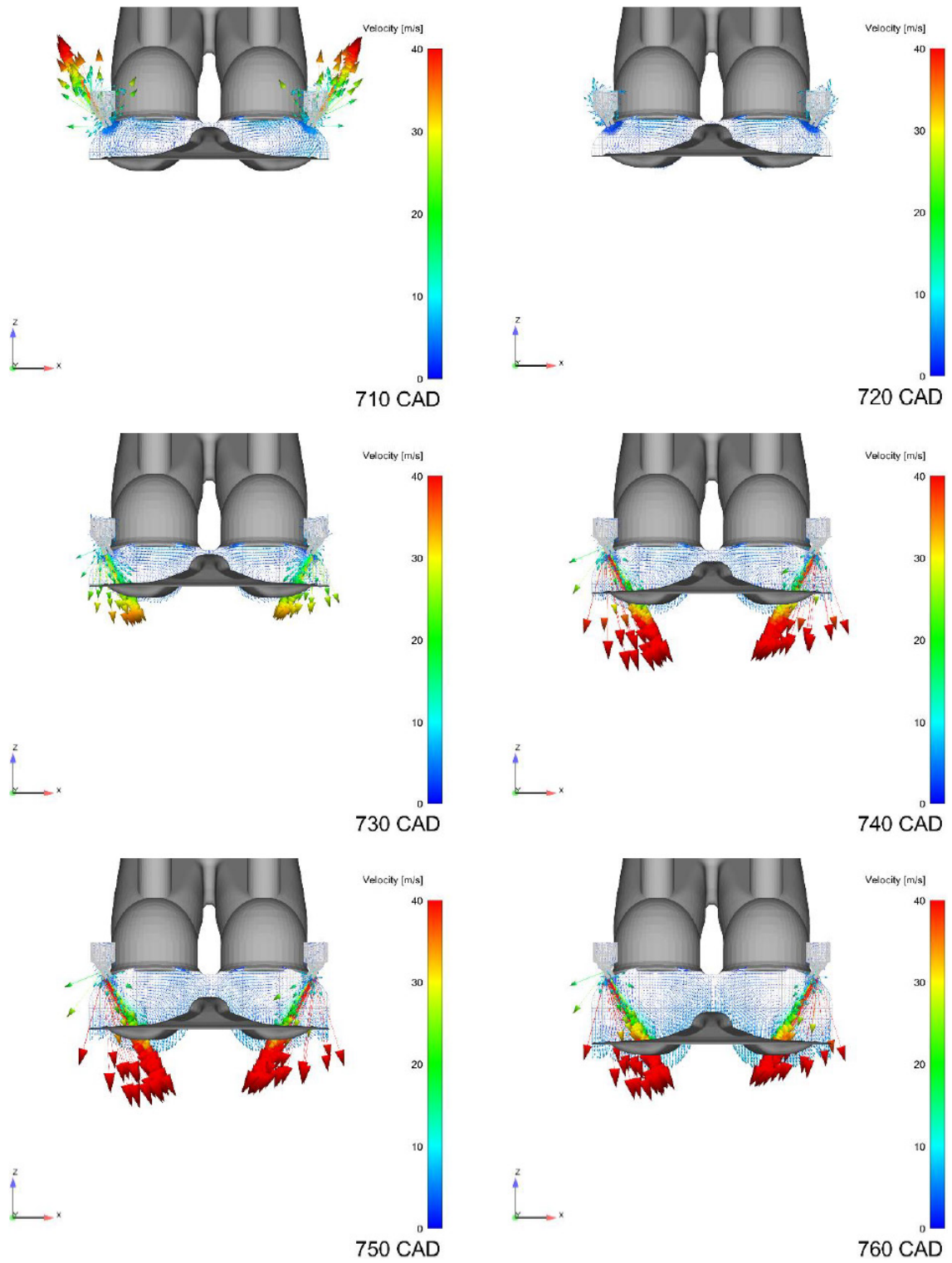
Figure 5.15: Converge simulation results for air charge motion of the Zeta Prototype for conditions of 2000 RPM.

5.4 Summary and Conclusions

The tests using the metal hardware of the DPC Zeta prototype showed good integrity for valve events, piston motion, and oil, coolant, fuel, and air flows. A fully transparent fused silica cylinder liner was fabricated for imaging studies of the fuel and air flow. High-speed imaging captured fuel injection events at different injection timings and the air charge motion (via droplet condensation).

The fuel injection imaging showed two narrow opposed fuel sprays were developed which targeted the walls of the combustion chamber. The performance of the fuel injector was in excellent qualitative agreement with the CFD predictions and with the quantitative calibration testing results provided by Delphi. Fuel penetration distance, injection speed, plume cone angle, and plume to plume spray angle were measured as a function of different operating conditions. The fuel spray data are the first *in situ* measurements of the unique fueling strategy and unique hardware.

The air charge imaging also confirmed vortices were developed near the surface of the piston, consistent with the CFD simulations. These vortices are critical in forming the split reverse tumble motion that guides the bulk charge motion in the main chamber. Additionally, the air charge imaging verified there was a significant outflow of charge mass from the pre-chambers into the main combustion chamber during the expansion stroke. The observation of air charge mass outflow of the pre-chambers eliminates the possibility of a recirculation zone existing near the pre-chamber orifices that would prevent air charge from being inducted into the pre-chambers during the compression stroke. The features of the fuel and air flow were considered vital based on the CFD results to passively fuel the pre-chambers. Given the good agreement with the CFD predictions, the air charge flow combined with the fuel flow of the physical engine is indeed expected to create the targeted stoichiometric charges in the pre-chambers.

CHAPTER VI

Conclusions and Recommendations for Future Work

6.1 Conclusions

The dramatic advances in digital computing has radically changed the process of engine research and development; significantly reducing the time from concept to reality. In this thesis, fundamental experiments, computational studies and experimental validation techniques have successfully guided the development of new engine hardware targeted to enable fuel lean, high-efficiency reciprocating engines. The following are the key conclusions and outcomes of this thesis.

- The effects of flame propagation accelerated the autoignition ignition delay time of premixed iso-octane and air by $2 - 31\%$ at $P_{EOC} = 7.8 - 9.5$ atm and T_{EOC} $= 942 - 1018$ K. Propagation rates of flames successfully initiated by the spark plasma ranged from $\sim 1 - 12$ m/sec at these state conditions. Dilution had a significant effect on the lean flammability limits, increasing the lean limit of ϕ $= 0.35$ at air levels of dilution to $\phi = 0.65$ at inert:O_2 dilution of 7.5. These data were the first of their kind to quantify the effects of flame propagation on autoignition at conditions relevant to end-of-compression conditions found in SI engines.

- A combustion system was successfully designed which CFD simulations predicted would simultaneously achieve near stoichiometric ($\phi \sim 1.0$) fuel-to-air equivalence ratios in two pre-chambers with lean equivalence ratios ($0.4 < \phi <$ 1.0) in the main combustion chamber. Model predictions showed good flexibility in fuel injection strategies (e.g. injection timing and fuel mass) in terms of achieving passive fueling of the pre-chambers. This part of the thesis research

demonstrated the first combustion chamber design of such a superposition of fuel strategies using pre-chambers.

- A flow alignment metric was developed based on the flow field near the pre-chamber orifices to quantify the contribution of the local flow to filling and emptying the pre-chamber. The metric was applied to understand the transient nature of the pre-chamber filling dynamics. Regardless of combustion chamber geometry, number of orifices, or pre-chamber location, optimal pre-chamber injection strategies will introduce the appropriate amount of vaporized fuel near the pre-chamber orifices at a time when the flow field near the orifice is well aligned with the normal vector of the orifice opening.

- A single-cylinder optically-accessible engine prototype was designed and manufactured to validate the CFD model predictions. The prototype engine showed good integrity for valve events, piston motion, and oil, coolant, fuel, and air flows. Fuel injection was in excellent qualitative agreement with the CFD predictions and with the quantitative calibration testing results provided by the manufacturer of the fuel injector. Fuel penetration distance, injection speed, plume cone angle, and plume-to-plume spray angle were measured as a function of different operating conditions. The fuel spray data were the first in situ measurements of the unique fueling strategy proposed for passive fueling of the pre-chamber.

- The air charge imaging confirmed vortices, critical in forming the split reverse tumble motion that guides the bulk charge motion in the main chamber, were developed near the surface of the piston, consistent with the CFD simulations. Additionally, the air charge imaging verified there was a significant outflow of charge mass from the pre-chambers into the main combustion chamber during the expansion stroke. The imaging results eliminated concerns of a recirculation zone forming near the pre-chamber orifices that could prevent the air charge from being inducted into the pre-chambers during the compression stroke.

- The features of the fuel and air flows were considered vital based on the CFD results to passively fuel the pre-chambers. Given the good agreement with the CFD predictions, the combustion chamber and fueling strategy are expected to create the targeted stoichiometric charges in the pre-chambers, while allowing the main chamber charge to be fuel lean.

6.2 Recommendations for Future Work

As stated by Albert Einstein, "The more I learn, the more I realize how much I don't know." The culmination of this thesis has demonstrated the feasibility of a novel SI engine strategy featuring a pair of passively fueled pre-chambers that can be used to ignite a leaner and more dilute main chamber charge. The clear and obvious immediate next step is to perform firing experiments to demonstrate the lean and dilute operating limits of this pre-chamber engine concept. With any new engine concept, the first critical milestones are to demonstrate a thermal efficiency benefit and reduced engine-out emissions. Often, these targets are set based on the understanding that exhaust after-treatment may be necessary to meet emissions regulations. Durability testing is also required. Throughout these steps, optimization studies would consider geometrical aspects such as the pre-chamber volume and pre-chamber connecting orifices as well as engine control aspects.

In addition to the immediate next steps for the engine concept stated above, there are a number of exciting opportunities that should be further explored both in the experimental and computational domains. Figure 6.1 briefly outlines the future areas to be explored for each of the three type of studies performed in this work. Starting from the fundamental studies, the same experimental approach can now be extended to further study lean flammability limits in the context of other fuels such as ethanol, new ignition energy sources, end-gas knock, and even higher pressure conditions that are increasingly more relevant given the trend of downsizing engine displacement and boosting. An additional area of future work is to investigate the mechanism(s) by which jet ignition affects the main-chamber combustion. Pre-chamber ejected products are described as high enthalpy flows and/or jets of highly reactive intermediate combustion species. Further work can focus on understanding whether the fundamental mechanism of jet ignition is due to thermal or chemical effects or a combination of both.

In regards to the computational studies, future work should focus on improving the ability to handle increased computational loads. This can happen through two means: advances in the physical computer hardware as well as developing faster algorithm using numerical methods to create more efficient solvers. With the extra computational capacity, one can now run larger computational domains, longer simulations, and/or include more detailed physical models. For example, the chemical kinetics that are used for in-cylinder combustion are presently highly reduced due to computational load limitations. By increasing the computational load handling

ability, detailed chemical kinetic mechanisms can be incorporated to better predict the in-cylinder combustion process.

Fundamental studies of fuel ignition characteristics	Computational Studies of in-cylinder flow development using a passively fueled pre-chamber	Single-cylinder optical engine studies
• Other Fuels • Ignition Energy Sources • Higher Pressures • End-gas knock • Pre-Chamber RCF speciation measurements	• Faster algorithms to enable simulation of full breathing • Integrate more fundamental fuel spray physics • Improved combustion models to include kinetics specific to pre-chambers	• Demonstrate sustained combustion using a passively fueled pre-chamber • Revise thermodynamic sweet spot based on new advances in combustion modes

Figure 6.1: Set-up for adjusting proper valve lash prior using lower camshaft carrier and conventional camshaft journal caps, prior to installing and sealing the upper camshaft carrier.

As a final thought, a lot of this work has been motivated by the looming 2025 corporate average fuel economy (CAFE mandate) and the need to explore viable new powertrains to meet this mandate. Improving the fuel efficiency of a vehicle's powertrain is undeniable a worthy task, but sometimes it is important to take a step back and look at the bigger picture. The CAFE standard was introduced as a way to curb the carbon dioxide emissions for the largest producing industry sector in the United States of America in response to an increasing global warming trend. Furthermore, it is important to note that the CAFE standard applies to new vehicles only. However, what does the fleet average fuel economy of all the vehicles on the United States roads look like? By examining Figure 6.2, the answer is $\sim$ 21 mpg compared to new vehicle average fuel economy of $\sim$ 36 mpg. If one is serious about curbing carbon dioxide production, it is not enough to set aggressive targets for new vehicles only. Over time the fleet average of $\sim$ 21 mpg will certainly increase through these mandates, but that will take many years given that approximately 15 – 20 million new cars per year are introduced into a fleet of approximately 250 million aging cars. Thus, it is imperative to address the entire fleet average to curb carbon dioxide production. In addition to designing new revolutionary powertrains, we must also look at all possible options to increase the fleet average whether it be through consumer awareness, ride-sharing, or buy-back programs.
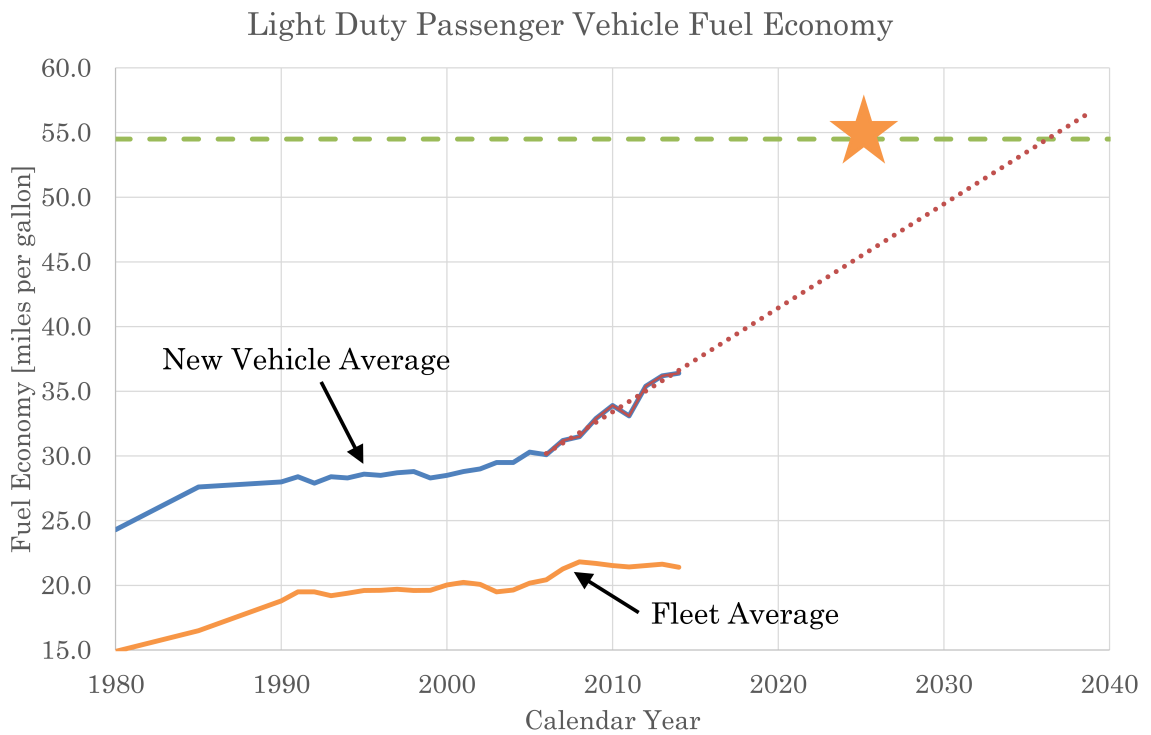
Figure 6.2: New light duty passenger vehicle fuel economy compared to fleet average with 2025 CAFE mandate highlighted. Data is sourced from the United States Department of Transportation [4].

APPENDICES

APPENDIX A

Supplemental Material for the Experimental Investigation of Flame Autoignition Interactions

Purity and source of the reactants used in the experiments are provided below:

- *iso*-octane, C_8H_{18}, (Sigma-Aldrich, 2,2,4-Trimethylpentane, anhydrous, $\geq 99.75\%$ purity, $\leq 0.003\%$ water), (Fisher Chemical, 2,2,4-Trimethylpentane, Optima™grade, 99.9% min by GC purity)

- Oxygen, O_2, (Cryogenic Gases, PurityPlus 4.3, 99.993% purity, ≤ 40 ppm argon, ≤ 3 ppm moisture, ≤ 10 ppm nitrogen, ≤ 0.5 ppm total hydrocarbons)

- Nitrogen, N_2 (Cryogenic Gases, PurityPlus 5.0, 99.999% purity, ≤ 2 ppm oxygen, ≤ 3 ppm moisture, ≤ 0.5 ppm total hydrocarbons)

- Argon, Ar (Cryogenic Gases, PurityPlus 5.0, 99.999% purity, ≤ 2 ppm oxygen, ≤ 2 ppm moisture, ≤ 2 ppm total hydrocarbons)

- Carbon dioxide, CO_2 (Cryogenic Gases, PurityPlus Laser 4.5, 99.995% purity, ≤ 5ppm moisture, ≤ 5 ppm oxygen, ≤ 5 ppm total hydrocarbons)

Table A.1: Summary of experimental conditions and results for baseline autoignition experiments in which the spark discharge was not used. The mixture composition is provided on a mole basis. The equivalence ratio is based on *iso*-octane to O_2 molar ratios.

		Test Gas Composition[a]									
ϕ	inert $I:O_2$	$\chi_{i-C_8H_{18}}$ [%]	χ_{O_2} [%]	χ_{N_2} [%]	χ_{Ar} [%]	T_{EOC} [K]	P_{EOC} [atm]	T_{eff} [K]	P_{eff} [atm]	τ_{ign} [ms]	T_{ad}[b] [K]
0.30	3.76	0.50	20.90	78.45	0.15	968	8.1	949	7.5	35.0	1875
0.30	4.98	0.40	16.66	80.72	2.23	993	8.2	986	7.9	26.6	1738
0.50	4.99	0.66	16.58	78.00	4.76	958	7.8	945	7.4	34.9	2138
0.50	4.99	0.66	16.59	78.89	3.86	963	7.9	945	7.3	35.8	2138
0.50	7.47	0.47	11.75	86.65	0.00	980	8.5	961	7.7	38.1	1830
0.69	4.99	0.92	16.54	76.87	5.67	945	8.2	926	7.5	39.0	2481
0.70	4.99	0.92	16.54	71.12	11.42	974	8.4	962	8.0	19.8	2536
0.73	7.40	0.69	11.82	83.09	4.39	984	8.9	965	8.2	27.7	2213
0.74	7.43	0.69	11.79	83.13	4.39	999	9.5	981	8.8	21.2	2225
0.74	7.43	0.69	11.78	78.34	9.18	1010	9.1	1001	8.8	14.5	2261

[a] Balance CO_2.
[b] Adiabatic flame temperatures were calculated assuming a constant volume using the initial reactant composition and the end of compression temperature and pressure for each experiment.
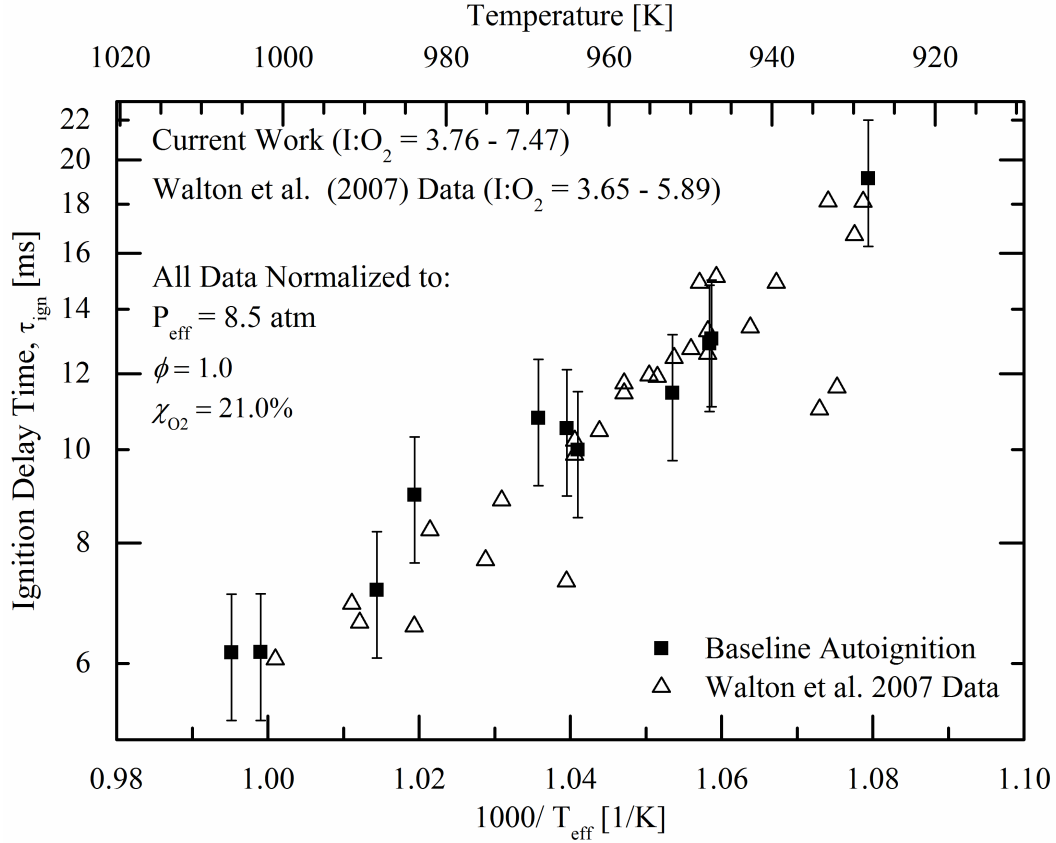
Figure A.1: Comparison of autoignition delay times determined in the current work (Baseline Autoignition) with data from the previous iso-octane autoignition study by Walton et al. [6]. The spark ignition system was not used with the baseline autoignition experiments. The error bars represent the uncertainty for the experiments in this study and was determined to be $\pm$ 15%. Data from the previous iso-octane RCF study by Walton et al. [6] were in the range of $P_{eff} = 9.0 - 12.0$ atm and inert to O_2 ratio 3.65 – 5.89. All data have been scaled to $P_{eff} = 8.5$, $\phi = 1.0$, and $\chi_{O_2} = 21.0\%$ using the functional dependence derived by Walton et al. [6] in which $P_{eff}^{-1.25}$, $\tau_{ign} \propto \phi^{-0.79}$, and $\chi_{O_2}^{-1.14}$.
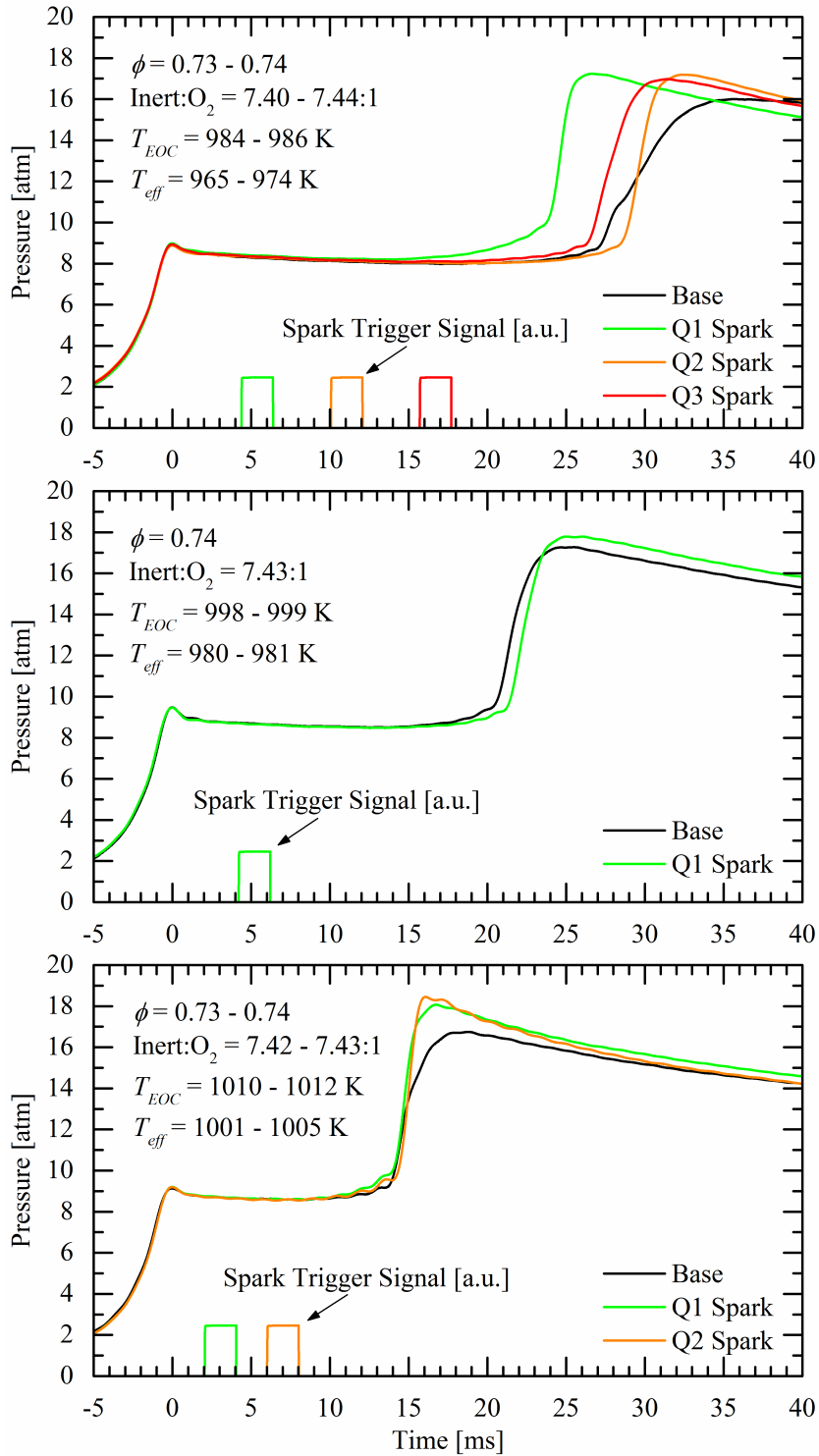
Figure A.2: Comparison of the pressure time histories for different spark timings for different end-of-compression state and mixture conditions.

APPENDIX B

Supplemental Material for the Computational Development of a Dual Pre-Chamber Internal Combustion Engine Concept

Table B.1: Summary of initial conditions for the regions in the dual pre-chamber computational model.

ID	Name	Temperature [K]	Pressure [kPa]
0	Cylinder	894	107.5
1	Intake System	320	61.8
2	Exhaust System	894	107.5
3	Pre-Chamber A	600	107.5
4	Pre-Chamber B	600	107.5
5	Orifices A	600	107.5
6	Orifices B	600	107.5

Table B.2: Summary of the boundaries in the dual pre-chamber computational model.

ID	Name	Region Name	Boundary Type	Temperature [K]	Pressure [Pa]
1	Piston	Cylinder	Translating Wall	530	-
2	Liner	Cylinder	Stationary Wall	420	-
3	Head	Cylinder	Stationary Wall	435	-
4	Pre-Chamber A	Pre-Chamber A	Stationary Wall	400	-
5	Orifices A	Orifices A	Stationary Wall	500	
6	Pre-Chamber B	Pre-Chamber B	Stationary Wall	400	
7	Orifices B	Orifices B	Stationary Wall	500	
8	Intake Port	Intake System	Stationary Wall	400	-
9	Intake Valve Top	Intake System	Translating Wall	500	-
10	Intake Valve Angle	Intake System	Translating Wall	625	-
11	Intake Valve Bottom	Cylinder	Translating Wall	625	-
12	Exhaust Port	Exhaust System	Stationary Wall	450	-
13	Exhaust Valve Top	Exhaust System	Translating Wall	550	-
14	Exhaust Valve Angle	Exhaust System	Translating Wall	675	-
15	Exhaust Valve Bottom	Cylinder	Translating Wall	675	-
16	Inflow	Intake System	Inflow	Specified Profile	Specified Profile
17	Outflow	Exhaust System	Outflow	Specified Profile	Specified Profile

Table B.3: Summary of region event schedule for the dual pre-chamber computational model.

Event Type	Event Start [CAD]	Region 1	Region 2	Event
Cyclic	358	Cylinder	Intake System	Open
Cyclic	623	Cylinder	Intake System	Close
Cyclic	165	Cylinder	Exhaust System	Open
Cyclic	404	Cylinder	Exhaust System	Close
Permanent	-	Cylinder	Pre-Chamber A	Open
Permanent	-	Cylinder	Pre-Chamber B	Open
Permanent	-	Orifices A	Pre-Chamber A	Open
Permanent	-	Orifices B	Pre-Chamber B	Open

BIBLIOGRAPHY

BIBLIOGRAPHY

[1] D. Assanis, S. W. Wagnon, and M. S. Wooldridge, "An experimental study of flame and autoignition interactions of iso-octane and air mixtures," *Combustion and Flame*, vol. 162, pp. 1214–1224, apr 2015.

[2] The Royal Society, "The Basics of Climate Science," 1896.

[3] U.S. Energy Information Administration, "Annual Energy Outlook 2015 with projections to 2040," tech. rep., U.S. Energy Information Administration, Washington D.C., USA, 2015.

[4] United States Department of Transportation, "Average Fuel Efficiency of U.S. Light Duty Vehicles."

[5] G. A. Lavoie, E. Ortiz-Soto, A. Babajimopoulos, J. B. Martz, and D. N. Assanis, "Thermodynamic sweet spot for high-efficiency, dilute, boosted gasoline engines," *International Journal of Engine Research*, vol. 14, pp. 260–278, jun 2013.

[6] S. Walton, X. He, B. Zigler, M. Wooldridge, and A. Atreya, "An experimental investigation of iso-octane ignition phenomena," *Combustion and Flame*, vol. 150, pp. 246–262, aug 2007.

[7] P. S. Shingne, M. S. Gerow, V. Triantopoulos, S. V. Bohac, and J. B. Martz, "A Comparison of Valving Strategies Appropriate for Multimode Combustion Within a Downsized Boosted Automotive EnginePart II: Mid Load Operation Within the SACI Combustion Regime," *Journal of Engineering for Gas Turbines and Power*, vol. 136, no. 10, p. 101508, 2014.

[8] M. S. Gerow, P. S. Shingne, V. Triantopoulos, S. V. Bohac, and J. B. Martz, "A Comparison of Valving Strategies Appropriate for Multimode Combustion Within a Downsized Boosted Automotive EnginePart II: Mid Load Operation Within the SACI Combustion Regime," *Journal of Engineering for Gas Turbines and Power*, vol. 136, p. 101509, may 2014.

[9] J. E. Dec, "Advanced compression-ignition engines - Understanding the incylinder processes," *Proceedings of the Combustion Institute*, vol. 32 II, no. 2, pp. 2727–2742, 2009.

[10] A. M. K. P. Taylor, "Science review of internal combustion engines," *Energy Policy*, vol. 36, pp. 4657–4667, dec 2008.

[11] A. C. Alkidas, "Combustion advancements in gasoline engines," *Energy Conversion and Management*, vol. 48, pp. 2751–2761, nov 2007.

[12] M. Yao, Z. Zheng, and H. Liu, "Progress and recent trends in homogeneous charge compression ignition (HCCI) engines," *Progress in Energy and Combustion Science*, vol. 35, pp. 398–437, oct 2009.

[13] H. R. Ricardo, "Internal-Combustion Engine," 1918.

[14] A. K. Oppenheim, K. Teichman, K. Hom, and H. E. Stewart, "Jet Ignition of an Ultra-Lean Mixture," pp. 2416–2428, feb 1978.

[15] D. Gussak, L., Turkish, M., and Siegla, "High Chemical Activity of Incomplete Combustion Products and a Method of Prechamber Torch Ignition for Avalanche Activation of Combustion in Internal Combustion Engines," *SAE Technical Paper 750890*, p. 25, 1975.

[16] M. C. Turkish, "3 - Valve Stratified Charge Engines: Evolvement, Analysis and Progression," in *SAE International*, pp. 3483–3503, feb 1974.

[17] E. A. Purins, "Pre-Chamber Stratified Charge Engine Combustion Studies," feb 1974.

[18] K. S. Varde, "An optical investigation of the combustion of a stratified mixture in a dual chamber confinement," *The Canadian Journal of Chemical Engineering*, vol. 52, pp. 426–431, jun 1974.

[19] F. F. Pischinger and K. J. Klöcker, "Single-Cylinder Study of Stratified Charge Process with Prechamber-Injection," in *SAE Technical Paper 741162*, feb 1974.

[20] G. C. Davis, R. B. Krieger, and R. J. Tabaczynski, "Analysis of the Flow and Combustion Processes of a Three-Valve Stratified Charge Engine with a Small Prechamber," pp. 3534–3550, feb 1974.

[21] W. R. Brandstetter, G. Decker, H. J. Schafer, and D. Steinke, "The Volkswagen PCI Stratified Charge Concept-Results from the 1.6 Liter Air Cooled Engine," feb 1974.

[22] K. S. Varde and M. J. Lubin, "The Roll of Connecting Nozzle and the Flame Initiation Point in the Performance of a Dual Chamber Stratified Charge Engine," feb 1974.

[23] L. Manofsky, J. Vavra, D. Assanis, and A. Babajimopoulos, "Bridging the Gap between HCCI and SI: Spark-Assisted Compression Ignition," *SAE Technical Paper*, no. x, pp. 01–1179, 2011.

[24] B. T. Zigler, P. E. Keros, K. B. Helleberg, M. Fatouraie, D. Assanis, and M. S. Wooldridge, "An experimental investigation of the sensitivity of the ignition and combustion properties of a single-cylinder research engine to spark-assisted HCCI," *International Journal of Engine Research*, vol. 12, pp. 353–375, aug 2011.

[25] J. P. Szybist and B. H. West, "The Impact of Low Octane Hydrocarbon Blending Streams on the Knock Limit of E85," *SAE Int. J. Fuels Lubr.*, vol. 6, pp. 44–54, apr 2013.

[26] F. A. Matekunas, "Schlieren study of combustion in a rapid compression machine simulating the spark ignition engine," *Proc Combust Inst*, vol. 17, pp. 1283–1294, 1979.

[27] M. Kono, S. Shiga, S. Kumagai, and K. Iinuma, "Thermodynamic and experimental determinations of knock intensity by using a spark-ignited rapid compression machine," *Combustion and Flame*, vol. 54, no. 1-3, pp. 33–47, 1983.

[28] S. Shiga, S. Ozone, H. T. C. Machacon, T. Karasawa, H. Nakamura, T. Ueda, N. Jingu, Z. Huang, M. Tsue, and M. Kono, "A study of the combustion and emission characteristics of compressed-natural-gas direct-injection stratified combustion using a rapid-compression-machine," *Combustion and Flame*, vol. 129, no. 1-2, pp. 1–10, 2002.

[29] S. Shiga, M. Araki, T. Obokata, Z. Huang, H. I. Takamasa Ueda, and M. T. Michikata Kono, "Basic Aspect of Combustion of CNG Incylinder Direct-Injection with Spark-Ignition," *SAE Technical Paper*, 2005.

[30] A. C. S. Villela, S. L. Braga, J. C. C. Egúsquiza, and G. B. Machado, "Rapid Compression Machine Tests for Brazilian Otto Cycle Fuels," *SAE Technical Paper*, 2011.

[31] X. He, M. T. Donovan, B. T. Zigler, T. R. Palmer, S. M. Walton, M. S. Wooldridge, and A. Atreya, "An experimental and modeling study of iso-octane ignition delay times under homogeneous charge compression ignition conditions," *Combustion and Flame*, vol. 142, pp. 266–275, aug 2005.

[32] X. He, B. T. Zigler, S. M. Walton, M. S. Wooldridge, and A. Atreya, "A rapid compression facility study of OH time histories during iso-octane ignition," *Combustion and Flame*, vol. 145, pp. 552–570, may 2006.

[33] X. He, S. M. Walton, B. T. Zigler, M. S. Wooldridge, and A. Atreya, "Experimental investigation of the intermediates of isooctane during ignition," *International Journal of Chemical Kinetics*, vol. 39, no. 9, pp. 498–517, 2007.

[34] M. T. Donovan, X. He, B. T. Zigler, T. R. Palmer, M. S. Wooldridge, and A. Atreya, "Demonstration of a free-piston rapid compression facility for the study of high temperature combustion phenomena," *Combustion and Flame*, vol. 137, pp. 351–365, may 2004.

[35] B. Mcbride, S. Gordon, and M. Reno, "Coefficients for Calculating Thermodynamic and Transport Properties of Individual Species," *Nasa Technical Memorandum*, vol. 4513, no. NASA-TM-4513, p. 98, 1993.

[36] D. M. a. Karwat, S. W. Wagnon, P. D. Teini, and M. S. Wooldridge, "On the chemical kinetics of n-butanol: ignition and speciation studies," *J. Phys. Chem. A*, vol. 115, pp. 4909–21, may 2011.

[37] S. W. Wagnon and M. S. Wooldridge, "Effects of buffer gas composition on autoignition," *Combustion and Flame*, vol. 161, pp. 898–907, apr 2014.

[38] T. Tahtouh, F. Halter, and C. Mounaïm-Rousselle, "Measurement of laminar burning speeds and Markstein lengths using a novel methodology," *Combustion and Flame*, vol. 156, pp. 1735–1743, sep 2009.

[39] A. P. Kelley, J. K. Bechtold, and C. K. Law, "Premixed flame propagation in a confining vessel with weak pressure rise," *Journal of Fluid Mechanics*, vol. 691, pp. 26–51, dec 2012.

[40] Z. Chen, M. P. Burke, and Y. Ju, "Effects of Lewis number and ignition energy on the determination of laminar flame speed using propagating spherical flames," *Proceedings of the Combustion Institute*, vol. 32 I, pp. 1253–1260, jan 2009.

[41] M. Mehl, W. J. Pitz, C. K. Westbrook, and H. J. Curran, "Kinetic modeling of gasoline surrogate components and mixtures under engine conditions," *Proceedings of the Combustion Institute*, vol. 33, no. 1, pp. 193–200, 2011.

[42] D. Assanis, N. Engineer, P. Neuman, and M. Wooldridge, "Computational Development of a Dual Pre-Chamber Engine Concept for Lean Burn Combustion," in *SAE International 2016-01-2242*, oct 2016.

[43] S. Philipp, R. Hoyer, F. Adam, S. Eckhoff, R. Wunsch, C. Schoen, and G. Vent, "Exhaust Gas Aftertreatment for Lean Gasoline Direct Injection Engines - Potential for Future Applications," apr 2013.

[44] Y. Takashima, H. Tanaka, T. Sako, and M. Furutani, "Evaluation of Engine Performance and Combustion in Natural Gas Engine with Pre-Chamber Plug under Lean Burn Conditions," *SAE International Journal of Engines*, vol. 8, no. 1, pp. 221–229, 2014.

[45] A. Shah, P. Tunestal, and B. Johansson, "Effect of Pre-Chamber Volume and Nozzle Diameter on Pre-Chamber Ignition in Heavy Duty Natural Gas Engines," in *SAE International*, no. group 1, apr 2015.

[46] S. Szwaja, A. Jamrozik, and W. Tutak, "A two-stage combustion system for burning lean gasoline mixtures in a stationary spark ignited engine," *Applied Energy*, vol. 105, pp. 271–281, may 2013.

[47] N. Watson and M. Kamel, "Thermodynamic Efficiency Evaluation of an Indirect Injection Diesel Engine," pp. 158–171, feb 1979.

[48] E. Toulson, H. J. Schock, and W. P. Attard, "A Review of Pre-Chamber Initiated Jet Ignition Combustion Systems," in *Internal Combustion Engines*, oct 2010.

[49] N. S. Mavinahally, D. N. Assanis, K. R. Govinda Mallan, and K. V. Gopalakrishnan, "Torch Ignition: Ideal for Lean Burn Premixed-Charge Engines," *Journal of Engineering for Gas Turbines and Power*, vol. 116, no. 4, p. 793, 1994.

[50] W. P. Attard and P. Parsons, "A Normally Aspirated Spark Initiated Combustion System Capable of High Load , High Efficiency and Near Zero NOx Emissions," *SAE International Journal of Engines*, vol. 3, no. 2, pp. 269–287, 2010.

[51] R. D. Reitz and R. Diwakar, "Structure of High-Pressure Fuel Sprays," *SAE Technical Paper 870598*, vol. 96, pp. 492–509, 1987.

[52] K. J. Richards, "Icef2012-92043," pp. 1–14, 2015.

[53] P. K. Senecal, K. J. Richards, E. Pomraning, T. Yang, M. Z. Dai, R. M. Mcdavid, M. a. Patterson, S. Hou, and T. Shethaji, "A New Parallel Cut-Cell Cartesian CFD Code for Rapid Grid Generation Applied to In-Cylinder Diesel Engine Simulations," *SAE Technical Paper*, vol. 2007, no. 724, pp. 776–790, 2007.